Design and Optimization of a Formula SAE Vehicle

A Major Qualifying Project Submitted to the Faculty of
Worcester Polytechnic Institute
in partial fulfilment of the requirements for the
Bachelor of Science Degree in Mechanical Engineering by:

_____   _____   _____
James Chakalos, ME   Justin Dyer, ME   Matthew Freed, ME

_____   _____
Justin Harris, ME   James Meagher, ME

Date: April 25th, 2019

Approved By:

_____   _____
Professor David Planchard   Professor John Hall

_____
Professor Mustapha Fofana

Abstract

WPI's 2019 vehicle is the culmination of an aggressive team effort to transition to a one year build cycle. The car is a bottom up refinement of the groundwork laid by the 2018 build team, with a heavy emphasis on improving drivability, power, and ergonomics without additional weight. The frame is completely redesigned to increase length and width in the driver compartment, significantly increasing comfort. The pedal assembly is redesigned to allow quick and simple adjustment for a wider range of driver heights. On the powertrain side, a new engine, piston, and intake design combined with more detailed engine modeling to meet our power goals. These changes, together with additional refinements to steering, shifting, and suspension, come together in a car that allows its driver to focus on what matters...going fast.

Executive Summary

The goal of the 2018-2019 FSAE MQP team is to design, optimize, and build a Formula style race car that will compete in the Michigan 2019 Formula SAE Competition. The 2018 WPI team did extremely well in last year's competition, despite many engineering challenges, and this year's team will be considering the designs and methods used in the 2018 car to develop and optimize each sub-system of the car. A major part of the MQP is to validate the various systems used in the 2018 car. Several industry standard simulation software packages were explored. The data from the simulations, as well as driving data collected from last year's competition, will be used to determine what systems need to be redesigned in the future years. All simulation software's used in the development of the 2019 car will be thoroughly documented to act as time saving guides for the future MQP teams.

The 2019 competition car can be classified into eight subsystems: frame, powertrain, suspension, steering, brakes, ergonomics, shifting, and electronics. According to the rules, a new frame structure must be made to compete each year in the Michigan competition. Last year's frame was reviewed, and several suspension pickup points were relocated to decrease the suspension compliance found in the 2018 car. In addition to the change for the suspension, the overall dimensions of the frame were altered to accommodate taller drivers. This decision was made based on driver feedback, as well as the input from the design judging at the 2018 competition.

The engine subsystem required a complete redesign due to the acquisition of a new engine. The 2019 car engine is a 2018 Yamaha WR450F motorcycle engine, a newer version of the 2015 model used previously. This engine went through a complete redesign during this three-year period and has a new cylinder head configuration that required a new intake and exhaust design. A 1D engine simulation software, Ricardo WAVE, was utilized in developing the new intake and exhaust for the new engine platform. An in-depth explanation of this software and the collection of engine data will be included in the engine section. Along with computer simulation data, physical testing of different intake and exhaust configurations are tested on a chassis dynamometer. The data collected from the physical testing is input into the simulation, ultimately producing more accuracy in the engine simulation model.

The shifting system uses the same linear electric actuator as the 2018 car. Improvements have been made to increase the reliability of the electronic shifters on the steering wheel, which was one of the main issues with the previous years system. An automatic clutch produced by Rekluse was installed to ease the drivability

of the vehicle by decreasing engine stalling during hard braking and assisting in engine starting while in gear. Although this system is an off-the-shelf product, a considerable amount of measurements had to be collected to ensure proper operation with a slipper clutch system taken from another Yamaha motor vehicle.

The drivetrain subsystem was carried over from the previous year. The Drexler limited slip differential was used with great success in the 2018 competition. Due to several changes made to the frame and suspension geometry several components in the drivetrain would need to be redesigned. The addition of electronic sensors to the drivetrain system, such as wheel speed sensors, were implemented to optimize the entire powertrain system with new advances such as traction control (need to look into wiring to see if any ECU inputs are available).

The suspension subsystem was kept similar in design to the 2018 car. Minor geometry changes, such as widening the track width and altering the rocker motion ratios, were implemented to improve the cornering stability. Along with this, camber values and kingpin angles were also adjusted utilizing last years data and recommendations from autocross professionals. A suspension kinematics software was used to fine tune the pickup points, help design new uprights, and collect values relating to the vehicle throughout its ride.

The steering subsystem of the 2018 vehicle was revised for use in the 2019 car. A new steering wheel is currently in development, and a new steering quick detach has been selected. The gearbox and lower shaft has been redesigned to pretension the system, reducing backlash in the gears. New positions for Ackerman adjustment have been selected and implemented on the uprights, while maintaining a 14 ft turn radius.

The braking subsystem is based off the 2018 car apart from a new adjustable pedal assembly. The redesigned system is adjustable to three positions, weighs a pound less than the 2018 assembly, and properly implements adjustable brake bias.

The final subsystem of the car is the ergonomics. As previously stated, frame geometry was altered to make the cockpit larger without substantially increasing the weight of the car. Seat design was also a major component. Our team discussed ergonomics with a professional on the optimal sitting position and seat shape for comfortable, yet competitive, driving.

The main goal of the 2019 FSAE MQP was not to completely design a new car. The success of the 2016 and 2018 competition cars demonstrated the WPI FSAE team had a good vehicle platform to start from. The decision to redesign a complete subsystem of the vehicle needs to be supported by data and proven that a new design would benefit the drivability of the car. Complete redesigns of subsystems without justifiable reasoning seems to be a theme within FSAE teams. In order to make these decisions, a deep understanding of each subsystem on the current car needs to be known. By analyzing the systems of the 2018 car with the use of simulation softwares, as well as physical vehicle testing, each subsystem can be analyzed and potentially optimized to provide a more controllable and efficient car.

Table of Contents

Table of Figures

Table of Tables

Units (SI and US)

Quantity	Name	Symbol(s)
Length	meter	m
	inch	in
	foot	ft
mass	kilogram	kg
	pound-mass	lb,lbm
time	second	s
	minute	min
	hour	hr
temperature	kelvin	K
	celsius	C
	fahrenheit	ft
angle	degree	deg, °
angular velocity	rotations per minute	RPM
	radians per second	rad/s
speed, velocity	miles per hour	mph
acceleration relative to gravity	g-force	G
area	square inch	in²
	square meter	m²
volume	cubic centimeter	cc
	liter	lb,lbm
	cubic inch	in³
	cubic meter	m³
density	kilogram per cubic meter	kg/m³
energy	joule	J
power	watt	W, J/s, kg-m²/s³
volumetric flow rate	cubic meter per second	m³/s
mass flow rate	kilogram per second	kg/s
pressure, stress	pounds per square inch	psi, lb/in²
	pascals	Pa, N/m²
torque	inch-pound	in-lb
	foot-pound	ft-lb
	Newton-meter	Nm
force, weight	Newton	N
	pound-force	lb,lbf

Competition Overview

The Formula SAE® series competitions challenge teams of university undergraduate and graduate students to conceive, design, fabricate, develop, and compete with small, formula-style vehicles. The competitions give teams the chance to demonstrate and prove both their creativity and engineering skills in comparison to teams from other universities around the world.

The competition consists of static and dynamic events. Under the static events, teams are judged on business presentations they prepare for their vehicle and their engineering design. Teams also provide a thorough cost analysis of the vehicle, which consists of not only material cost, but machining and assembly cost as well. All of these sections must adhere to strict FSAE rules.

The dynamic event consists of five parts: Acceleration, Skid-Pad, Autocross, Efficiency, and Endurance. Teams will actively push their vehicle to the extremes in these events, trying to receive the most points.

Each event is independently scored, and summed together to return the final scoring for the teams. The team with the most points at the end of all events is deemed the competition winner.

Introduction

Worcester Polytechnic Institute's 2018 SAE team placed 41st out of 120 competition teams. This has been the teams highest ranking placement within the past few years, and it became the 2019 teams MQP goal to optimize the previous year's design to improve our rankings for the 2019 competition. The previous year's team had a two year build cycle, but due to the decision to utilize components from the 2018 car, the 2019 team's build cycle will only require a one year build cycle. This will allow the 2019 team to compete in the 2019 SAE Michigan competition with an optimized version of the 2018 car.

This report was developed to not only inform those interested about the 2019 car, but also to be a well documented reference for future teams. Each section of the report represents a separate subsystem, with documentation on the design formulation, manufacturing techniques, and data collection processes. All rules mentioned within the text are from the 2019 Formula SAE rules document version 2.1.

Frame

Design of Frame
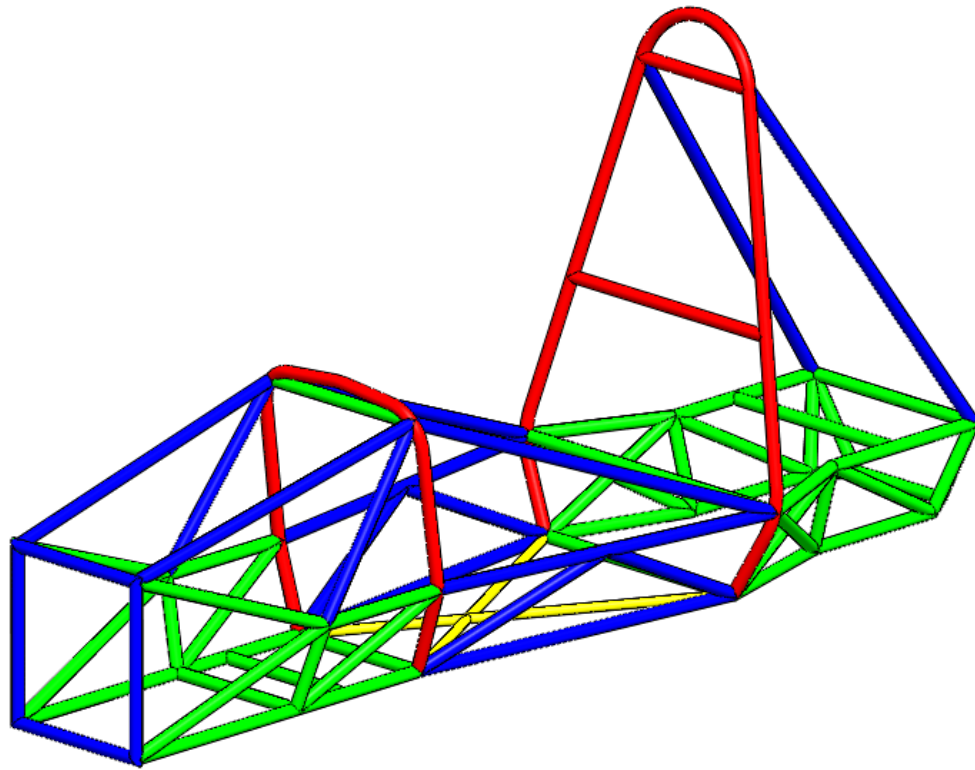
Figure 1: *2018 to 2019 Frame*

Table 1: *Color legend of 2018-2019 frame.*

Tube Color	Cross Section	Outer Diameter	Wall Thickness
Red	Round	1.000"	0.095"
Blue	Round	1.000"	0.065"
Green	Round	1.000"	0.049"
Yellow	Round	0.750"	0.049"

      The frame's overall design was based on the design used by the 2016 to 2017, and 2017 to 2018 teams. The theory behind the design was to create a frame that was light, easy to manufacture, and satisfied the requirements of the 2017 competition rules. The 2017 team did not compete in the 2017 competition, as their project was entirely focused on the design of the frame. The 2017 to 2018 team then grandfathered in the frame

and built components of the car around this pre-existing frame.The team then raced this frame in the 2018 competition.

The 2017 to 2018 team found some issues with the frame in terms of comfort and design flaw. The frame was designed to meet the minimum size requirements provided by the rules. This allowed the frame to pass through competition static judging events; however, limited leg room, elbow room, leg to steering wheel clearance, driver height. Another disadvantage of this frame was the suspension mounting locations. Because the frame was not designed in parallel with suspension and other subsystems of the car, the methods of mounting could not be optimized. Namely, the suspension mounting locations. To keep the suspension mounting locations rigid, they should be attached at the nodes of the welded tube frame. The nodes of the tube frame are the strongest attachment points on the car. It is where 3 or more tubes are joined and gains its strength from the joining of all these members. Because the frame was not designed in parallel with the suspension the control arms, rockers, and springs had to mounted on the mid-span of tubes. In doing this, the tube will experience both torsional and bending stresses to the tubes. This both weakens the frame over time and adds unwanted spring and damping forces to the suspension system. The suspension must be mounted in a rigid fashion or the desired handling will not be achieved.

The overall frame design stood strong in some regards: it had a satisfactory amount of torsional rigidity, it was relatively cheap to manufacture, and it was fairly lightweight for a steel tube frame. The design of this year's frame was based upon the style of the previous design. However, the frame was redesigned so the nodes would be where the suspension mounts to the frame. The frame design started with a 2D sketch of the main defining features of the frame: the main roll hoop, the front roll hoop, then suspension nodes, and the overall length. (Figure 2).
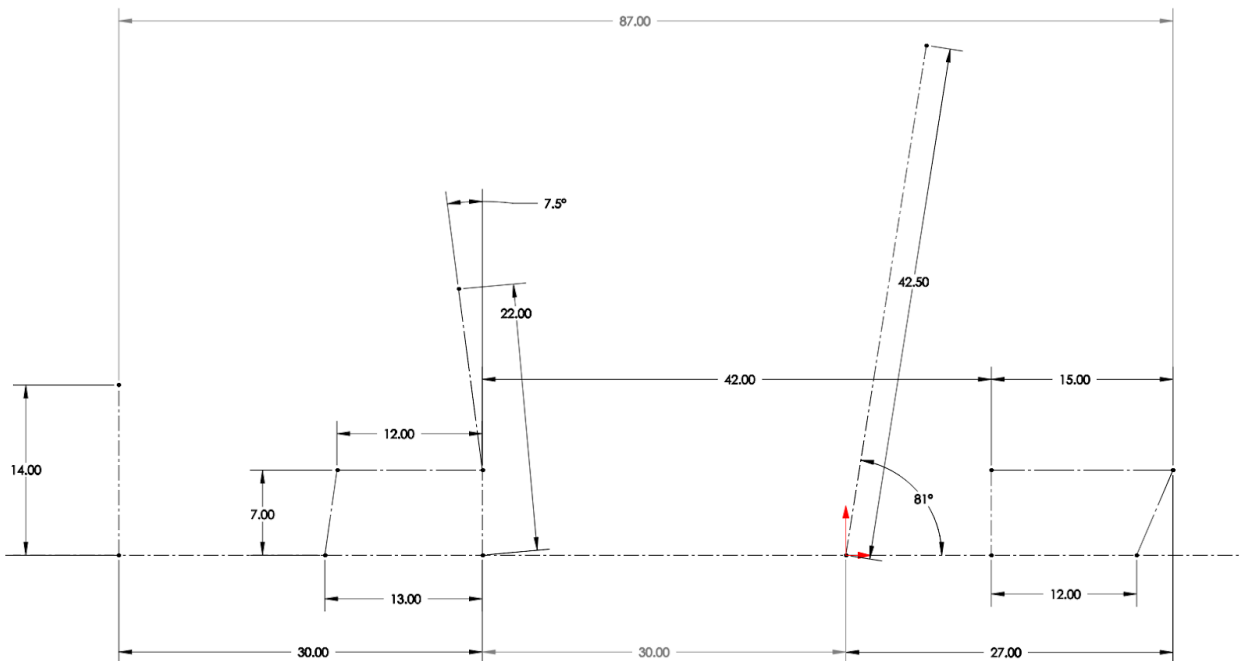
Figure 2: *2D Skeleton of frame with roll hoops, overall length, and suspension mounts*

The main roll hoop is represented by the construction line starting from the origin, extending 42.50" upwards at an 81° angle from horizontal. These dimensions were pulled directly from the old car, there was no reason to change this. Once the main roll hoop was defined, a 2D projection of the control arm mounting locations was brought into the sketch. The rear-most control arm mounting point was 27" behind the origin. From this dimension, the rear and front control arm mounting positions were located. The front roll hoop was then built off of the upper front rearward control arm mount, extending upward at an angle of 7.5° and 22" above the lowest frame tube. This angle and length was chosen for two reasons: the first it puts the top of the front roll hoop an inch above last year's to allow for more room in the cockpit, and the second was for the steering assembly. The steering shaft was designed to run parallel to the front roll hoop, making the steering wheel sit at 7.5° from vertical. This angle is very comfortable for the driver and does not strain the wrists when turning.

From this sketch the widths of the control arm mounting positions were drawn (Figure 3). By constructing the frame in SolidWorks in this manner, it allows for the frame to be constructed around a skeleton defined by the suspension mounting locations and the locations of the roll hoops; two vital components of the frame.
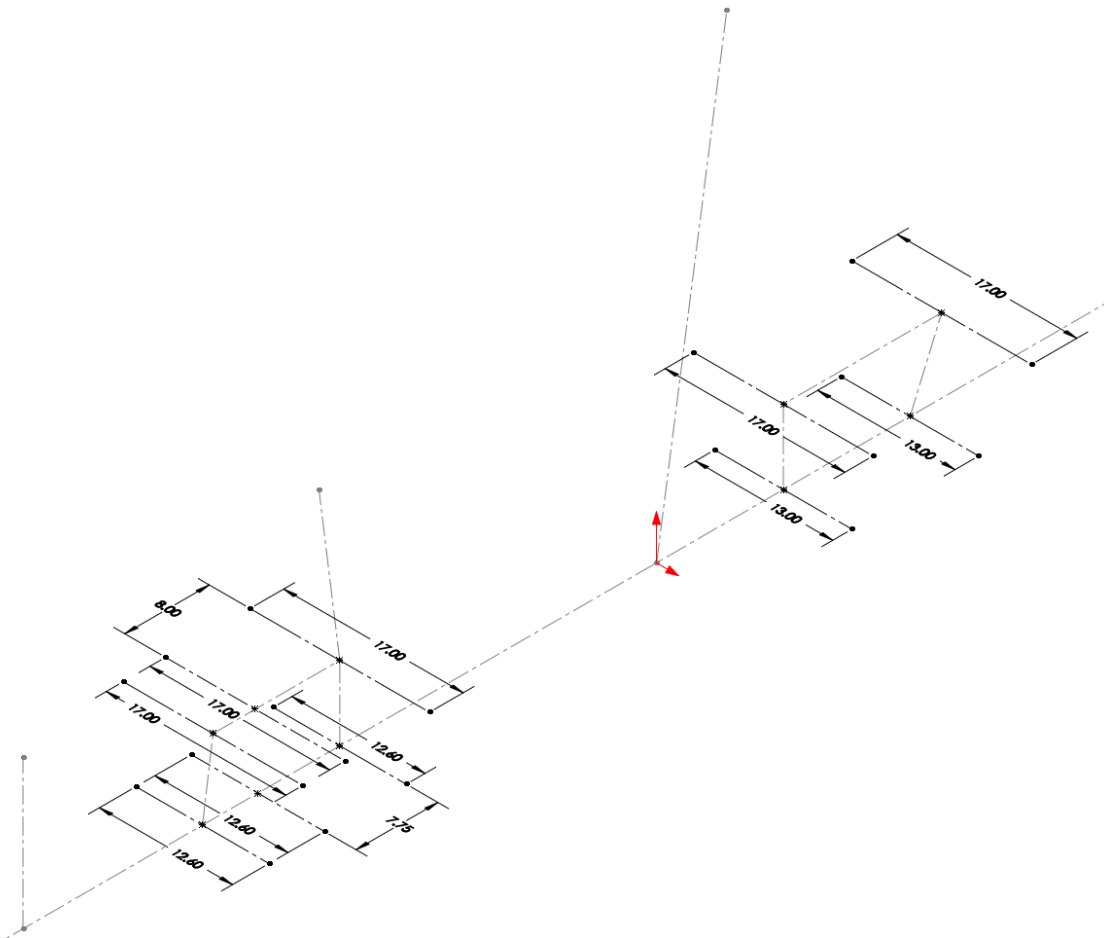
Figure 3: *Sketch of control arm mounting locations.*

By following the design of last year's frame, all frame tubes were constructed in a 3D sketch. The front roll hoop was made 1" wider at the top. This gives the driver a wider cockpit . This gave the driver more elbow room and made the cockpit feel much less claustrophobic. The overall frame length was extended by 1", allowing for an extra 1" of leg room. A comparison of frames can be seen in the following figures 4 to 8. The old frame is pictures in light blue, and the new frame is pictured in red.
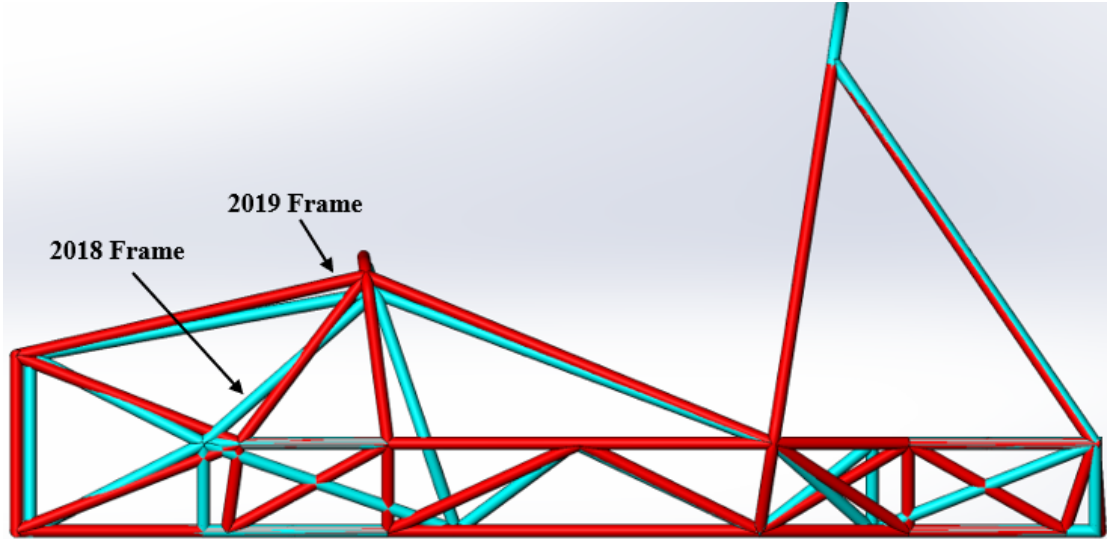
Figure 4: *Right side view comparing 2018 frame to 2019 frame.*

Figure 5 clearly shows the added 1" of legroom and change in roll hoop angle. Another change between years is the direction of the diagonal member triangulating the control arm mount nodes. This was done because there was not enough room for the steering rack if the same orientation were kept.
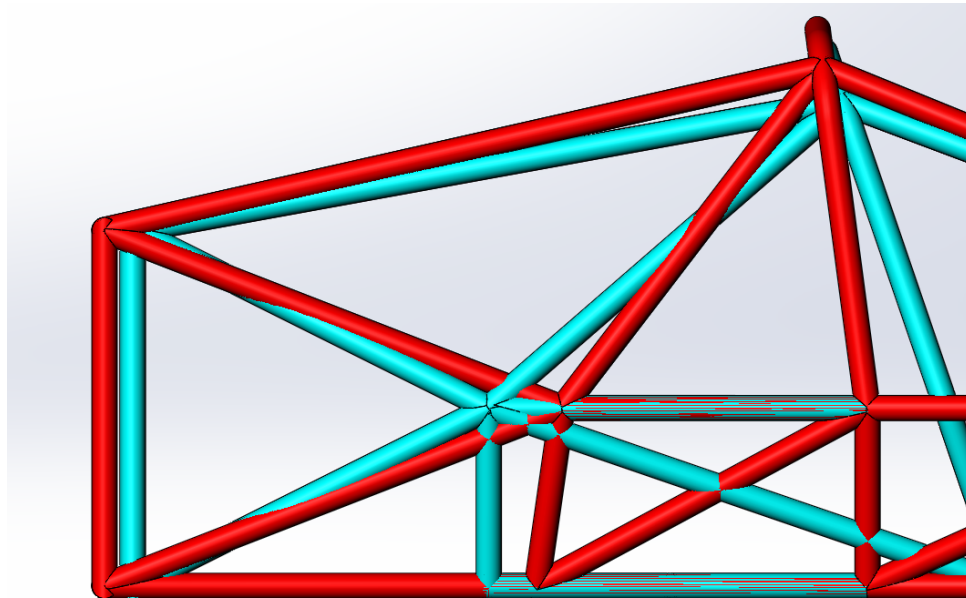
Figure 5: *Right side view of front portion of frames.*

15

In the front view (Figure 6) the change in height and width of the front roll hoop can be seen. The front roll hoop is 1" both taller and wider than the previous year's. This gives the driver more room in the cockpit, an issue with last year's frame.
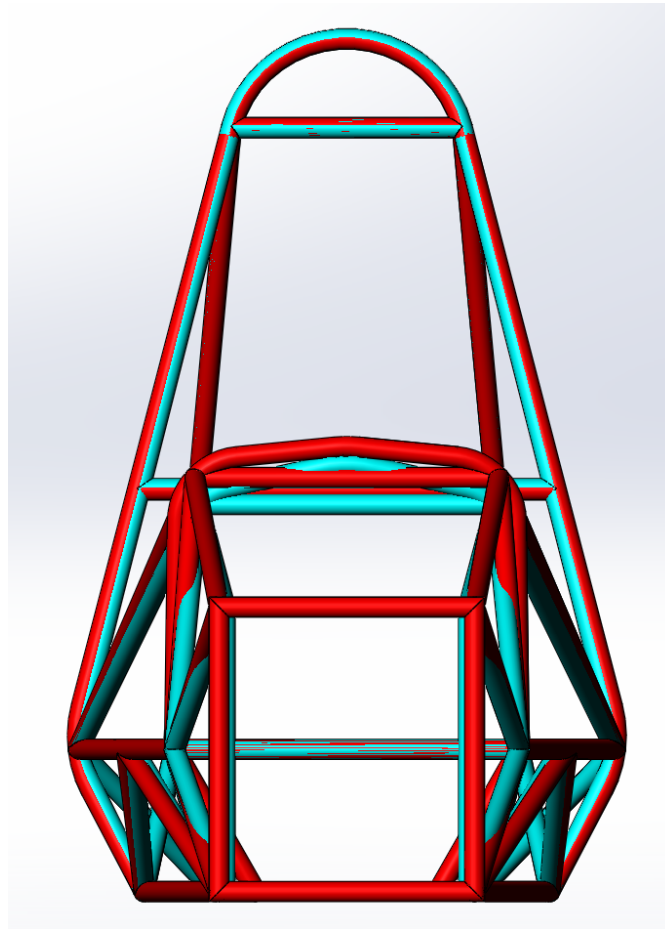
Figure 6: *Front side view of frames.*

In the right side view of the rear portion of the frame (Figure 7), there are a few noteworthy changes. The upper horizontal frame tube remains the same length as the previous year; however, the lower frame tube has been shortened. The upper frame tube remains the same because the control arm could simply be extended to the rear nodes. In the case of the lower, that could not happen. This rear a goal on the suspension was the mount the toe bar to the frame rather than to the control arm. To achieve this, the frame would need to extend rear of the control arm frame mount. This proved to be a challenge because the control arm mount also needed to be a node. This was solved by angling in the vertical member to form a node where the control arm mount needed to be (Figure 8). The frame then angle back to the rear of the car. This gave a spot for the toe bar to mount and allowed enough space to fit the sprocket and differential.
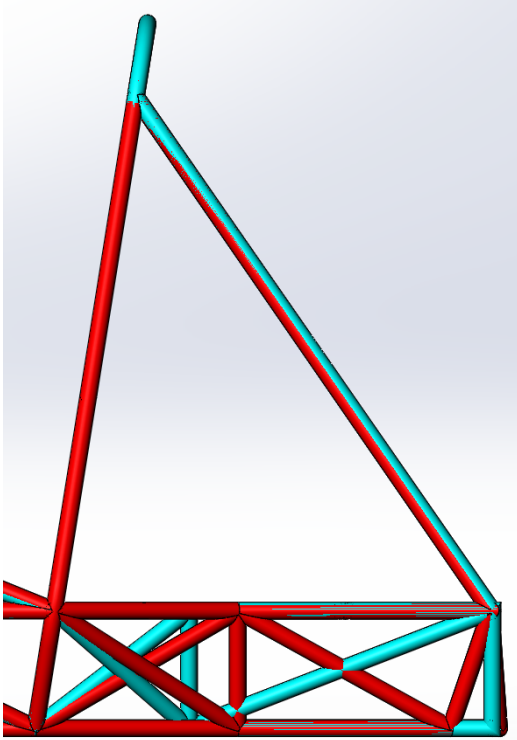
Figure 7: *Rear portion of frames*
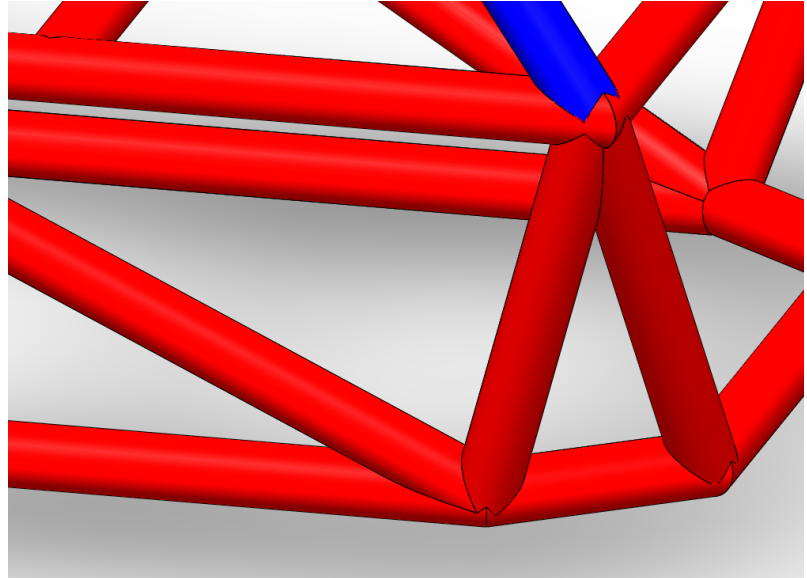
Figure 8: *Rear control arm tab location*

Frame SolidWorks Simulation

Finite element analysis was performed on the frame to check the safety factors in the event of a front impact, side impact, or roll. In the event of a roll, the force could be entirely concentrated on the main roll hoop, front roll hoop, or split between. The scenario in which all the force is on either the main roll hoop or front roll hoop was simulated because that would induce the most stress on either component.

The force value used in the event of a front impact was taken from the attenuator specifications in the rules. It specifies per T.2.25.2 the attenuator must function in the event of a 20g impact with a 300kg car. The resulting force of this impact is 59kN, or split between the four frontal nodes where the attenuator attaches would be 14750 N per node. The SolidWorks simulation was performed with this value as seen in Figure 9. The safety factor in the event of a front impact is a minimum of 1.34. The frame will not break in the event of a front impact of this magnitude and keep the driver safe. The frame was featured at the rear control arm nodes to see how the car would compress with respect to those fixed points.
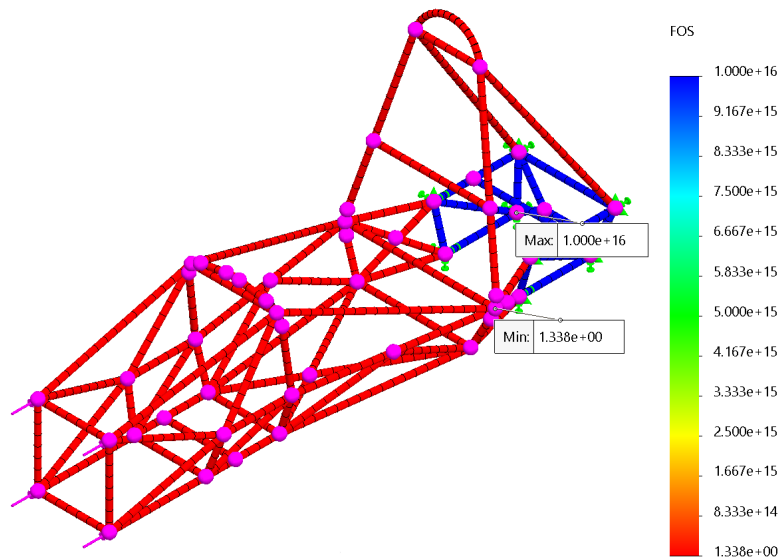
Figure 9: *SolidWorks Simulation results from front impact of 59 kN displaying factor of safety.*

The next simulation (Figure 10) performed was to test the side impact structure. This structure is a vital component in the frame because it protects the driver from any and all side impacts. The frame was fixtured in this test by all control arm nodes. These nodes were picked to simulate if the car was stationary and stuck in that position and a large force were to act on the impact structure, such as another car impacting it. A force of 7000 N acting perpendicular to the side impact structure was used. This value was chosen from previous FSAE frame design evaluation.
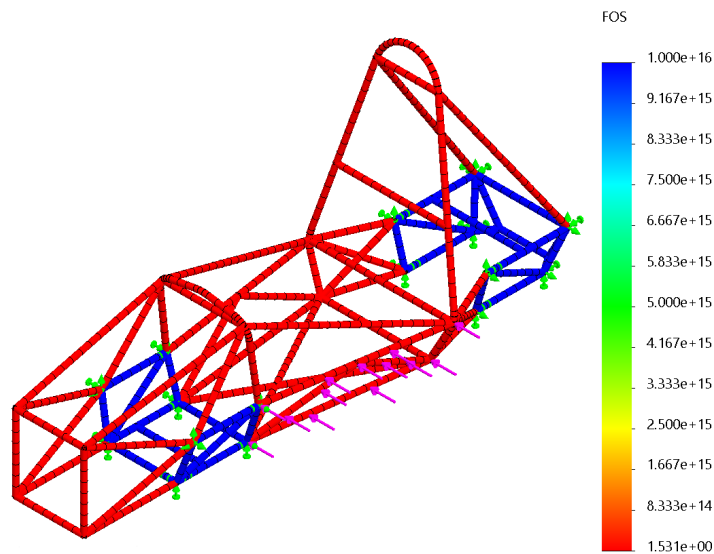
Figure 10: *SolidWorks Simulation results from side impact of 7000 N displaying factor of safety.*

The roll hoop simulations (Figures 11 and 12) were done by fixing the front and rear control arm mount positions. This was done to see how the supporting beams behave under strict compression in case of buckling. A force of 6000 N was derived from the given 300 kg and 20 g from section T.2.25.2. This simulation resulted in a safety factor of 2.71 and 2.21, ensuring the safety of the driver.
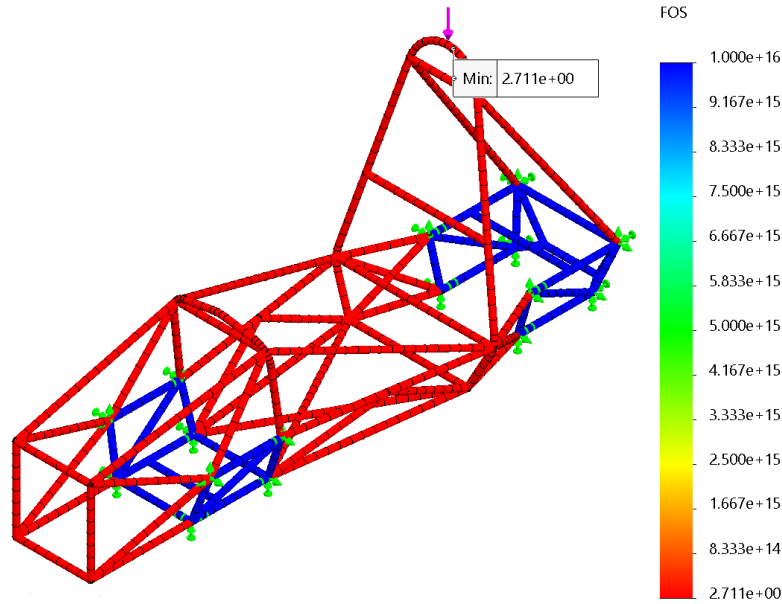
Figure 11: *SolidWorks Simulation results from main roll hoop impact of 6000 N displaying factor of safety.*
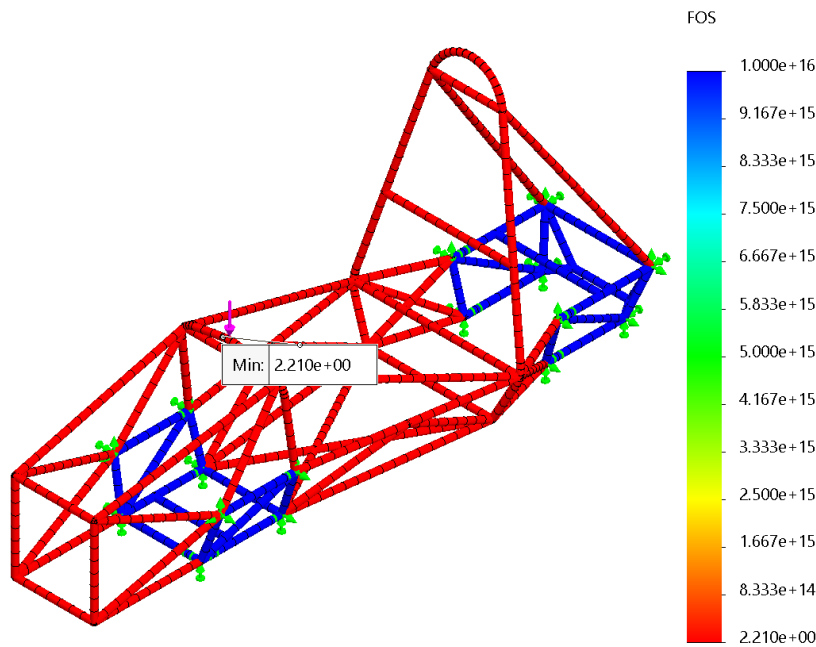
Figure 12: *SolidWorks Simulation results from front roll hoop impact of 6000 N displaying factor of safety.*

The frame was designed to satisfy a requirement of 1° of twist for every 1500Nm applied. The simulation (Figure 13) shows the design holds true to this. Having a frame that is torsionally stiff will help the suspension stay stable and predictable while driving.
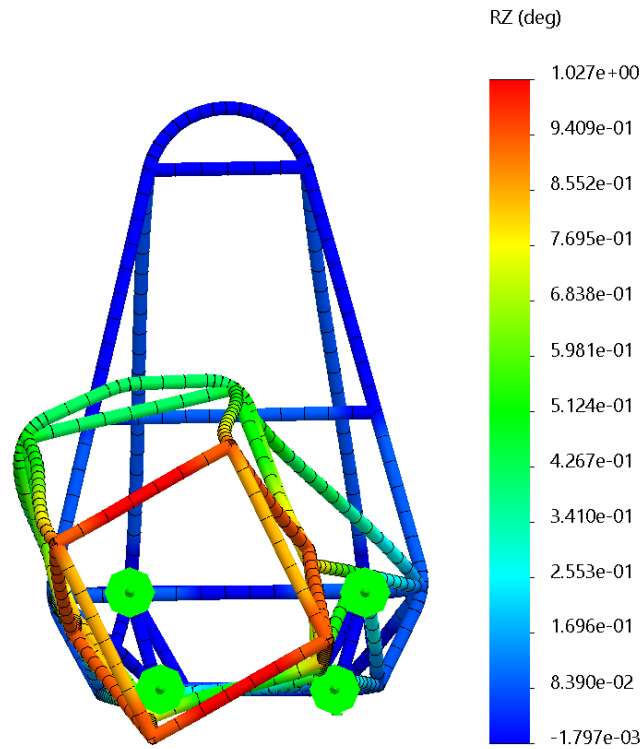
Figure 13: *Torsional rigidity of frame, 1° of twist per 1500Nm.*

Design of Frame Tabs

The frame tabs are to be made of 4130 chromoly steel. They will be spaced 0.9" inches apart to leave enough room for the spherical bearings of the control arms. The tabs will be 0.875" wide and 0.1875" thick. The tabs will be cut to specific lengths that hold the spherical bearings 1.25" away from the centerline of the frame tube per the suspension geometry. Each tab has been cut specifically to match the mating face of the frame node (Figure 14). This will allow the tabs to be mounted in an accurate position. The tabs act in double shear to hold the control arm spherical bearings in with a shoulder bolt.
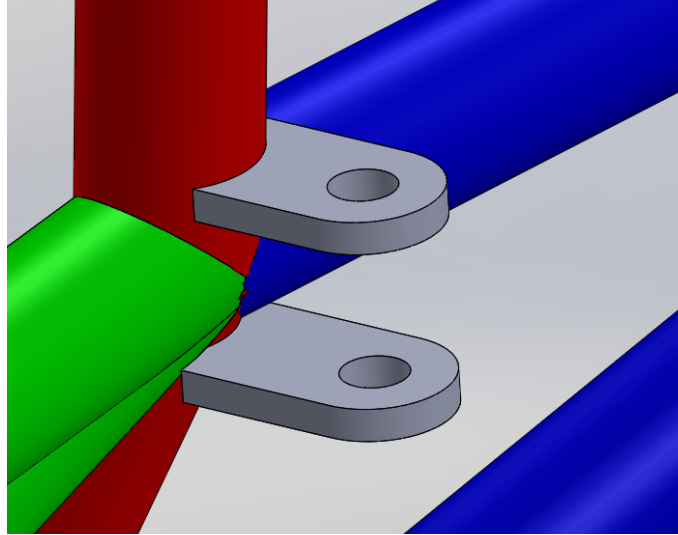
Figure 14: *Control arm tabs at upper left front rear node.*

An analysis of the longest control arm tab with the least amount of mounting surface area was done to check the safety factor in five scenarios: turning in while braking, turning in while accelerating, turning out, high cycle fatigue of accelerating and braking, and high cycle fatigue of turning in and turning out. The tab in question was the tab for the front left and right lower forward control arm mount tabs, denoted in Figure 15.
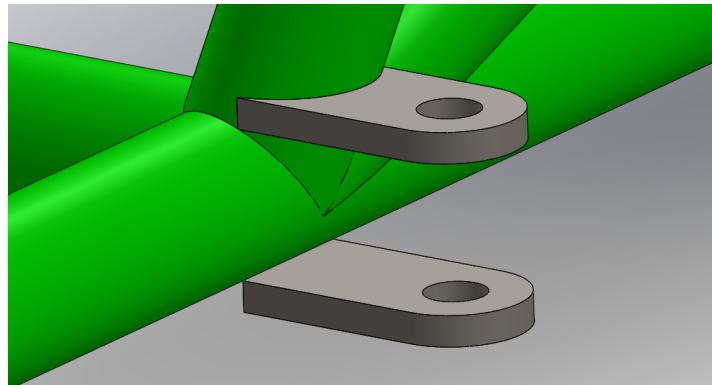
Figure 15: *Control arm tabs to be analyzed. The lower of the two will be the one taken into consideration.*

A section view of the tabs from the rear view with respect to the car can be seen in figures 16 and 17. The left side view can be seen in figures 18 and 19. Each figure has an associated force and reaction forces in the tabs. The figures were made to find how much force each tab experiences in each case of turning in (turning force in the positive x direction), turning out (turning force in the negative x direction), accelerating, and braking. The forces act at the center point between the two tabs. The magnitudes of each for can be found in table 2.
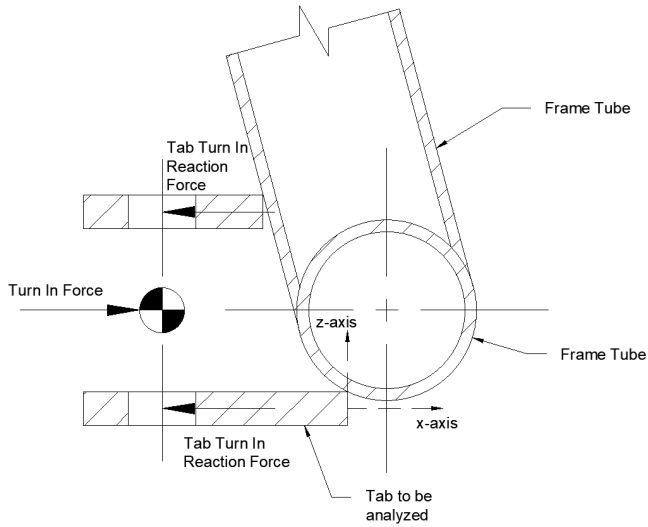
Figure 16: *Diagram of turn in force acting on tabs.*
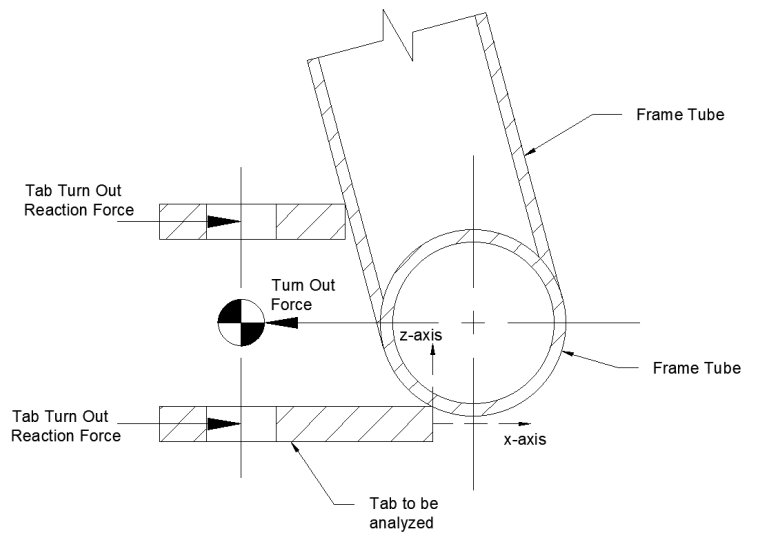
Figure 17: *Diagram of turn out force acting on tabs.*
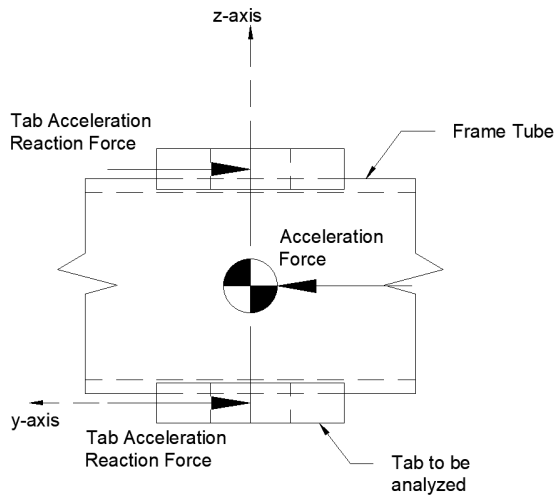
Figure 18: *Diagram of acceleration force on tabs*.
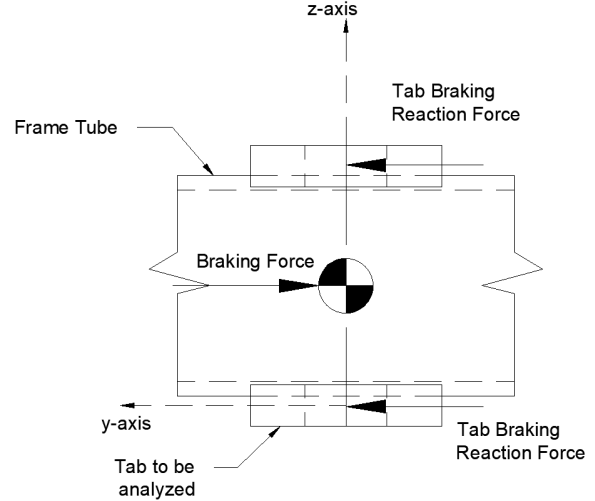
Figure 19: *Diagram of braking force on tabs.*

Table 2: *Magnitude and Direction of Forces Acting on Control Arm Tabs*

Type of Force	Magnitude	Direction
Turn Force	750 lbf	±x
Acceleration Force	500 lbf	+y
Braking Force	750 lbf	-y

The tab was simplified into a cantilever beam 1.16" long. This length was chosen because that is the length from the base to the center of the pin that holds the control arm. This is where the force acts, and because the pin is a tight fit it can be assumed to be one material. Because the control arm is mounted in double shear and the force acts in the middle between each tab, only half the force is felt by each tab. Thus, the following forces in table 3 were used when analyzing the individual tab:

Table 3: *Magnitude and Direction of Forces Acting on One Control Arm Tab*

Type of Force	Magnitude	Direction
Turn Force	375 lbf	±x
Acceleration Force	250 lbf	+y
Braking Force	375 lbf	-y

A freebody diagram of each force is seen in Figure 20. The the turning in and turning out forces cannot act simultaneously, as well as braking or acceleration. Braking and turning in or out or accelerating and turning in or out can act simultaneously. Situations where two forces are acting on the tab will cause the most stress in the part and would be a culprit in causing failure. The tab was analyzed in the following cases in table 4 and all calculations can be seen in appendix B.
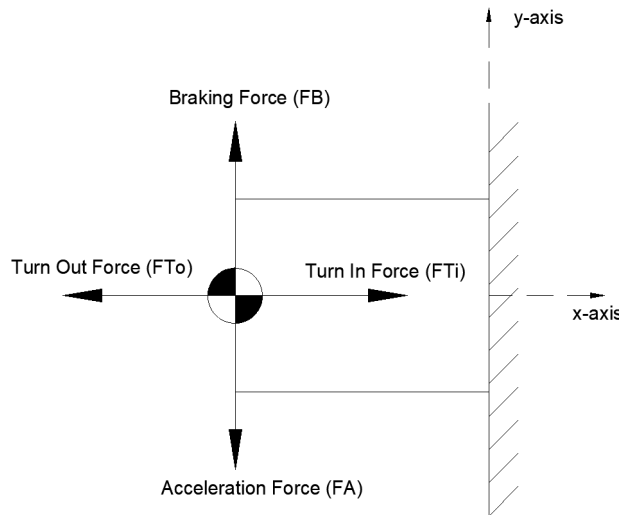
Figure 20: *Free-body diagram of tab represented as cantilever beam*

Table 4: *Results from tab force analysis of weakest tab represented as cantilever beam.*

Case	Analysis Type	Forces Used	Lowest Safety Factor
1	Buckling	Turn In	69.8
2	Static Bending Failure	Acceleration and Turn In	5.6
3	Static Bending Failure	Acceleration and Turn Out	4.3
4	Static Bending Failure	Braking and Turn In	3.6
5	Static Bending Failure	Braking and Turn Out	3.0
6*	Tear Out	Turn Out	11.8
7	Fluctuating Forces: High Cycle Fatigue	Acceleration and Braking	1.4
8	Fluctuating Forces: High Cycle Fatigue	Turn In and Turn Out	8.3

*Note: Case 6 was analyzed as the full tab, not the simplified cantilever beam.

The lowest safety factor of the weakest control arm tab is 1.4. What this means is after the strength of the material degrades from a high life cycle of one million cycles, the part will not fail (assuming the forces do not exceed the calculated values). Steel is a ductile material and according to a graph of Strength to Number of cycles, or S-N graph (Figure 21), the steel's strength will not continue to degrade after one million cycles. The car's suspension mounting pickups will stay firmly attached to the frame and will remain to safe to drive for the life of the car.
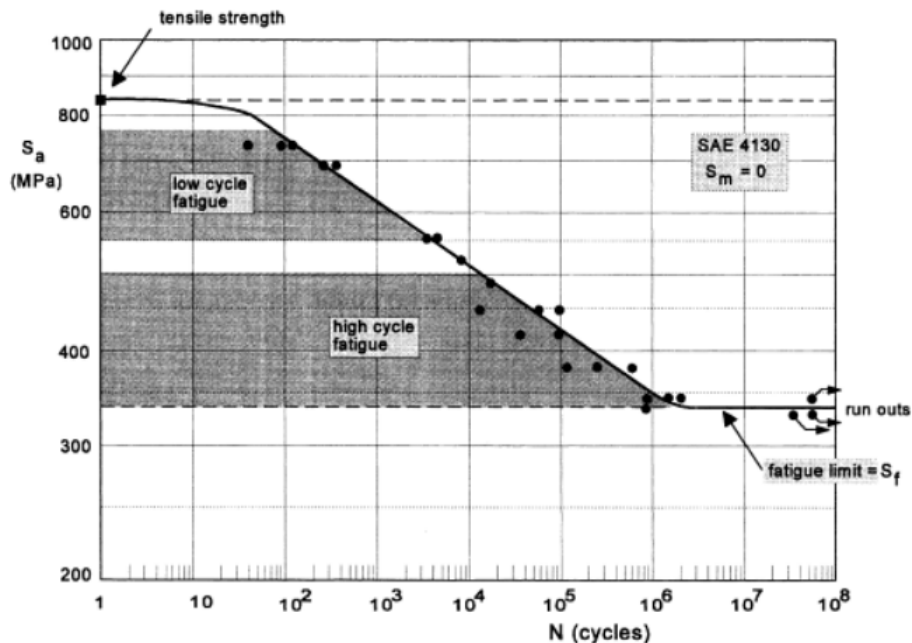
Figure 21: *S-N graph of 4130* [1].

The results from cases 1, 2, 3, 4, 5, and 6 were checked using SolidWorks Simulation. The figures below show the results from the finite element analysis. In all simulations, the tab was fixtured as "fixed geometry" by the face to be welded to the frame. This type of fixturing simulates a weld very accurately in that it holds the fixed face's geometry constant and all forces flow through it. The force was applied to the center of the shoulder bolt hole and acts on the inner diametral face where the shoulder bolt sits.

The buckling analysis (Figure 22) calculated the load factor to be 70.029. This means the force would need to be 70 times larger for the tab to undergo buckling. When the tab was analyzed with the acceleration and turn in forces applied (Figure 23), the minimum factor of safety was 2.995.
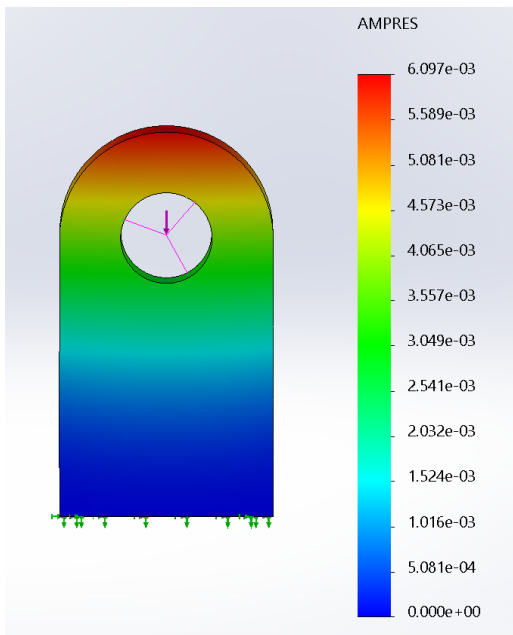
Figure 22: *Turn in force on control arm tab.*
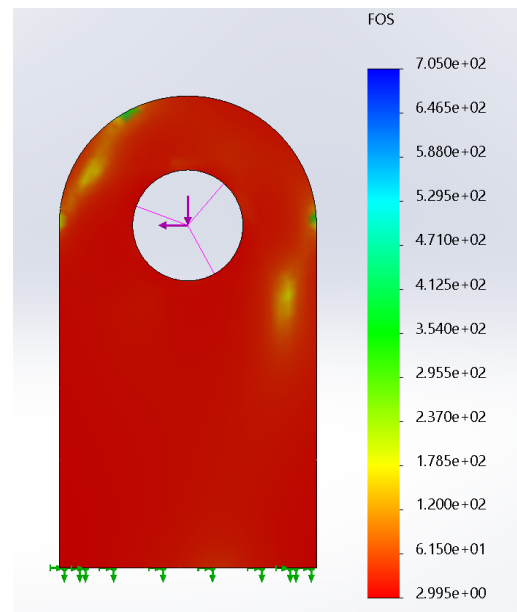
Figure 23: *FoS with acceleration and turn in forces.*
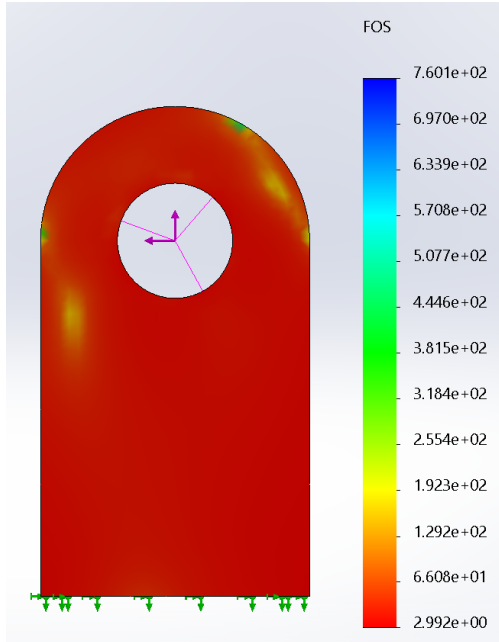
Figure 24: FoS *with acceleration and turn out.*   Figure 25: *FoS with braking and turn in forces applied.*
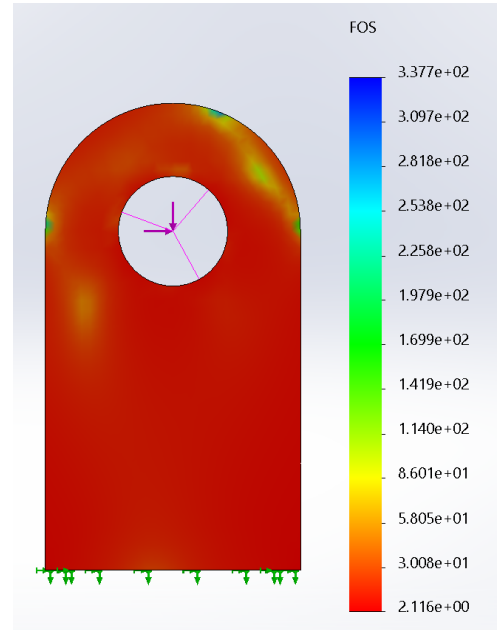
When the tab was analyzed with the acceleration and turn out forces applied (Figure 24), the minimum factor of safety was 2.992. When the tab was analyzed with the braking and turn in forces applied (Figure 25), the minimum factor of safety was 2.116.
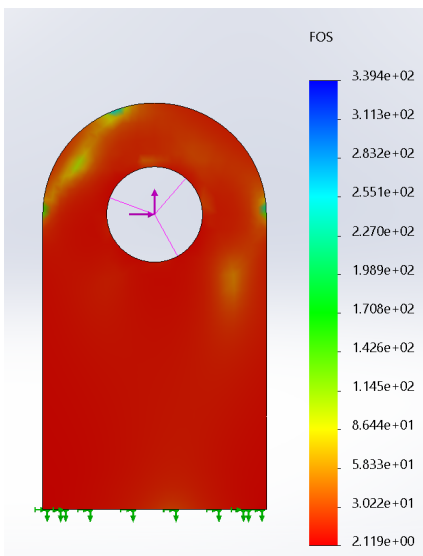
Figure 26: *FoS with braking and turn out forces.*   Figure 27: *FoS with turn out force.*
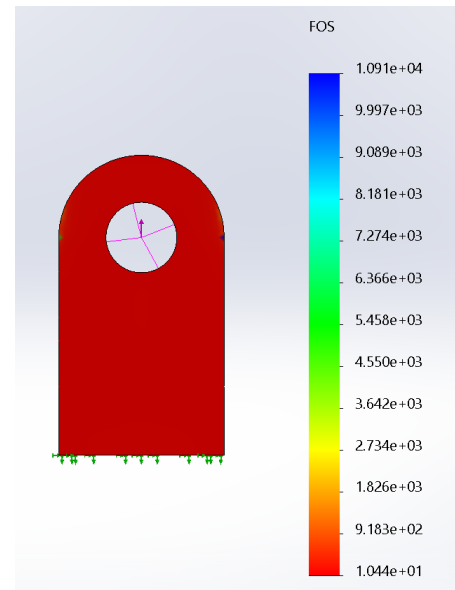
When the tab was analyzed with the turn out force applied (Figure 27), the minimum factor of safety was 10.44. When the tab was analyzed with the braking and turn out forces applied (Figure 26), the minimum factor of safety was 2.119.

In table 5 it can be seen that assuming the tab to act as a cantilever beam provided somewhat accurate results in cases 1 and 6. However, cases 2 through 5 have fairly high percent error. Representing a frame tab as a cantilever beam may not be the best method to predict safety factors and finite elements analysis should be used primarily. Regardless, the tabs will be able to withstand the rigors of competitive track driving. Because the longest and weakest tab will withstand the driving forces,it can be assumed all the tabs will be strong enough.

Table 5: *Comparing cantilever beam analysis results to SolidWorks Simulation results*

Case	Cantilever Beam FOS	SolidWorks Simulation FOS	Percent Error
1	69.8	70.029	0.33%
2	5.6	2.995	46.5%
3	4.3	2.992	30.4%
4	3.6	2.116	41.2%
5	3.0	2.116	29.5%
6	11.8	10.44	11.5%

In Figure 28, a special frame tab has been made to fix the issue in last year's rear tie rod mount. Figure 29 shows the actual mounted rear tab. The tie rod was previously mounted to the control arm, introducing a bending moment and unnecessary stresses in the control arm. To fix this issue, the tie rod mounting position was moved to a node on the frame. Because the mounting locations of the control arm and tie rod are so close together, one large tab was made to attach both. By having a large mount, the welding surface area attaching it the frame is increased, thus increasing the strength of the part. The tie rod will no longer cause unnecessary stresses in the control arm and will transmit all force through the tab and into the frame node.
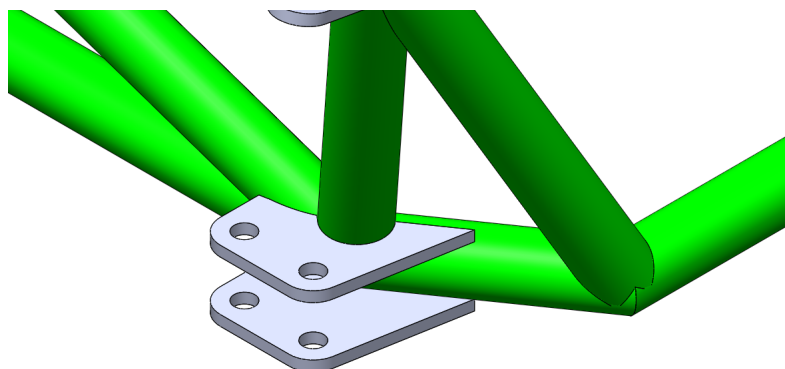
Figure 28: *Rear lower control arm and toe bar dual mount.*

Figure 29: *Rear lower tab actual.*

The welding process to attach the tabs to the frame can be seen in Figure 30 to 34. All welded tabs were waterjet out of 0.1875" thick 4130 plate. By using a waterjet, the tab geometry could be made very precise to help locate themselves on the frame. Each frame tab was specially made to fit to the contour of its welding location. This greatly helped in locating the tabs accurately. The tabs were attached to the frame by TIG welding. To maintain the correct spacing and orientation between the tabs, the two tabs were first bolted together with a 3D printed fixture inbetween. The fixture held the tabs at the proper spacing, aligned the holes, and held the tabs against the frame to be tacked. The 3D printed fixtures were then removed and replaced with a metal spacer. The metal spacer holds the tabs at the correct spacing and alignment when being welded. The 3D printed fixtures were only used during initial tacking, then the metal spacers swapped in for completion. In doing this, the holes for the shoulder bolts stay lined up and the space between the tabs is accurate.
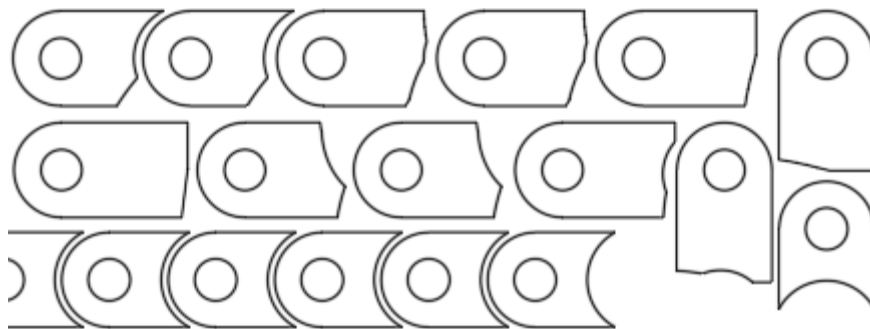
Figure 30: *Frame tab layout for waterjet.*
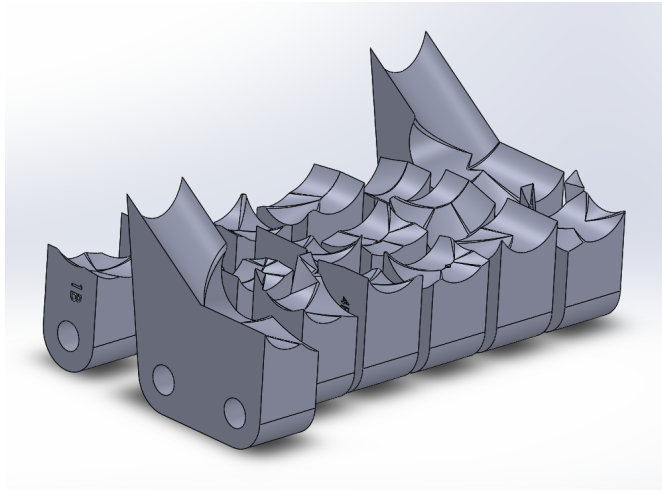
Figure 31: *Tab location fixturing blocks.*

Figure 32: *Welding tabs onto frame.*

Figure 33: *Rear tab with 3D printed fixture.*
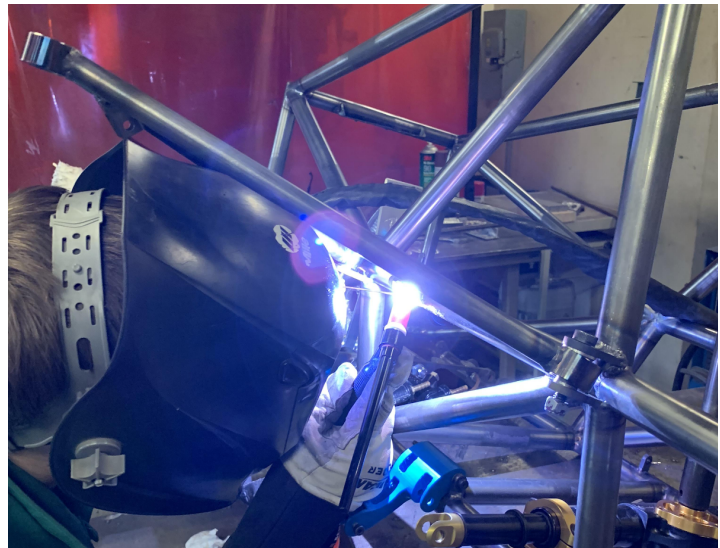
Figure 34: *Shock tabs being welded.*

Tab Placement Verification

The driving motivation behind the redesign of the frame from the 2018 team was to relocate frame nodes to suspension tab locations. The nodes are suspected to be the most rigid locations on the frame and thus perfect for mounting suspension. To test this, SolidWorks FEA was used. A force of 750lbs was placed on the front left upper forward control arm node. The force points in the positive x-direction, simulating a right turn. At the node, there is only 0.12in (3.1mm) of deflection. 2 inches to the right of the node the same force is applied. This is to simulate the suspension force had the tab been mounted offset from the node. There is about twice as much deflection, 0.24in (6.1mm). The node is a much more sturdy location to mount the suspension to.
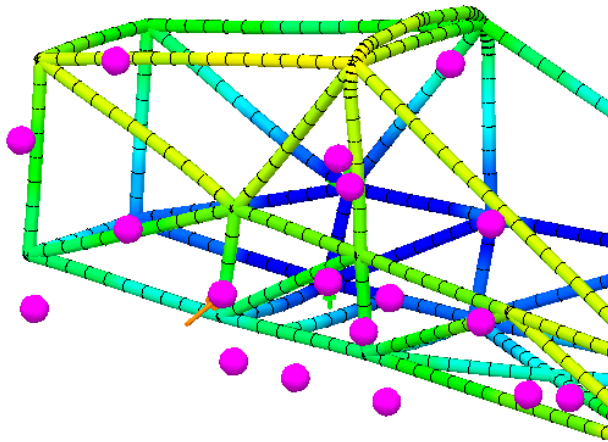
Figure 35: *Force at node.*
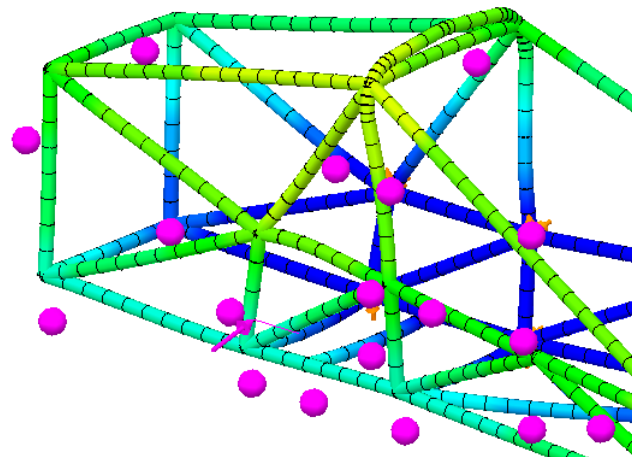
Figure 36: *Force applied 2 inches from node.*

Drivetrain – Power Transmission

The drivetrain system consists of the transmission, the differential, the final drive components, the axles, and the rear wheel hubs. Each system is included in the sections below.

Differential

The 2019 competition car uses the limited slip differential (LSD) made by Drexler Automotive. This differential is specifically designed for Formula SAE and Formula Student competitions and is used by many FSAE teams internationally. The decision to purchase this differential was made by the 2018 MQP team and was chosen for its exceptional performance.

There are several types of limited slip differentials, but the main function between them is the same; it will allow each wheel to rotate at different speeds but will restrict the difference between the two wheels. Most road cars are equipped with on open differential that allows each drive wheel to rotate at different speeds. The reasoning behind this is due to the distance each wheel needs to travel while driving around a corner. The radius of the arc that the inside wheel travels is much smaller than the outside wheel and therefore travels a shorter distance. The outside wheel adapts by rotating at a faster speed than the inside wheel. The application of an open differential benefits road cars by improving tire life and increasing fuel efficiency. The problem with an open differential is when the tires are at the limit of traction. Once one wheel loses traction, it will begin to spin, applying zero torque to the ground, while the other wheel will transfer no torque as well. In auto racing, the tires of the vehicle are balancing on the limit of traction, and an open differential would be detrimental to the performance of the vehicle. Many racing cars use a solid rear axle, sometimes referred to as a spool, to lock the rotation of the rear wheels together. Although this design allows the transfer of torque to a wheel when the other is slipping, it will not allow a difference in wheel speed under non-slip conditions. The compromise between these two systems is a limited slip differential, which can operate like an open differential under non-slip conditions while also being able to control the rotation differences between the wheels when experiencing tire slip.

The Drexler differential is a clutch plate type differential, also known as a Salisbury type. It operates similar to an open differential, but with an additional locking mechanism. This type of differential is load dependent and will only provide locking during acceleration or deceleration. The spider gear axle is not held by the differential housing, rather with two pressure rings located within the housing. These pressure rings are torsionally coupled to the housing but can slide axially and consists of 'ramps' where the spider axle is located. Figure 37 shows the internals to the Drexler limited slip differential.
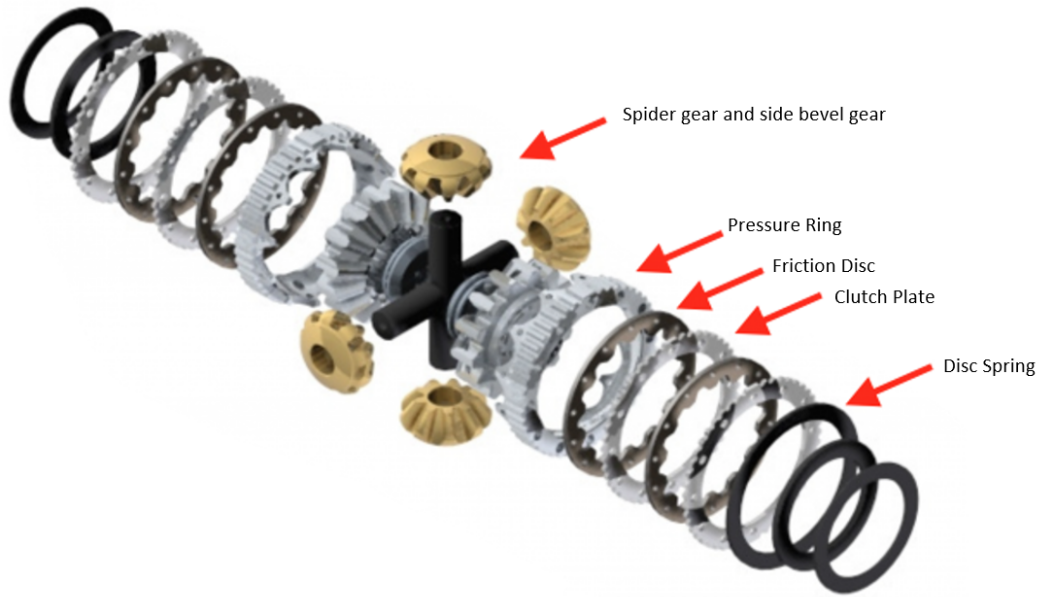
Figure 37: *Exploded view of Salisbury type Differential* [2]

During acceleration, the spider gears axle is wedged into the pressure plate ramps due to the spider gears and axle not being torsionally fixed to the housing. A component of the axle force on the ramps pushes the pressure plates outward and into the clutch packs, locking the differential, seen in Figure 38. The Drexler differential has six ramp adjustment setups that are adjusted by dissembling the differential and rotating the pressure plates. Each pressure plate position has a different ramp angle combination for acceleration and deceleration. Different ramp angles affect how much torque is transferred to each wheel, or how much lock up. The lower the ramp angle, the more lock up (e.g., a 30° ramp angle will lock more than a 45° ramp angle).
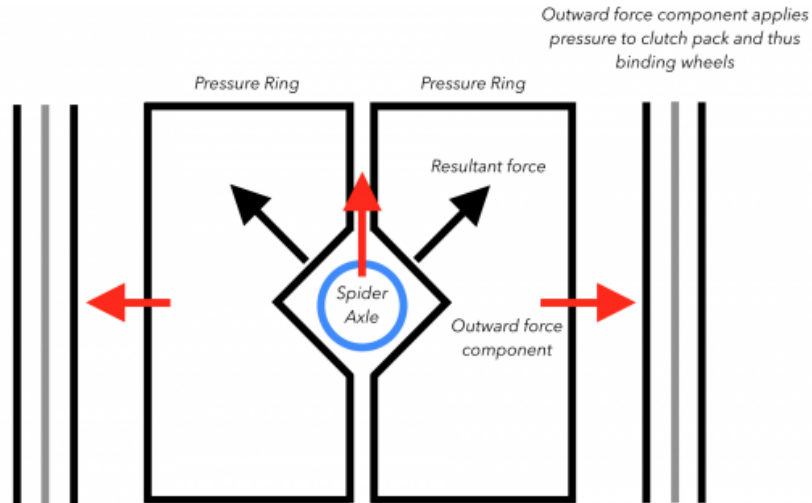
Figure 38: *Pressure Plate Ramp Angles* [2]

Differential Mounts

The differential mounts for the 2019 competition car were based on the previous years design. The main feature of these mounts is the built in chain tensioning system. The differential bearings are mounted in eccentric cups thats can be rotated within the differential mounts. This allows the differential to be moved forwards and backwards by rotating the cups, loosening and tightening the chain respectively. This system was chosen due to its simplicity. By tightening the chain with the eccentric cups the addition of a chain tensioning device can be eliminated. This reduces the complexity and weight of the vehicle by reducing the multiple components needed for a chain tensioning device. The differential assembly can be see in figure 39.
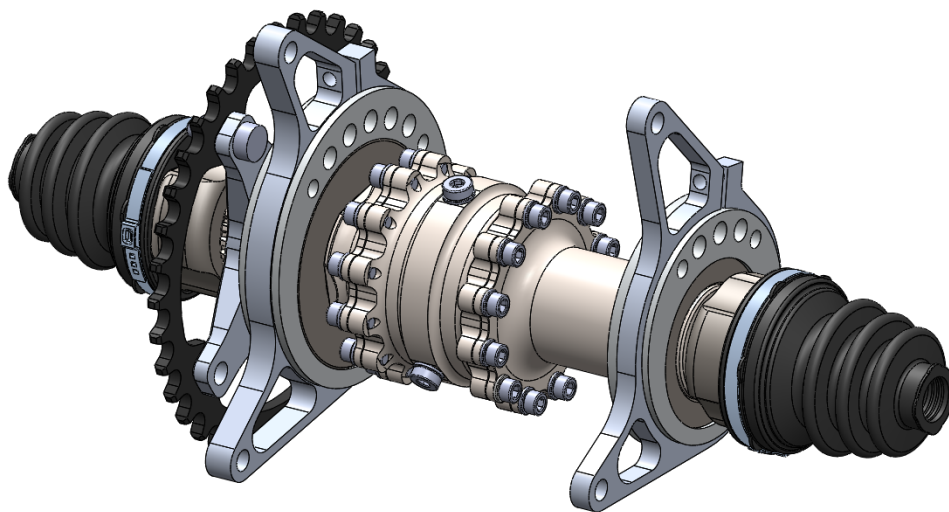
Figure 39. Differential Assembly

Differential Positioning and Tab Design

The differential position relative to the frame is extremely important. Too high, too low, too left, or too right could cause major issues when installing the axles or chain. To reduce the chance of an incorrect offset, mounting tooling was designed. This tooling, seen being used in Figure 40 and Figure 41, helped keep the differential in the correct placement during welding. The tooling was made specifically for this years frame, and latches to the frame bars to hold the differential at the correct height. The differential was then centerlined to the frame, and tabs were welded for final differential installation.

Figure 40: Differential mount tooling

Figure 41: Differential tab welding

Final Drive Ratio Selection

The new engine, the 2018 WR450F, has the same primary and secondary gear ratios as found in the previous engine used in the 2018 competition car. The selection for the final drive ratio of the 2019 car was based on knowledge gained from driving the previous year's car, along with examining the total speed range of each gear. It was because the gear ratios between the two engines were the same that granted the use of driver feedback to aid in determining the final ratio. Considering the primary and secondary gear ratios are difficult to change, since gears are inside the engine crankcase, the best option for altering the gear ratio is by changing final drive, which consists of the combination of the front and rear sprockets. The 2018 Yamaha WR450F utilizes a 5 speed transmission. By examining the ratios of each gear it can be seen that there is a large jump between 1st and 2nd gear when compared to 2nd-3rd and 3rd-4th, seen in table 6.

Table 6: *2018 Yamaha WR450F Transmission Gear Ratios*

Gear	Ratio
1st	2.417
2nd	1.733
3rd	1.313
4th	1.050
5th	0.840

To start the selection of the final drive, the maximum size of each sprocket needs to be constrained. This is done to prevent any interference between the chain on the front sprocket and engine, as well as the chain on the rear sprocket and the frame. Research on the the new 2018 WR450F engine showed that the original front sprocket, located on the engine, had 13 teeth. After comparing several aftermarket part suppliers it was found that the range of front sprockets available for this engine was between 12 and 15 teeth. Based on this information the front sprocket to be selected was constrained to be between a 12 tooth and a 15 tooth. The rear sprocket, if too large, could come into contact with the frame. On the 2018 car the rear sprocket was a 36 tooth from a Yamaha YFZ450 ATV. Due to the positioning of the rear differential there was only a small amount of chain clearance with the frame. The possibility of increasing the size of the rear sprocket was not advisable because of the potential of frame damage if the chain ever became loose and lifted from the sprocket. Positioning of components like the differential can easily be overlooked in the design of the frame. In future FSAE MQP's the frame team should be aware of all subsystems to minimise the potential of frame geometry constraining any subsystem. The 36 tooth rear sprocket fit within the frame and was chosen to be used on the 2019 car. The final drive could be adjusted by changing the size of the front sprocket to increase or decrease the gear ratio.

Driver feedback from the 2018 competition car was that first gear was rarely used mid race, only at the starting line. The highest point earning dynamic events at the FSAE competition are the autocross and the endurance races. The rule book gives average speeds for these two events which were used to determine the final gear ratio, see table 7.

Table 7: *2019 FSAE Competition Rules Dynamic Event Speeds*

	Autocross - Rule D.10.1.1	Endurance - Rule D.11.2.2
Average speed range	40 - 48 km/hr or 24.85 - 29.8 mph	48 - 57 km/hr or 29.8 - 35.4 mph
Max speed	N/A	105 km/hr or 65.2 mph

To select the final drive, the team chose what gears would be used most during these two events and then selected a final ratio that would cover that range. A 12/36 tooth combination and a 13/36 tooth combination were found to be the best candidates for the final drive by plotting the vehicle road speed vs engine

RPM per gear, seen in Figure 42. The road speed was found using the ratio of each gear, the engine's primary ratio, the final drive ratio, and the circumference of the tire. These two ratios would allow 2nd, 3rd, and 4th gear to cover the entire vehicle speed range during the autocross and endurance races while the engine operated within the designed engine powerband range; powerband range discussed more in engine section. The data in table 8 displays that the 12 tooth front sprocket would satisfy the speed requirements of the dynamic events using 2nd, 3rd, and 4th gear while also providing a larger gear reduction to produce more wheel torque. For this reason, the 12/36 tooth final drive was selected for initial testing.
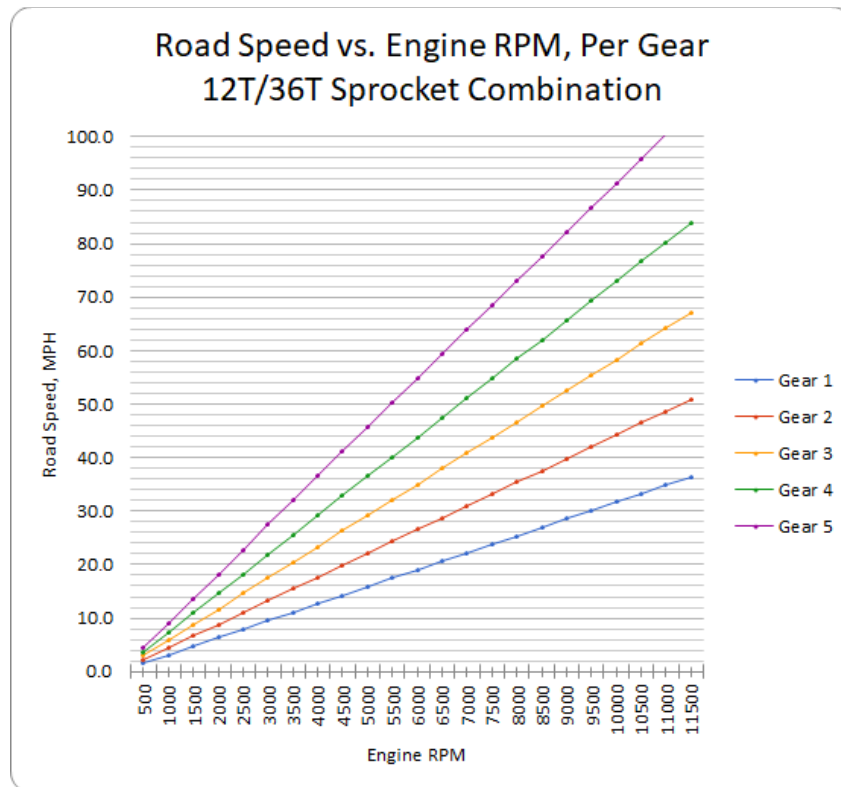
Figure 42: *Road Speed Vs. Engine RPM, Per Gear Plot (Final Drive = 3)*

Table 8: *2nd, 3rd, and 4th gear road speeds for 12/36 and 13/36 tooth Sprocket Combinations.*

Gear - Sprocket	5500rpm	6000rpm	6500rpm	7000rpm	7500rpm	8000rpm	8500rpm	9000rpm
2nd - 12t	24.3mph	26.5mph	28.8mph	31.0mph	33.2mph	35.4mph	37.6mph	39.8mph
2nd - 13t	26.4mph	28.8mph	31.1mph	33.5mph	35.9mph	38.3mph	40.7mph	43.1mph
3rd - 12t	32.1mph	35.0mph	37.9mph	40.9mph	43.8mph	46.7mph	49.6mph	52.5mph
3rd - 13t	34.8mph	37.9mph	41.1mph	44.3mph	47.4mph	50.6mph	53.8mph	56.9mph
4th - 12t	40.2mph	43.8mph	47.5mph	51.1mph	54.8mph	58.4mph	62.1mph	65.7mph
4th - 13t	43.5mph	47.5mph	51.4mph	55.4mph	59.3mph	63.3mph	67.2mph	71.2mph

Testing and Final Selection

After testing the vehicle on several different track configurations with the 12/36 final drive combination it was found that in the lower gears, 1st and 2nd, the drivers had some difficulty smoothly transitioning from decelerating to accelerating. Very little throttle needed to be applied in 2nd gear due to the low gear ratio and when the driver would start applying more throttle it was easy to apply too much and cause a break in traction or an abrupt weight transfer. The effect of this was causing the vehicle to "buck" forward and backward and made smooth driving difficult. The team found that by driving the same track in 3rd gear made a significant improvement in the driveability, but it also seemed to slow the vehicle down when exiting several of the corners.

Two solutions were proposed to improve the drivability in the lower gears. One possibility was that when operating in on-off throttle conditions around peak torque RPM, 6000-7000 RPM, in 2nd gear the power delivery might be excessive and hard to modulate. The main two options were to try the 13/36 tooth final drive combination or to reduce the peak torque in lower gears using a different ignition timing maps. The first option could help by increasing the final drive ratio, effectively reducing wheel torque at the peak torque RPM; when compared to the lower 12/36 ratio. Although this could help smooth the lower gears, it will also increase the speed of each gear, seen in table 8, which could hurt the acceleration. The second possibility to improve the low speed drivability was to decrease the torque in the lower gears. The best method to reduce engine torque is by retarding ignition timing, which is achieved by reducing the amount of the combustion energy transferred to the piston. This would not be an advisable thing to do to the entire ignition map, but the Haltech ECU allows for different maps to be made for each gear. Before the higher 13/36 final drive ratio was tested, the ignition timing in the peak torque range of the 2nd gear map was decreased by 5°. The ignition timing map for 2nd and 3rd gear can be seen for comparison in Figure 43. The results of adding the reduced torque 2nd gear ignition map were determined to benefit the lower gear drivability. This 2nd gear timing map was kept for the 2019 competition. It is recommended to futures teams to explore this more to help improve the drivability, especially if the future vehicles have more power and torque.

Left map (2nd Gear):

Base Ignition Angle °

Ignition - Load psi / inHg

RPM	-29.5	-23.6	-20.7	-17.7	-14.8	-11.8	-8.9	-5.9	-3.0	0.0	1.5
10000	35.0	35.0	30.0	28.1	26.2	24.4	22.5	22.5	25.0	27.5	27.5
9000	35.0	35.0	30.0	28.1	26.2	24.4	22.5	22.0	24.5	27.0	27.5
8000	35.0	35.0	30.0	28.0	26.1	24.2	22.2	21.5	24.0	26.4	27.2
7500	35.0	35.0	30.0	28.0	26.1	24.2	22.2	21.2	23.7	26.2	27.2
7000	35.0	35.0	30.0	28.0	26.1	24.2	22.2	21.0	23.5	25.9	27.0
6500	35.0	35.0	30.0	28.0	26.1	24.2	22.2	20.8	23.2	25.6	27.2
6000	35.0	35.0	30.0	27.8	25.7	23.6	21.4	20.5	22.9	25.4	26.4
5500	35.0	35.0	30.0	27.8	25.7	23.6	21.4	20.2	22.7	25.1	26.4
5000	31.7	31.7	28.0	26.2	24.4	22.8	21.0	20.0	22.4	24.9	25.7
4500	28.3	28.3	26.0	24.5	23.1	22.1	22.0	19.8	22.2	24.6	25.4
4000	25.0	25.0	24.0	22.9	21.8	21.3	22.0	19.5	21.9	24.3	24.5
3500	21.7	21.7	22.1	21.3	20.6	20.5	22.0	19.2	21.7	24.1	23.8
3000	18.3	18.3	20.1	19.6	19.3	19.8	22.0	19.0	21.4	23.8	23.0
2500	15.0	15.0	18.1	18.0	18.0	19.0	18.6	17.2	21.8	21.4	21.0
2000	15.0	15.0	19.0	19.0	19.0	23.6	23.1	21.6	21.0	20.5	20.0
1500	15.0	15.0	15.0	15.0	15.0	21.2	20.6	19.9	19.3	18.6	18.0
1000	16.0	16.0	16.0	16.0	16.0	19.8	19.0	18.3	17.5	16.8	16.0
500	16.0	16.0	16.0	16.0	16.0	18.4	17.5	16.6	15.8	14.9	14.0
Output Value 0	17.0	17.0	17.0	17.0	17.0	13.0	12.0	11.0	10.0	9.0	8.0

Current Gear: gear 1 — 2 — 3

Right map (3rd Gear):

Base Ignition Angle °

Ignition - Load psi / inHg

RPM	-29.5	-23.6	-20.7	-17.7	-14.8	-11.8	-8.9	-5.9	-3.0	0.0	1.5
10000	35.0	35.0	35.0	33.1	31.2	29.4	27.5	27.5	27.5	27.5	27.5
9000	35.0	35.0	35.0	33.1	31.2	29.4	27.5	27.5	27.5	27.5	27.5
8000	35.0	35.0	35.0	33.0	31.1	29.2	27.2	27.2	27.2	27.2	27.2
7500	35.0	35.0	35.0	33.0	31.1	29.2	27.2	27.2	27.2	27.2	27.2
7000	35.0	35.0	35.0	33.0	31.1	29.2	27.2	27.2	27.2	27.1	27.0
6500	35.0	35.0	35.0	33.0	31.1	29.2	27.2	27.2	27.2	27.2	27.2
6000	35.0	35.0	35.0	32.8	30.7	28.6	26.4	26.4	26.4	26.4	26.4
5500	35.0	35.0	35.0	32.8	30.7	28.6	26.4	26.4	26.4	26.4	26.4
5000	31.7	31.7	33.0	31.2	29.4	27.8	26.0	25.6	25.7	25.7	25.7
4500	28.3	28.3	31.0	29.5	28.1	27.1	27.0	25.2	25.3	25.3	25.4
4000	25.0	25.0	29.0	27.9	26.8	26.3	27.0	25.0	25.5	25.0	24.5
3500	21.7	21.7	27.1	26.3	25.6	25.5	27.0	24.6	25.0	24.4	23.8
3000	18.3	18.3	25.1	24.6	24.3	24.8	27.0	24.0	24.5	23.8	23.0
2500	15.0	15.0	23.1	23.0	23.0	24.0	23.6	22.2	21.8	21.4	21.0
2000	15.0	15.0	19.0	19.0	19.0	23.6	23.1	21.6	21.0	20.5	20.0
1500	15.0	15.0	15.0	15.0	15.0	21.2	20.6	19.9	19.3	18.6	18.0
1000	16.0	16.0	16.0	16.0	16.0	19.8	19.0	18.3	17.5	16.8	16.0
500	16.0	16.0	16.0	16.0	16.0	18.4	17.5	16.6	15.8	14.9	14.0
Output Value 0	17.0	17.0	17.0	17.0	17.0	13.0	12.0	11.0	10.0	9.0	8.0

Current Gear: gear 1 — 2 — 3

Figure 43. Haltech Ignition Timing Map for 2nd and 3rd Gear

Sprocket Carrier

The sprocket carrier on the 2019 car was carried over from the previous year. A 2" thick cylindrical blank with internal splines matching the Differential was included with the Drexler purchase. The previous year team had designed and machined the blank into a sprocket carrier that held a Yamaha YFZ450 ATV sprocket. Since the Drexler differential would be reused for the 2019 competition, it was decided to also reuse the sprocket carrier.

Axle Housings

One change to the 2019 Competition vehicle geometry was to increase the overall track width by 2" from the previous year. Many of the components, including axles, from the 2018 vehicle were being reused to save manufacturing time and to help stay within budget. Seeing how the axles were made for the narrower 2018 vehicle, they would not be long enough and a solution would need to be formulated.

It was obvious that the best option was to purchase the correct length axle shafts. The axles from the 2018 car were from Drexler Automotive, located in Germany. The team contacted Drexler for pricing and availability on a set of longer axle shafts and it was found that the new shafts would be approximately $1,200, plus an addition cost if expedited, and have a manufacturing time of around 12 weeks. Due to the high cost and long lead time, the team decided to find a solution to use the axle shafts from the 2018 vehicle.

One solution found was to design a longer outer axle housing. The outer axle housing from the 2018 vehicle was made from 4340 alloy steel and consisted of an opening for the axle tripod bearings on one end and a hex spined section on the other end that engaged with the wheel hub. The tripod bearing of the axle sits inside the housing on machined bearing surfaces and allow the axle to articulate under suspension movement while transferring torque to the wheels. A model of the 2018 axle housing can be seen in Figure 44. Due to this components being under a high level of stress, a detailed analysis was conducted to guarantee the components would not fail under racing conditions. Being made from steel, any extension of the housing would significantly

add to the weight of the part. The objective in the axle housing design was to lengthen the part by approximately 1.5", meet a minimum safety factor of 2.5 during maximum loading, and to keep weight increase to a minimum.

Figure 44. *Axle Tripod bearings and 2018 Axle Housing.*

Several methods for extending the axle housing were explored. The first method involved extending the main body of the housing, and the second was to extend the hub splines and then use a aluminum spacer to position the housing in the correct location. Extending the main body of the housing would have caused an increase of approximately one pound to each housing. This weight increase was considered unacceptable and this design was discarded. The version with the aluminum spacer was considered, but was not selected because of the possibility of the lengthened splines adding additional stress concentrations to the part. The third version of the axle housing consisted of lengthening the main body of the housing, but using a smaller diameter section and then have a flange to contact the bearing. These designs can be seen in Figure 45.
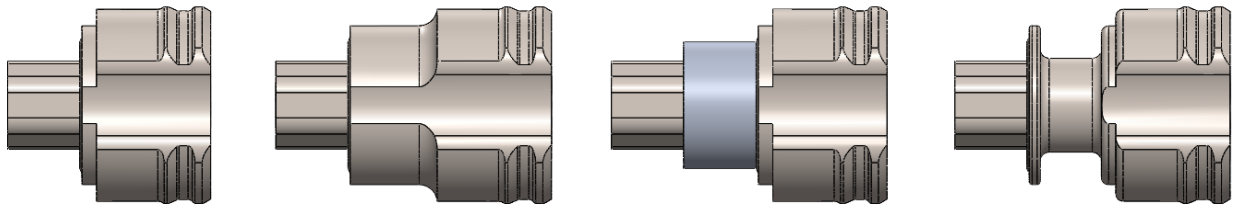
Figure 45: *Axle Housing Designs, 2018 Version on left followed by extended body design, extended spline and aluminum spacer design, and the final design.*

The first step in the stress analysis on the axle housing was to calculate the the applied loads. This was conducted using basic stress calculations and then verified using a SolidWorks FEA analysis. The entire stress calculation and FEA can be seen in appendix C. An assumption was made that the housing would only be experiencing torsional loading because the axle can articulation in the housing. Since the exact engine torque was unknown at the time of the design, the torque on the axles was calculated using two different methods and then the larger of the two was used in the calculations. The first method was to use the wheel torque value that would cause the tires to break free or 'burnout'. The team did not have tire data on the chosen tires, so an assumption on the tires coefficient of friction was selected based on background research. Using a coefficient of friction of 1.5, the normal force of the vehicle, based on the assumed mass of the vehicle, and the radius of the

tire the torque applied to each wheel at break away was approximately 353 lbf-ft. The second method was to use an engine torque value from the 2018 WR450F that was found from a dyno graph obtained online, approximately 33 lbf-ft, and the maximum gear reduction possible. Using the engines 1st gear ratio and the selected final drive ratio of 3, the axle torque value was approximately 317 lbf-ft. The torque value from method one was the larger value and was selected for the calculations. Due to the number of assumptions used to obtain this value, a correction factor or 1.5 was applied to make sure no failure occurs. This resulted in the final axle torque value to equal 530 lbf-ft.

To simplify the analysis, only the section between the spline and the larger diameter portion, where the tripod bearing is located, was analyzed. The bearing surface section dimensions were taken directly from the axle manufacturer and therefore considered not to be a section of concern. A simplified 2D drawing of the housing was created, shown in Figure 34. The dimensions in the drawing were found to be acceptable values to meet the requirements of the part. The dashed line in the center of the part displays the range of the part that will be considered in the analysis. The next step in the analysis was to find the critical section, location of highest stress, within the selected range. It was found that the two highest stress sections would be located at points *a* and *b*, seen in Figure 46.
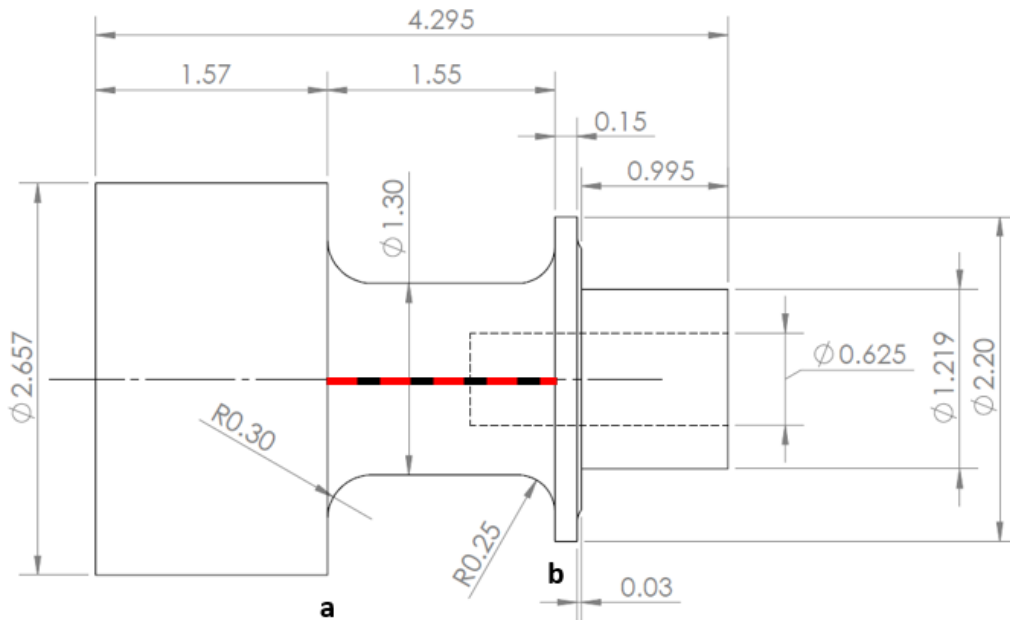
Figure 46: *2D drawing of Simplified Axle Housing. All Units in Inches*

This is due to the smaller diameter and the addition of stress concentrations from the 0.3in and 0.25in radius on the 1.30in diameter section. Since the part was only under torsional loading, the maximum point of stress in any given section would be located on the surface. Next, at section *a* and *b,* the applied stresses and the principle stresses were calculated; being sure to include any stress concentrations. Using the principle stress results, the Von Mises stress at each section was calculated to find safety factors as well as to compare to the results form the SolidWorks FEA.

Von Mises Stress

$$\sigma`_b = \sqrt{\sigma_{1b}{}^2 - \sigma_{1b} * \sigma_{3b} + \sigma_{3b}{}^2} = 32839.18psi$$

$$\sigma`_a = \sqrt{\sigma_{1a}{}^2 - \sigma_{1a} * \sigma_{3a} + \sigma_{3a}{}^2} = 31113.75psi$$

Using 4340 alloy steel material properties obtained from SolidWorks material library the safety factor for the higher stress section, section *b*, was found. The safety factor was calculated as 3.136 using the Distortion Energy Theory and 2.716 using the Maximum Shear Stress Theory.

Safety Factors:
4340 Alloy Steel Properties:
S_{ut} = 160991.89 psi
S_y = 102976.79 psi

Distortion Energy Theory
$$N = \frac{S_y}{\sigma`_b} = 3.136$$
Maximum Shear Stress Theory
$$S_{ys} = \frac{1}{2} * S_y$$
$$N = \frac{S_{ys}}{\tau_{maxb}} = 2.716$$

The calculated Von Mises stress values can be compared to the SolidWorks FEA analysis, found in appendix C. The 3D model was created to match the simplified configuration in order to confirm the results of the stress calculations. The location of highest stress in the SolidWorks FEA was found to be within the radius of the fillet at location b, seen in Figure 47. Images of the final machined axle housings can be seen in Figure 48.

Max: 3.268e+04
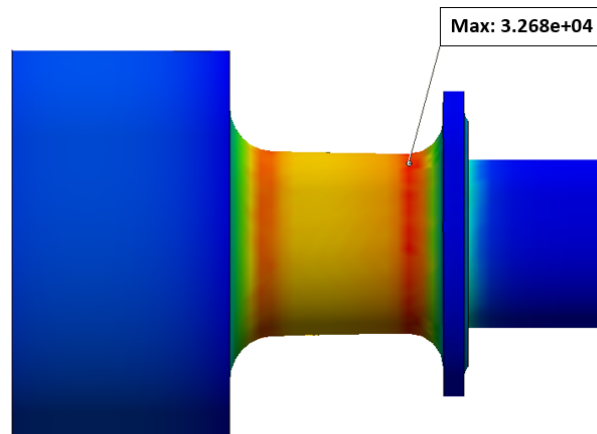
Figure 47: SolidWorks FEA analysis displaying maximum Von Mises Stress Value.

Figures 48: *Machined Axle Housings*

Hand Clutch

The hand clutch is used to break the mechanical link between the engine and the drivetrain, allowing the transmission to move freely. Although the sequential gearbox, linear actuator based shifting system, and centrifugal clutch should ideally limit the frequency with which the hand clutch needs to be engaged, it is still required for launching the vehicle and preventing a stall under full breaking. Last years design used a two piece mount: one for the pivot point of the lever and another for holding the cable cover and overtravel stop. The goal of this years redesign was to create a self contained system which could be placed anywhere along the frame member to the left of the driver to allow adjustment for personal preference.
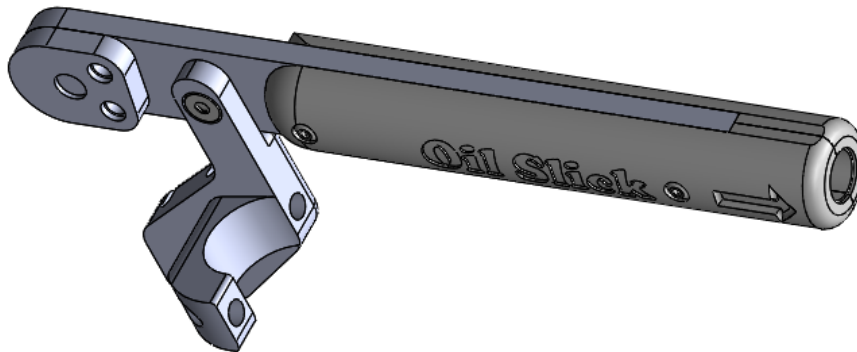
Figure 49: *Hand Clutch Assembly*

In order to reduce compliance in the system and prevent the two mounts from drifting relative to each other, these applications were combined into a single mount, which attaches to the frame via a matching shaft collar. 6061 T6 aluminum was used for this new combined mount. The clutch handle attaches to this mount via a shoulder bolt to ensure smooth operation. To actuate the clutch, a force of 32 lbf must be applied to the steel cable which runs to the transmission. A cover plate with a cylindrical pocket is attached to the handle with two machine screws and serves to tie the cable to the handle. A moment arm of 1 ⅜" exists between this attachment point and the lever, with a 5" moment arm between the pivot and middle of the natural grip point on the lever, resulting in a required driver applied force of approximately 9 lbf.

The lever is completed by two mating PLA grip panels which bolt to the lever. These serve two purposes: providing a more comfortable grip for the driver and serving as a housing for the launch control button, which is located on the end to allow the driver to activate it with their thumb while launching. The wiring for this control is enclosed under the grip panels, protecting it and routing it to the frame where it meets the main wiring harness.

Shifting and Clutch Modifications

The new 2018 Yamaha WR450F engine utilizes an integrated five speed sequential transmission with a multi disk wet clutch. During the various dynamic events in the FSAE competition the driver will be required to shift between the gear positions a significant amount of time due to a multitude of acceleration changes. Since a manual transmission requires an input from the driver to change gear, an amount of difficulty is added to the drivability of the vehicle. This difficulty is mostly associated with the driver needing to remove their hand from the wheel to pull a shift lever to change gear position. The addition of an actuator to the engines shifter shaft can greatly improve the driveability of the the vehicle by allowing the driver to change gear position by pressing "paddles" or buttons on the steering wheel to either upshift or downshift. The past MQP teams have utilized pneumatic linear actuators as well as electronic linear actuators to improve the shifting system. Both methods have proven successful, but the complexity and large number of components in the pneumatic system have made it less desirable for the the 2019 Team. The pneumatic shifting system that was used on the 2016 vehicle required two pneumatic actuators, an air tank, an air compressor, control solenoids, and a purpose built computer to control the air supply and the actuator timing. The 2018 MQP team decided to move away from the pneumatic shifting and changed to a fully electronic system. Their first attempt to control shifting was to use a geared motor to rotate the shifter shaft. The main issues found with using this motor was that it would need to change directions for upshifts and downshifts and also stop its rotation when the chosen gear engaged. Due to the large amount of force required to change gear position a geared motor was chosen. The gearbox of this motor could not be back driven. In order for the motor to shift, it would need to rotate to the gear change position and then rotate the opposite direction to return to it natural position. To achieve this, an electronic device was developed to track the motors location so it could know where to stop. After many design iterations with this system it was found to be to problematic and a new device to control the shifting was found. To replace the motor the 2018 team purchase a Pingel Electric Speed Shifter, which is a electronic linear actuator designed to shift sequential transmissions in motorcycles, seen in Figure 50. The final results from the 2018 team using this shifting system showed great potential and was recommended to use in the 2019 season due to its simplicity and function.

Figure 50: *Pingel Electric Shifter Actuator*

Initial Mechanism Designs

To connect the pingel to the shifter shaft of the engine, a 4-bar linkage was used. A crankshaft was fitted to the engine shifter shaft. The crankshaft has a lever arm which the Pingel operates, pushing or pulling to change the gear based on the input from the paddle shifters. The engine shifter shaft takes about 4.48Nm of torque to shift the transmission; thus, the pingel and crankshaft must produce at last 4.48Nm of torque and rotate 14 degrees to reliably shift the car. The Pingel produces 30lbf when the actuator travels from the center to either the far back or far front side (1.25in); depending on the travel direction. If the actuator does not travel the full distance, the full 30lbf is not produced. These factors were the driving design constraints of this assembly.

The resulting design is pictured below in an AutoCAD 2D kinematic layout showing the three different positions: mid upshift, mid downshift, resting. Mid upshift is in blue, mid downshift is in red, and resting is in black. The Pingel does not travel the full 1.25" on either stroke, but, because of the length of the lever arm, the pingel still provides enough torque to reliably shift the car.
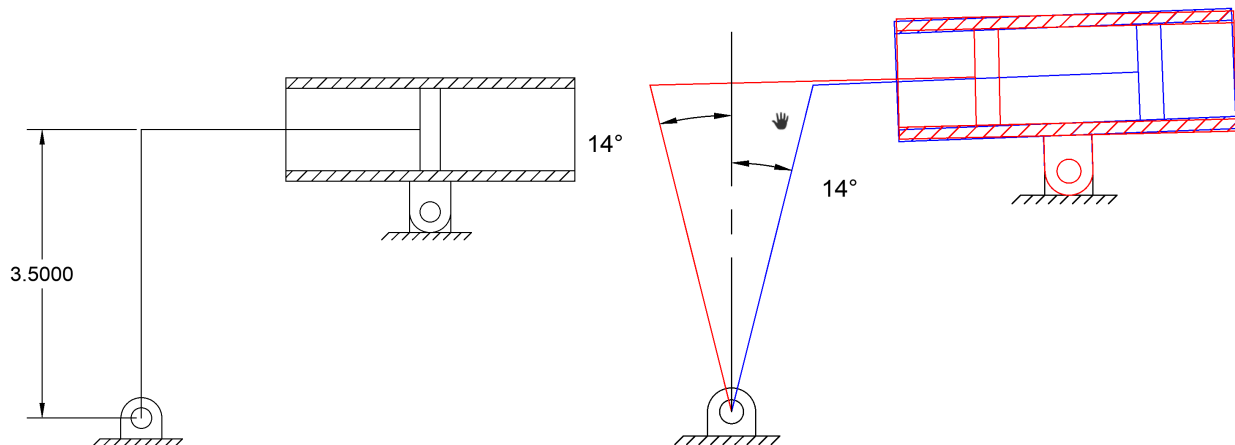
Figure 51: *Linkage kinematic sketch at rest.*

Figure 52: *Linkage in mid upshift (blue) and downshift (red).*

In this configuration, the Pingel travels about 0.875" in either direction. This is not the full travel; however, assuming the Pingel provides all 30 lbf (133.5N), the torque produced is 8.73 ft-lb (11.8Nm). This is more than twice the amount of required torque to shift the car.

Solid Model

To develop the shifting crankshaft and the associated mounts, SolidWorks was used. The shaft extends from the base of the engine connection to the perpendicular frame tube. On the frame tube, an adjustable mount holds a bushing PTFE bushing concentric to the shaft. This mount helps stabilize the shaft and reduce and bending moments and deflection while shifting. The shaft is constructed of a yamaha shift lever spline, an aluminum shaft, and a lever arm welded to the shaft. The Pingel and the lever arm arm are joined by a 0.25" shoulder bolt. The single shear method is used in this application due to packaging restrictions. The issues with double shear are either the Pingel will either interfere with the axle or chain, or the lever arm will interfere with the frame. The only solution was to make the shaft in single shear to properly fit it in the car. To test the strength of the single shear, dynamic FEA was performed in SolidWorks.
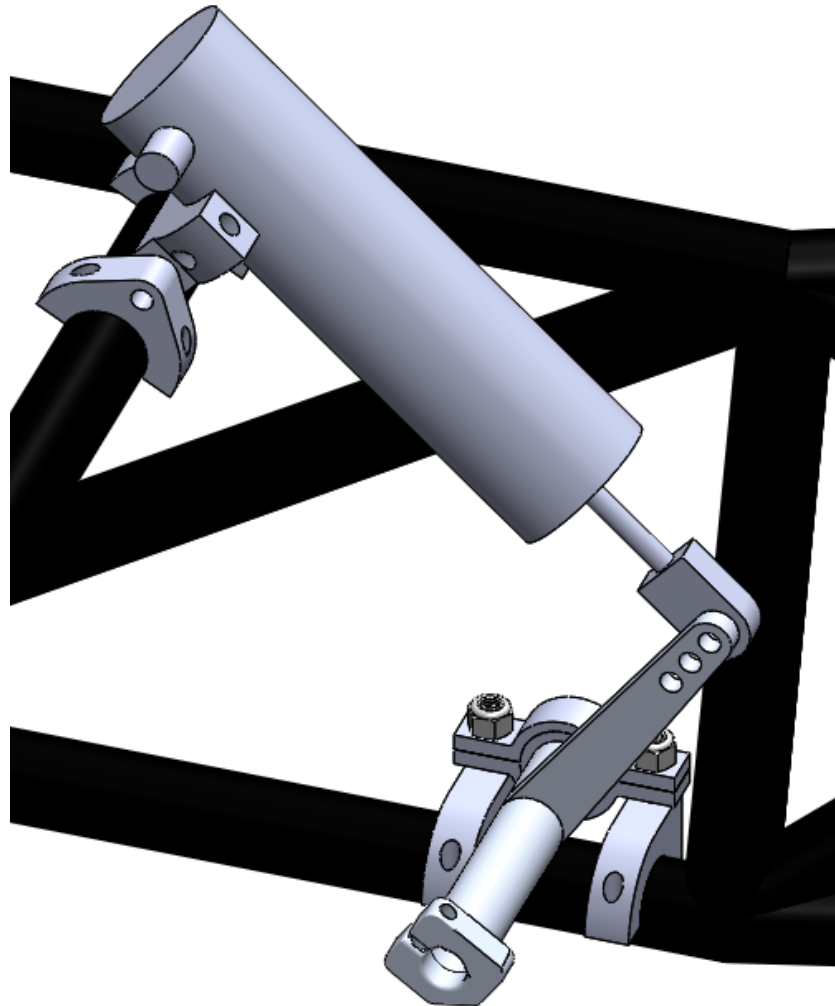
Figure 53: *Shifter assembly in SolidWorks.*

In the FEA, a force is applied concentric to the Pingel, acting on the inner diameter face of the the shoulder bolt hole. The spline is fixed to simulate the resistance before the shifting shaft rotates. The bushing on the other end is represented by a roller/slider fixture. The FEA yielded a minimum safety factor of 1.6.
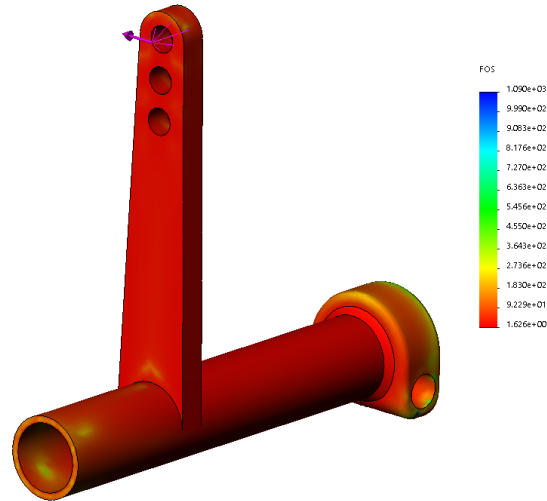
Figure 54: *FEA of shift lever.*

Shifting Controls and Electronics

The 2019 vehicle will use the Pingel electronic actuator to control the shifting. The wiring for the Pingel is quite simple, requiring only three wires to control the up and down shifts. One constant power wire is connected to the actuator and then one of the other wires is grounded to activate the shift lever. When the other wire is grounded, the direction of actuation is reversed. When neither wire is grounded, the actuator floats freely with little resistance and allows the internal spring on the shift shaft to return it to its natural position. To activate the Pingel a circuit consisting of a 40A fuse (or circuit breaker), two 5 pin relays, and two micro switches was developed. This circuit is extremely simple and essentially activates the actuator whenever the switch is held, which is not the best method since the the fuse will burn out if the paddle is held for to long. It was recommended by the Pingel company to use 40A fuse even though the actuator itself can draw up to 150A of current. The reason the 40A does not instantly burn out is because although 150A is being drawn during each shift it is only for a short amount of time. The 40A fuse is a "slow blow" type and is able to withstand the high current for a few seconds before burning out. See Figure 55 for the shifting wiring diagram.
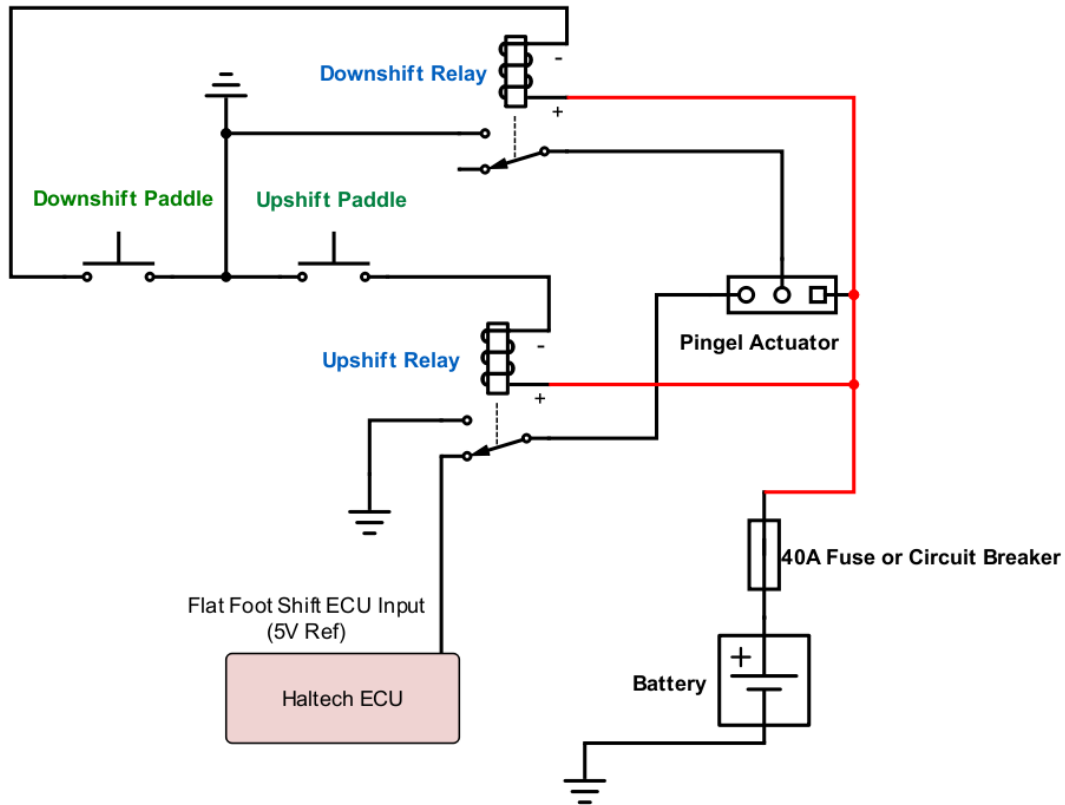
Figure 55. *Shifting Wiring Diagram* [20]

The paddle shifters were designed and manufactured by an SAE club member. Each shifter assembly consisted of a 3D printed base and paddle. The micro switch attached to the base is activated when the paddle is depressed by the driver. To hold the paddle away from the micro switch, a strong magnet was installed into the base as well as the paddle. Once the paddle is activated and released, the magnets attract and immediately pulls the paddle back to the base. Figure 56 show an image of the paddle shifter assembly.

Figure 56: *3D Printed Paddle Shifter Assembly*

A gear indicator sensor was designed and based on the factory Yamaha neutral position sensor. This sensor consisted of a CNC machined delrin body with six integrated copper pins that were ground flush with the face of the body. The sensor is fixtured to the side of the engine crankcase and a pin protruding from the transmission shift drum creates a connection between each pin and the engine (Ground) depending what gear is selected. To differentiate between each gear, the sensor was wired as a voltage dividing circuit. Each pin was connected to a resistor and the other end of each resistor was connected to a single wire leading to the ECU. Haltech incorporated a 1K OHM pull up resistor into the analog input pins, therefore the voltage drop through each of the resistors could be measure and indicate the current gear. Haltechs analog pins are 5V reference so the six calculated resistance values (gears 1-5 and neutral) needed to provide even voltage drops were a 166.6 OHM, 400.2 OHM, 750.1 OHM, 1333.2 OHM, 2499 OHM, and a 6002.8 OHM. Resistors with the approximate calculated resistance values were sourced and soldered to the sensor's copper pins. The largest resistor was connected to the 5th gear and then repeated on the rest of the pins ending with the smallest resistor being soldered to the 1st gear pin.

By implementing the shift sensor it was possible to output the current gear onto the Haltech RacePak IQ3 dash unit. This helped to inform the driver if there was any misshifts. It also gave the ability to created different ignition timing maps in each gear to improve torque delivery, as discussed in the shifting section. An image of the shift sensor model and the pin resistors can be seen in Figure 57.
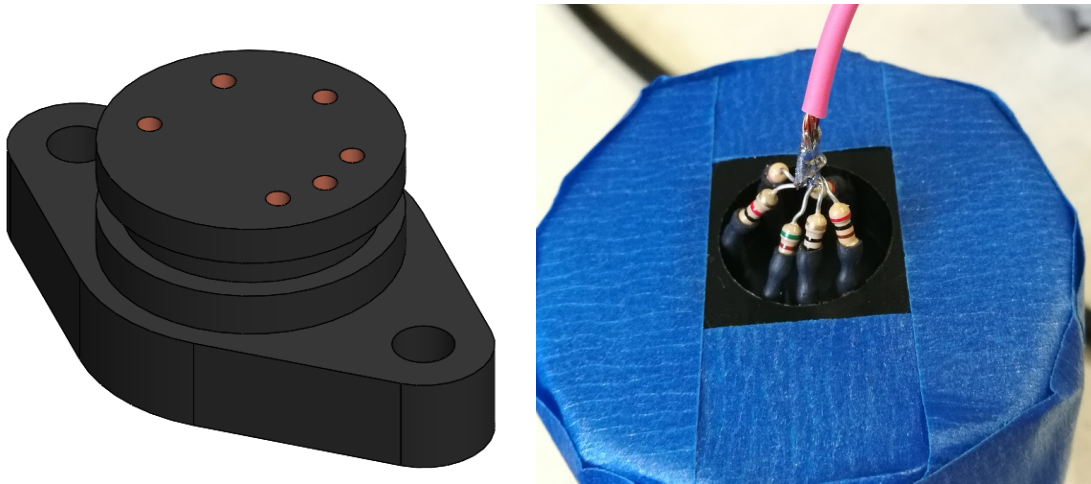
Figure 57: *Shift Sensor model and Shift Sensor Pin Resistors Before Epoxy Potting Compound*

Clutch modifications

A major issue experienced by the 2018 team was from rear wheel lock up while downshifting to low gear, such as from 2nd to 1st. The solution to this problem was to add a back torque limiting clutch, commonly known as a "slipper clutch". A back torque limiting clutch was utilized for the 2019 vehicle because of the success of the previous year.

The 2018 WR450F engine used in the 2019 vehicle included a 5 speed sequential manual transmission. This type of transmission shifts between the gears in order, unlike an "h pattern" transmission which can move directly from one gear to any other gear. The main benefit of the sequential transmission is that it can be safely shifted without using the clutch. It only requires a quick interruption of engine torque, such as letting of the

accelerator. This can easily be accomplished on upshifts by using the ECU to cut the ignition for a split second, between 100-300ms, while shifting under power. Clutchless downshifts are a little more difficult to achieve without rear wheel lockup. The cause of the wheel lock up comes from the difference between the engine speed and wheel speed once the lower gear engages. When the car shifts from second to first the wheels are normally rotating much faster then the engine and once first gear engages the engine must quickly accelerate or the wheels must quickly decelerate. Since the car is likely decelerating during downshifts and there is no throttle input, the latter is more plausible and results in the rear wheels slowing down so much that skidding occurs until there is an equilibrium between the engine and wheel speeds (equilibrium speeds relative to gear ratio). To help solve this problem, a back torque limiting clutch from a Yamaha YFZ450 was implemented into the new WR450F engine, the same as the previous year. This type of clutch is designed to slightly disengage or "slip" when the rear wheel speed is higher than the engine speed, during downshifts or engine braking. By slipping the clutch a small amount the engine and wheel speed has more time to equalize and the amount of rear wheel lockup is reduced. The yamaha YFZ450 clutch utilizes a ramps on the pressure plate and the inner hub. During deceleration the pressure plate slides up the ramp or the inner hub, decompressing the clutch pack. A diagram of this type of clutch can be seen in Figure 58.
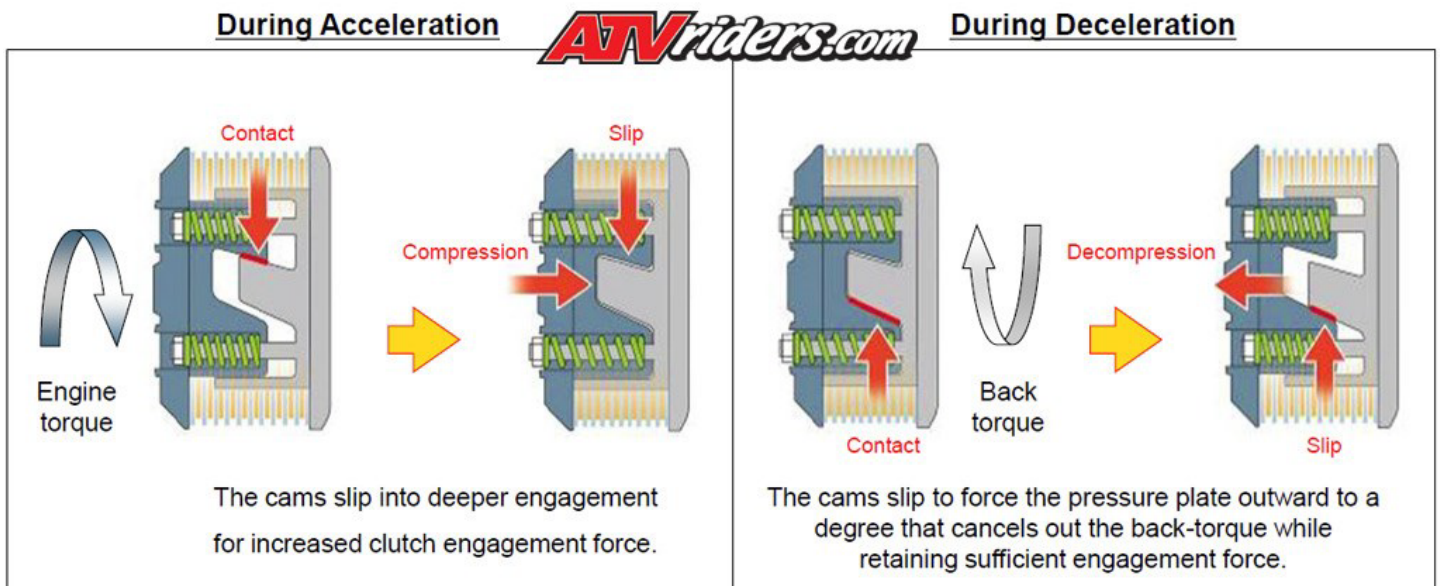
Figure 58. *Workings of an Assist and Slip Clutch (atvriders.com)*

The engine used in the 2018 competition car was from a 2015 Yamaha WR450F and the slipper clutch components used in the their car were from a 2014 Yamaha YFZ450. To check if the YFZ clutch components could be used in the new 2018 WR450F engine the part numbers of the 2015 and 2018 engines were compared and found to be the same. This meant that the same YFZ450 slipper clutch components used in the previous years 2015 WR450F engine could also be used in the new 2018 WR450F engine. In the 2018 FSAE MQP report [*Design and Optimization of a Formula SAE Vehicle - 2018*] a detailed table of the components needed to install the YFZ450 clutch into the WR450F engine was created and can be referenced by future teams to see the what Yamaha components are required.

For the 2019 competition vehicle only the slipper components from the YFZ450 were used (Inner hub and pressure plate). Instead of using the clutch disks from Yamaha a complete clutch pack assembly from Rekluse was used. The Rekluse clutch includes a special clutch disk that allows the clutch to automatically disengage at low engine speeds. The Rekluse EXP disk uses centrifugal force to engage and disengage the clutch. Figure 59 shows a diagram of the Rekluse EXP disk. Figure 60 displays images of the before and after installing the Yamaha YFZ450 slipper components and the Rekluse EXP Torque drive clutch assembly.
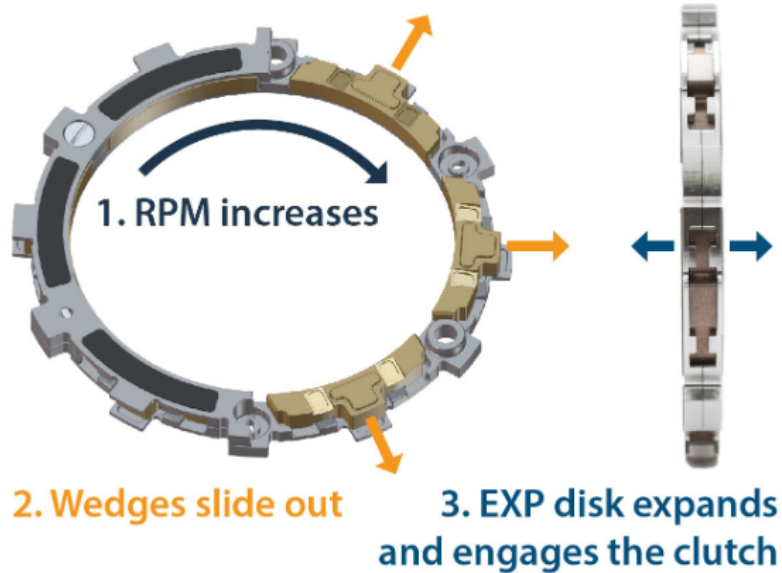
Figure 59. *Rekluse EXP Auto Clutch Disk* [21]
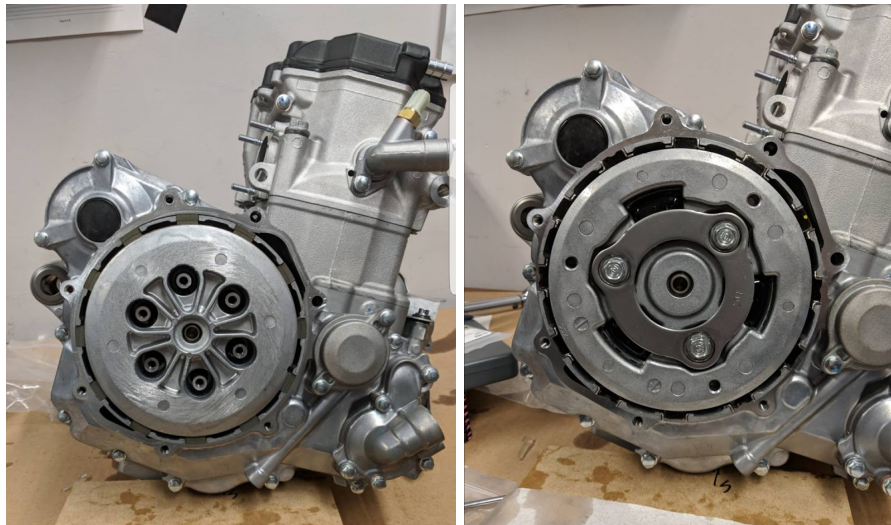
Figure 60: *Before and After Slipper and Rekluse Clutch Installation*

Testing Results and Future Recommendations

As with the 2018 competition car, the addition of the slipper clutch components greatly improved the drivability of the vehicle. No rear wheel lockup was noticed during downshifting, even when shifting into 1st gear. It is highly recommended to use a slipper clutch in any engine used in the future. The information in the 2018 and 2019 FSAE MQP reports will give all necessary information needed to convert the Yamaha WR450F or YZ450F engines.

The Rekluse auto clutch was easy to install and while driving it did not seem to make the car operate any different than the factory clutch, a good thing. Since this clutch was designed for the factory 2014 Yamaha YFZ450 the engagement point for the auto clutch disk should be around the stock idle RPM, about 1900 RPM. The engagement point could be adjusted to a higher RPM by installing stiffer disk springs, which were supplied with the clutch. It was difficult to obtain a steady idle close to the factory value so the stiffer gold springs were installed into the disk to obtain the highest engagement point. This setup seems to engage the clutch around 2300-2400 RPM. During several drives the Rekluse clutch worked perfectly and allowed the driver to start and stop the vehicle without any use of the clutch lever, but due to the difficulty in finding a steady idle it was hard to use it consistently. When the car was idling in gear with the clutch disengaged there were many random RPM surges which would cause the clutch to engage and the car to either move or stall. This product would greatly improve the drivability of the vehicle by allowing clutchless starting and also reduce the possibility of engine stalling during wheel lockups. Future teams should strive to gain a more consistent idle RPM in order to improve the consistency of the auto clutch engagement.

One possibility for future teams to investigate is directly control on the transmission to control shifting. The shift shaft and components inside the engine were designed to include the motorcycles shift lever and to allow the rider to downshift one gear by pressing the lever down and upshift one gear by pulling the lever upwards. If all the components associated with the shift shaft were removed from the engine the shift drum could then be rotated by an actuator outside the engine, such as a servo motor. The current gear indicator sensor mounts to the engine's crankcase, concentric to the shift drum, and its mounting location could be used as the shift drums motor mounting location instead. Directly controlling the shift drum would be able to improve the accuracy of the shifting system because it would be able to turn the drum and shift forks to the each gears exact location. This system could also include an encoder to measure the exact location of each gear and could potentially be programed to shift shift multiple gears at once. Other benefits would be the ability to easily locate neutral with the push of a button and minimizing the amount of misshifts.

Engine Performance

One major area of interest for the 2019 competition year was to increase engine performance. Past years have shown that the power output produced was relatively low when comparing to the vehicles of many competing teams. Another issue past MQP teams have faced is lack of documentation on each of the different systems in the powertrain.

To assist future FSAE teams, the 2019 team has heavily relied on industry standard simulation software packages. In the past students have developed their own simulations and although impressive the simulation is specific to a particular engine configuration and are difficult to redevelop for a new engine. The results of these

simulations can be easily documented, but the procedures used to develop the simulation itself create great difficulty in documentation. In order to both simulate the current engine and create models that can be used by future teams for experimentation, a standard Ricardo WAVE license has been acquired. Ricardo WAVE is a form of one dimensional engine simulation software, useful for basic examination of engine operating conditions, as well as exploring the effects of various engine performance concepts. The software primarily utilizes fluid dynamics and thermodynamic calculations to analyze pressure waves, mass flows, and energy losses within the ducts, plenums, and manifolds of an engine to enable performance evaluations to take place with various component configurations. This has been especially important with understanding the effect of exhaust and intake tube lengths and diameters, and the end result they have on changes to torque and horsepower values for the engine. The various dimensions, material properties, and performance specifications of the 2018 Yamaha WR450F have been measured and implemented into the parameters required by WAVE, which allows us to gain an understanding of what changes to the engine will prove most optimal for performance, while also allowing future teams to modify the engine model as they see fit to validate any powertrain changes they may make.

High Compression Piston

One of the first engine modifications under consideration was the implementation of a high compression piston for the WR450F engine, in order to provide an increase in horsepower and torque across a wide range of engine speeds. The stock compression ratio of the WR450F engine is 12.5:1, while the Wiseco piston eventually selected increases this to 14:1.

Figure 61: *Yamaha and Wiseco Pistons, & WR450F Pentroof*

The method in which the gas and air mixture becomes more compressed in higher compression ratios is affected by a reduction in clearance volume, or the volume of the combustion chamber when a piston is TDC. The compression ratio itself can be described as the sum of this and swept volume, or volume taken by an entire piston stroke, then compared to clearance volume. Thusly, for every sum of swept and clearance volume within the combustion chamber, there are 14 clearance volumes fitting within that summation for the project vehicle.

This is evident in Figure 61, as one could see the Wiseco piston had a higher zenith height tapering towards a peak, unlike than the standard Yamaha WR450F piston. This pointed face becomes flush with the pentroof as seen in the same figure, resulting in higher temperatures and pressures reached within the combustion chamber. This increase in pressure and temperature leads to a rise in power due to the more thorough combustion of the air fuel mixture taking place. While engine knock as well as pre-ignition of the fuel would be a concern with high compression pistons, this was a non-issue due to precautions taken during engine testing. Not only did the 100 octane race gas used in the car over the U.S. standard of 94 octane premium assist, but a safe base Haltech tune was utilized during dyno testing with incremental changes in ignition timing, as explained later in this report. Thusly, the Wiseco high compression piston was installed and utilized with minimal risk, while playing a significant role in the goal of increasing power and torque for this year's FSAE vehicle.

Air Intake

Background Research

A goal for this year's vehicle was an increased level of validation for a newly developed intake system that would help provide power at the RPMs demanded. Research primarily consisted of determination of runner lengths, plenum sizes, and restrictor flow for the car, validated through physical calculations along with multiple software packages including SolidWorks Flow Simulation and Ricardo WAVE. The demand of air required for combustion varies in synchronicity with engine speeds, yet the intake system can be altered in such a way that air flow can be optimized for certain RPMs. This can be taken advantage of to increase power and torque at speeds believed to be most useful or frequently used on track. For this car, a goal was to optimize the intake and exhaust system to produce peak torque at 6000 RPM, as this was a middle ground between the WR450F's approximate operating speeds of 2000 and 10,000 RPM. In the moment an intake valve closes, air flow into the combustion chamber is halted, and a pressure wave is formed that reverses direction and travels upstream within the intake. Once either the atmosphere or an area of a sudden and significant change in piping diameter has been reached, the pressure wave will yet again reverse and travel downstream. This back and forth flux can be predicted, calculated, and timed, providing denser air arriving with the pressure wave, and a better volumetric efficiency at selected RPMs thereafter. This tuning is based on Helmholtz resonance, and is typically referred to as pulse or pressure wave tuning.

While formulas for intake resonance tuning do exist, none are all encompassing for various engine types, and therefore were only used to approximate various runner test lengths to use on a dyno. General knowledge suggests that the longer a runner is, the further down in engine speeds peak torque will be made, while the opposite is true for a shorter runner. Two books were studied in order to further understand pulse tuning, being David Vizard's *How to Build Horsepower*, and Phillip H. Smith's *Scientific Design of Exhaust and Intake Systems*. Formulas were derived from each, providing similar results for intake runner length, with a means to determine which lengths were viable to test both physically and simulation.

David Vizard's formula provided the longer length of the two calculated, with an all encompassing length that begins at the valve openings and heads to the area of pressure wave dispersal.

$$L = \frac{(720 - ECD) * 0.25V * 2}{RPM * 2} - 0.5D \qquad\qquad L = \frac{(720 - 291) * 0.25(1100) * 2}{6000 * 2} - 0.5(1.65) = 18.8in.$$

ECD = Effective Cam Duration (291 Degrees)
V = Pressure Wave Velocity (1100 ft/sec)
D = Pipe Diameter (1.65 inches)

Phillip H. Smith's *Scientific Design of Exhaust and Intake Systems* formula was less detailed, yet could potentially be the base of development for the previous formula.

$$L = \frac{72C}{RPM} + 3 \qquad\qquad L = \frac{72(1100)}{6000} + 3 = 16.2in.$$

C = Pressure Wave Velocity (1100 ft/sec)

These runner length calculations acted as the base of not only tested lengths within Ricardo WAVE simulation, yet had the additional benefit of helping determine varying pipe lengths required for successful dyno tests once validated.

Plenum

Within the intake system, plenums play the vital role of ensuring a quantity of air is available for the engine to optimally operate at a variety of speeds. Placed between the restrictor and runners, the plenum functions as a FSAE rule compliant air reservoir, alleviating power decreases that arise with a mandatory maximum restrictor diameter of 20 mm as per FSAE IC.2.4.3. Since the area in which air travels through is heavily constrained, this air is allowed to congregate within this container, especially at time of low RPM. Due to this, the key attribute to a single cylinder plenum design is its volume over all else. A cylinder was chosen as the final shape due to its symmetry, as well as its effect on intake runners further downstream when compared to spherical designs. The bottom of this plenum functions acts as the end of the intake runners, as the near 7 inch inner diameter of this cylinder provides for a drastic enough diameter change to disperse a pressure wave primarily travelling through a 1.63 inch runner. Due to its primary function, the key attribute of its design is focused on volume.

Figure 62: *Intake test configuration.*

Two plenum sizes were tested on the dyno as seen in Figure 62 in its 3.6 L configuration. A 2.5 L setup was also configured, involving removal of the black 3D printed centerpiece.   The dimensional printer constraints as well as intake packaging FSAE rule IC.1.2 prevented larger volumes from being explored. Theoretically, plenums linearly increase engine power as volume grows, yet this fails to mention how throttle response may be hampered due to a drastic reduction in air velocity that occurs when this volume increases. Since key factors such as this response are important for acceleration and thusly performance on track, it is important for these air reservoirs to not hinder this performance quality. Two plenum sizes were produced to safeguard against this detriment, while also ensuring no advantages in power were avoided.

Restricted Air Intake Theory of Operation

FSAE rule IC.2.4 states that any vehicle running gasoline as fuel must utilize a 20 mm diameter restrictor. Within that constraint, the converging and diverging angles may be adjusted in order to limit the hampering of mass flow rate that the restrictor nozzle causes. This is also referred to as choked flow, a point where the velocity of gas flow through an orifice has reached sonic conditions, and can increase no further. What determines whether or not this limit is reached for De Laval restrictor nozzles is the ratio between downstream and upstream pressures. The absolute pressure ratio is 0.528, where downstream pressure is 52.8% of upstream pressure. (26) The restrictor from last year's vehicle has carried over to the present, as it met FSAE rule standards, yet this was not decided without additional validation. The mass flow rate calculated by last year's team was done in detail with 2016 WR450F engine specifications in mind, with the 2018 WR450F following suit with the same volume and RPM range. Therefore, last year's validation theoretically proves valid for 2019, yet there was room for improvement by verifying delta pressure is within the choked flow ratio.
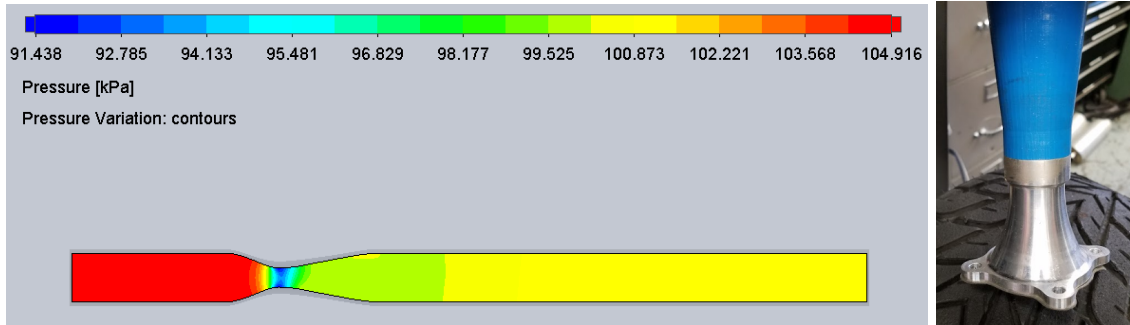
Figure 63: *Restrictor Choked Flow Validation and Restrictor*

Solidworks Flow Simulation was utilized to confirm delta pressure. While the restrictor simulation isn't reflective of the final iteration by extending 10 inches downstream as seen in Figure 63, this extension does expose pressure behavior if longer intake piping near the restrictor were to be utilized by future teams. Pressure downstream was recorded at a maximum of 104.9 kPa, and an upstream maximum pressure of 101.3 kPa. This in fact translates to a ratio of 0.966, far above the ratio limit for choked flow. Due to the current restrictor being rule compliant, the difficulties of remanufacturing of a new metal converging angle section, and engine performance goals being exceeded significantly nonetheless, the team moved forward with last year's restrictor.

Design and Concept Refinement

The first step in the intake design was to constrain the size and location of the intake. According the the the FSAE rule IC.1.2 the air intake system and fuel system is constrained within the surface defined by the top of the roll bar and the outside edge of the four tires in a side view and rear view. The air intake system includes the throttle body, the intake plenum, the restrictor, any airbox if used, and the air cleaner. To be sure no part of the intake system was outside the surface envelope construction sketches were added into the full car assembly and used as guides while designing the intake components and finalizing their locations. The surface envelope can be seen in Figure 64.
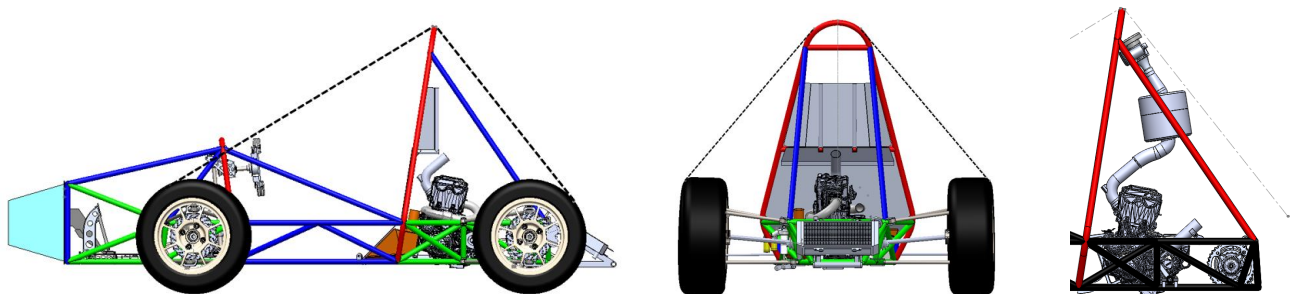
Figure 64: *Intake Surface Envelope, and Final Intake System Packaging*

Once a runner length extension of 6.5 inches from the end of the intake injector tube to the plenum was determined, work was done on making sure that length would comfortably fit within the intake surface envelope as seen in Figure 64. The curvature of bends was kept at a minimum to ensure flow wouldn't be severely affected, while also maintaining packaging constraints.

Prototype Intake Design and Manufacturing

Starting at the engine, the first piece of the intake system was the injector tube and mounting flange. According to rule IC.2.3.1 the intake manifold must be securely attached to the engine block or cylinder head with brackets and mechanical fasteners. The use of hose clamps, plastic ties, or safety wires do not meet this requirement. From the factory the WR450F engine has a rubber and aluminum flange or "boot" that is retained to the engine with two fasteners. The cylindrical rubber section of the boot connects to the factory intake by tightening the boot around the intake with a hose clamp. To satisfy the rules this method can not be used because the hose clamp is not considered a suitable mechanical fastener. The factory intake boot can be seen in Figure 65.

Figure 65: *Factory Yamaha Intake Boot*

To eliminate the rubber boot an aluminum flange was designed to attach to the engine with the factory fasteners. The flange was welded to an 2" aluminum 90° tube which would be the first section of the intake runner. The fuel injector mount was machined from aluminum and was designed to sit tangent to the bend of the aluminum tube and locate the injector concentric to the engine's intake port. Completed intake flange and injector tube seen in Figure 66.

Figure 66: *Intake Flange and Injector Tube*

Physical Testing and Refinements

Once theoretical dyno configurations were established, the team proceeded with gaining performance numbers during dyno testing. A base Haltech tune was established to safely operate the car on the dyno and slowly improve the tune based off of intake configuration changes. Runner lengths tested included virtually no runner, defined as a small 4 inch bend directly into the metal injector tube, as well as a 2.5 and 5 inch extension. A 10 inch extension was additionally tested as an outlier to provide further validation. It is important to note that these extensions are a component of total intake length calculated and simulated. A rough total length of 8 inches from the injector runner, and 2 inches of intake valve tubing must also be included. Accommodating this, lengths tested were a 10 inch, 12.5 inch, and 15 inch runners, with a 20 inch long outlier.

Figure 67. *Dyno Testing*

Dyno testing validated developmental work done previously, as peak power for the configuration decided upon was 47 horsepower, with a peak torque of 31 lbs-ft at 6000 RPM confirming work done for intake modelling and simulation. As it turns out, a runner length extension of 2.5 inches proved to be the optimal setup, yet was the second most powerful overall. The no runner extension produced the highest peak power by a few tenths of a margin, and produced a more erratic torque curve than the 2.5 inch setup, which confirmed the latter was better than the former for the sake of driveability.
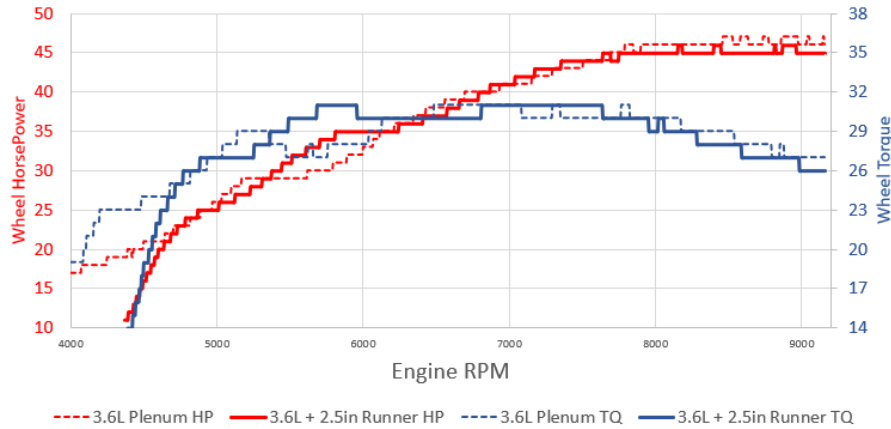
Figure 68. *Runner Length Dyno Test*

As expected, the larger of two plenums was superior, and through driver feedback, has been validated to have no discernable negative effect on throttle response. The power and torque curve as seen in Figure 68, were drastically smoothed for the 3.6 L plenum, while an increase of approximately 6 hp was observed. Due to this, the 2.5 L plenum was not tested for all runner lengths, and was excluded from 2.5 and 10 inch extension tests.
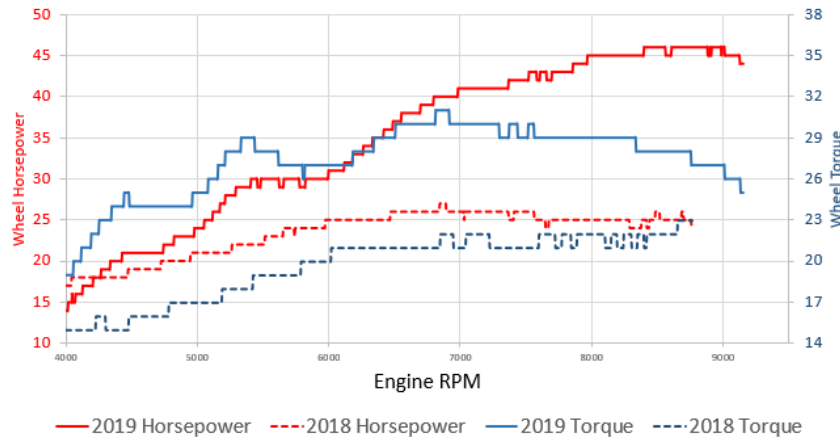
Figure 69: *2018 vs. 2019 Powerband Comparison*

When compared to the previous year's performance characteristics, it is evident that this year's vehicle has exceeded the goal of a 9 hp increase from last year's numbers, with a significant increase in peak torque at the desired 6000 RPM.

Future Recommendations

While extensive research was invested into intake systems, further validation could occur to improve air flow to the engine. While volume was considered one of the few key attributes of the plenum, the shape and construction of the component could be further validated. Ribs exist to prevent flex during changes in interior pressures. While modelling of interior faces was smoothed for the sake of better flow, this was done out of general knowledge that air flow is improved on smooth surfaces. It is unknown whether or not bottom sides of the plenum should concave in for the sake of increasing air velocity further downstream, for example. Besides

validation of plenum shape, the restrictor should especially be improved upon, as choked flow seems to be occurring on the basis of a delta pressure ratio above 0.528. Converging and diverging angles should be observed for the current model, and other angles experimented with. Additionally if peak torque is desired at an engine speed other than 6000 RPM, calculations done to assist with intake runner length determination should be redone, with step by step improvements investigated along the way.

Exhaust Tuning

Header Piping Calculations and validation.

While intake systems had the benefit of being easily adjusted during testing using 3D printed components and polyurethane tubing, the exhaust system's header pipe length would have to be determined earlier on, due to the high cost and manufacturing time required to produce and test various exhaust pipe lengths. A. Graham Bell's *Performance Tuning in Theory and Practice, Four-Strokes* was investigated, with formulas derived from the book being utilized to find a base exhaust length for WAVE simulation.

$P = (850(ED) \,/\, RPM) \,-\, 3$ $\qquad\qquad$ P = Pipe Length (in.)
$P = (850(254) \,/\, 6000) \,-\, 3$ $\qquad\qquad$ ED = Angle range in which exhaust valve is open.
$P = 33 \; in.$

$ID \;=\; (\sqrt{(cc \,/\, (P+3)25)}) * 2.1$ $\qquad$ ID = Inner Exhaust Pipe Diameter
$ID \;=\; (\sqrt{(449.3 \,/\, (32.98+3)25)}) * 2.1$ $\qquad$ cc = Cylinder Volume (cm^3)
$ID \;=\; 1.5 \; in.$

As validated by Ricardo WAVE simulation, a 6 inch runner extension was required in order to achieve exhaust resonance tuning optimized for 6000 RPM peak torque. This would result in a total header pipe length of 39 inches.

Header Pipe Modifications

Figure 70: *Exhaust Tubing and Perforated Muffler Tube*

In order to increase the length of exhaust headers, tubing was acquired and welded to the 39 inch length simulated. This calculation is the optimal length for a pressure wave to travel through tubing and reach valves consistently at a 6000 RPM speed. While the muffler is approximately 23 inches in length, this tubing is considered negligible, as perforations within this tubing cause a pressure wave to disperse and make the return back to exhaust valves.

Fuel system

Fuel Selection

As referenced in FSAE rule IC 5.2, vehicles must run on a choice between either gasoline or E85 fuel which would be available at competition. It was important for the project to make a decision on fuel early, as either choice would broadly affect the power, tuning, and reliability of the engine later on. In previous years, gasoline has been run due to its accessibility and instructed choice of operational fuel for most FSAE compliant engines. Nonetheless, E85's feasibility for the Yamaha WR450F had been evaluated for the sake of future teams understanding the benefits and drawbacks of the fuel.

E85, or Flex Fuel, possesses characteristics which can lead to higher horsepower and torque for the engine, yet many preparations would have to be made to ensure the engine is prepared to run on it without issue. Negative characteristics of the fuel are also its benefits, with the high oxygen content of ethanol (around 35 wt%), as well as the high latent heat of vaporization work well with higher compression ratios when compared to gasoline. At high RPMs, greater air-fuel charge flow takes place, increasing volumetric efficiency, while requiring higher fuel consumption in order to maintain stoichiometry. The fuel additionally has a high octane rating ranging from 100 to 105 based on research, which would work well high compression engines. One of the most concerning challenges with E85 however is the presence of acetic acid and water within the fuel. Acetic acid is corrosive to aluminum, which could prove detrimental to the operational lifespan of the aluminum block of a WR450F engine, as well as certain intake components such as the injector pipe in contact

with the fuel before reaching the combustion chamber. Additionally, certain rubber and silicone materials exposed to the fuel can become brittle and crack over time. The 2018 WR450F manual does state that running E10 fuel, a mix of standard gasoline, can be safely used, however this naming system explains inconsistencies found with ethanol dominant fuels. Flex Fuel in the U.S. can contain anywhere between 51%, to 83% ethanol, with no discernable way to discover what this ratio is during acquisition.[19] Cold starting the engine may prove to be a dilemma as well if winter testing were to take place, as the high latent heat of vaporization for the fuel can prevent combustion. The design precautions taken to ensure the engine can run on E10 are not stated in the manual, with the same issue for any engine coatings, specific gasket materials, among others. Heavy investigation and testing of engine components would be required to take place, potentially making the engine unusable in the process.

Due to uncertainties with ethanol based fuels, it was decided that gasoline would be the fuel run in the car, due to not only being the instructed fuel for the WR450F, but also the potential for high compression engine modifications to still be made without engine failure due to knowledge gained in previous years. The gasoline utilized during FSAE competitions is not 87 to 94 octane, but race gas with an octane rating of 100. This was the logical choice for the project, as the fuel has been run on WR450F engines of later years without issue of engine knock or backfire. Additionally, Haltech engine tunes used this year were derived from data gained from former years, which had also utilized the fuel. Gasoline with a 100 octane rating was chosen due to its lack of potential component fracture or decomposition when compared to E85, along with its general reliability and versatility when converting to higher performance parts.

The majority of the fuel system was carried over from the previous years vehicle. Since the frame design was similar to the 2018 vehicle the fuel tank could be retrofitted into the new chassis with minimal modifications. An improvement that was made to the fuel system was the addition of AN (Army Navy) fittings on the fuel lines. AN fittings are available in a selection of configurations which include different bends, end type, and hose connection type. Figure 71 shows a selection of different type of AN fittings. Although the addition of AN fittings will cost more than using a standard barb fitting with a hose clamp they provide a more secure and reliable connection, reducing the risk of any fuel leaks.

Figure 71: *Example of AN Fittings* [22]

Future Fuel System Recommendations

      A major problem with the current fuel system is the use of a Walbro 255LPH (Liter per hour) fuel pump. The reason this pump is used is because of its all metal construction and its inline configuration make it easy to use and meet the FSAE rule requirements, unlike a pump mounted inside the fuel tank. This fuel pump can support over 500HP and is excessive for this application. The current draw of this pump is large, between 6-9 Amps. This is fine for full size automobiles with large 100-150 Amp charging systems, but is hard on a small motorcycle engine charging system. The 2018 Yamaha WR450F engine includes a 160W stator to power all electrical components. The Walbro 255 drawing 9 Amps (108W at 12V) will use approximately 68% of the total stator output. It is recommended to future team to find a new fuel pump with a motorcycle specific pump to both reduce weight and electrical current consumption. The best method would be to use an in tank pump rather than an inline pump. Many motorcycles use returnless in tank fuel systems which locate the pump, pressure regulator, filter, and even a fuel level sensors in the tank; the complete assembly is commonly referred to as a fuel sending unit. Implementing a returnless system would only require one fuel hose to be routed from the sending unit to the injector and would eliminate the inline fuel pressure regulator currently being used, therefore reducing the weight of the vehicle. An example of a sending unit to consider is from a Suzuki RMZ450 motorcycle, seen in Figure 72. If other fuel types are to be considered, such as E85, a fuel sending unit of this type may need to be designed and manufactured by the team because any available 450cc motorcycle fuel pump might not be able to deliver the required amount of fuel. When designing the fuel system be sure to not only consider the fuel delivery, but also the electrical current consumption to reduce the demand on the electrical system.

Figure 72: *Suzuki RMZ450 Fuel Sending Unit* [23]

Another recommendation is for future teams to consider different fuel injectors. The current fuel injector was purchased from FiveO Motorsports and is a 550cc/min Black-Ops M-Series Injector. The size of the required injector can be determined using simple calculations. The flow rate of the injector is a function of the desired horsepower, the brake specific fuel consumption (B.S.F.C), the number of injectors, and the maximum injector duty cycle. B.S.F.C is the amount of fuel being used per horsepower per hour and can be assumed to be 0.5 for a naturally aspirated gasoline engine. Injector duty cycle is the time the injector stays on and should not exceed 80% for reliable operation. Assuming a horsepower goal of around 60 brake horsepower would result in the engine requiring a injector flow rate of approximately 37.5lbs/hr or 393.75cc/min.

$$\frac{(BHP * B.S.F.C)}{(\# \ of \ Cylinders * Inj \ Duty \ Cycle)}$$

$$\frac{(60 * 0.5)}{(1 * 0.8)} = 37.5lbs/hr = 393.75cc/min$$

It can be seen that the current 550cc/min injector is much larger than required. This larger injector was chosen in case E85 was to be selected. If gasoline is still to be used in the future years it would be recommended to decrease the injector size. Although the vehicle does operate fine with the 550cc/min injector a smaller injector could help improve idle and low speeds drivability due to a more precise fuel delivery.

Cooling System

Throughout the semester, the cooling system for the 2019 car has had changes that from calculations, maintain similar cooling performance in comparison to last year. The main focus was optimization of air flow through the radiator, and reducing the electrical demands of the radiator fan, which were both accomplished with the same solution. Last year's Auto Dynasty fan was a push configuration, pushing air through the radiator around the radius of said fan, yet obstructing and slowing air flow in the process. Air flow for the car when stationary only occurred through the area of the fan, as the lack of a shroud made air outside of this effective area stagnant. Additionally, the electrical demands of the 12.7 A fan were surpassed only by the fuel injection system, which in combination puts heavy demand on the stator of the car. It was clear that improvements could be made, and therefore a more efficient fan and cooling configuration was sought after to eliminate these issues.

The benchmark for radiator performance was acquired from test data at 2300 RPM and 7000 RPM of last year's MQP, being a heat dissipation of 17,200 W and 44,400 W respectively. The ambient temperature during this testing was 7°C. Utilizing this information along with the fact that the entire radiator surface area will be utilized in the new configuration, the minimum volumetric flow rate required for a fan to meet cooling demands can be confirmed to work at both low and high RPM.

$Q = \dot{m}c(T_2 - T_1)$ *All calculations done in SI Units.*
- $\dot{m}$ = mass flow rate (ambient air density (p) x air velocity into radiator (v) x core area (A))
- c = specific heat of air
- T_1, T_2 = ambient air temperature, radiator air temperature

Assumptions:
- Vehicle speed is 0 m/s, when fan performance is critical due to no airflow from travel.
- Radiator core area of the car's current configuration is the area of the 7" fan (0.025 m^2), as the current push configuration only allows for airflow within the bounds of the Auto Dynasty fan's diameter.
- Radiator core area of the new pull configuration utilizes the entire core area (0.063 m^2), as the addition of a shroud will allow for fan airflow through the entire radiator.

2300 RPM:

$c = 1005$ J/kg*°C at 7°C

$p = 1.259$ kg/m^3 at 7°C

$A_{fan} = 0.0250 m^2$

$v = 12.91$ m/s (Auto Dynasty CFM = 1730 cu ft/min. = 0.8165 m^3/s => 0.8165/A)

$17,200\ W = (1.259\ kg/m^3 * 12.91\ m/s * 0.025m^2)1005\ J/kg°C(T_2 - 7°C)$

$T_2 = 49.12°C$

With air temperature in the radiator calculated, the required air velocity for the new pull/shroud configuration can be found when utilizing the entire radiator area within the same conditions. This will then be used to find CFM for a new 7" fan.

$A_{radiator} = 0.0630 m^2$ (h*w = 0.2080*0.3040)

$17,200\ W = (1.259\ kg/m^3 * v * 0.0630m^2)1005\ J/kg°C(49.12°C - 7°C)$

$v = 5.12$ m/s

$A_{in}v_{in} = A_{out}v_{out}$

$0.0630m^2 * 5.12$ m/s $= 0.0250m^2 * v_{out}$

$v_{out} = 12.9$ m/s

Volumetric Flow Rate $= A_{out}v_{out} = 0.0250m^2 * 12.9$ m/s $= 0.3225 m^3$/s => 683.3 cu ft/min.

7000 RPM:

Fan activation temperature of 2017-18 car: $90.6°C$

$44,400\ W = (1.259\ kg/m^3 * 12.91\ m/s * 0.0250m^2)1005\ J/kg°C(T_2 - 7°C)$

$T_2 = 115.7°C$

$44,400\ W = (1.259\ kg/m^3 * v * 0.0630m^2)1005\ J/kg°C(90.6°C - 7°C)$

$v = 6.66$ m/s

$A_{in}v_{in} = A_{out}v_{out}$

$0.0630m^2 * 6.66$ m/s $= 0.0250m^2 * v_{out}$

$v_{out} = 16.8$ m/s

Max Volumetric Flow Rate $= A_{out}v_{out} = 0.0250m^2 * 16.8$ m/s $= 0.420 m^3$/s => 889.9 cu ft/min.

Figure 73: *UPGR8 Radiator Fan.*

With the volumetric flow rate found, focus was applied to finding a fan with lower amperage than the current Auto Dynasty meeting the volumetric flow rate threshold. This turned out to be the UPGR8 Universal 12V High Performance Radiator Fan (7") of 1350 CFM. While 6" and 8" fans rated at 900 CFM were considered, none had lower amperage than the fan chosen. The UPGR8 fan has an amperage of 6.6 A compared to Auto Dynasty's 12.7 A. It has the added benefit of being 0.3 lbs lighter than the current fan's weight of 2.1 lbs. As it turns out, the only difference between the old and new fan were UPGR8 radiator fan's curved blades. As of now, the current Mishimoto radiator will be implemented into the new car, with cooling system testing being done to validate these calculations once a test bench has been developed.

Ricardo WAVE Simulation

Ricardo WAVE is a one dimensional (1D) engine simulation software package utilizing computational flow dynamics to create an accurate computer model of a motor and its related powertrain components. The goal of the software's use is to implement the known dimensions and specifications of our 2018 Yamaha WR450F engine to prepare a virtual model which can be used to both experiment with and validate changes to motor components, as well as the new intake and exhaust system. Data was gathered through physical measurements and the 2018 WR450F manual, then placed in the corresponding engine elements for WAVE. Information required for the engine modelling process of Ricardo WAVE will be described, as well as how parameters were gathered and implemented.

Figure 74: *Ricardo WAVE 2018 WR450F Engine Model.*

Elements

Elements are the various objects within Ricardo WAVE software that are placed and attached to other elements to create an accurate representation of the engine desired. WAVE is known as 1D engine simulation due to the fact that these elements, no matter their complexity, all begin at one element, and follow a chain of attachments that will lead to a final element. Laying all elements side by side in a left to right order is a simplified explanation for how the software perceives the model, no matter the on screen representation. The leftward diagonal curve seen at the bottom left of Figure 41 is where the beginning of the model lies, yet its orientation has no effect on the parameters or data gathered during simulation. The order elements appear in can be described in likeness by the order gases make contact with a component, being intake, to engine, to exhaust in general terms. Within the multitude of elements seen is a list of parameters to be input by the user, in which material specifications, shape dimensions, operating temperatures, and more are to be implemented, with data requirements differing among element types. It is evident that data or measurements can sometimes be limited or unattainable due to lack of equipment or information, and therefore the system allows for some parameters to be assumed under default WAVE numbers, or can be withdrawn as a variable altogether. These assumptions will be reviewed element by element. Nonetheless, the end result is a linear system which utilizes the data and measurements given to create a simulation of the WR450F, which can have parameters adjusted to see how certain characteristics can affect the performance of the engine.

Ambients

One of the simplest elements in WAVE, ambients are typically the beginning and ends on an engine simulation, representing the intake and exhaust of a given engine. The state of the air as well as its composition can be input, being 300°K at an atmospheric pressure of 1 bar for the intake ambient, and values of 800°K at 1.05 bar for the exhaust ambient. The gas composition of ambients are given as simple ratios representing a ratio of burnt and unburnt air and fuel, yet without the means to measure gas composition for the car, these have been left as defaults.

Ducts

Representing a multitude of piping components found in all motors, ducts must be measured and given the proper parameters and approximations in order to be interpreted correctly within the software. Due to their varied use, the intricacy of parameters implemented into a duct vary throughout the system. The inner diameter, length, and the angle of the pipe bend are values taken into account for all ducts within the WR450F WAVE model, yet more advanced parameters such as the heat transfer and roughness values for duct materials, flange inertia, and more are applied in cases where they are known, being left as a default and/or non-existent parameters otherwise.

Simplicity can is primarily be found with certain intake ducts, being ducts to the left of the engine cylinder, as intake piping has not yet been constructed. Therefore, the further away one goes towards the left in the model, the simpler the duct parameters are, being altered in length and shape to understand potential adjustments to air flow and intake tuning that can be done. Other intake components that are already finished, such as the intake boot, have been measured with calipers and implemented into the model. After the second Y-junction in the system the most complex ducts lie, being the representation of intake and exhaust runners.
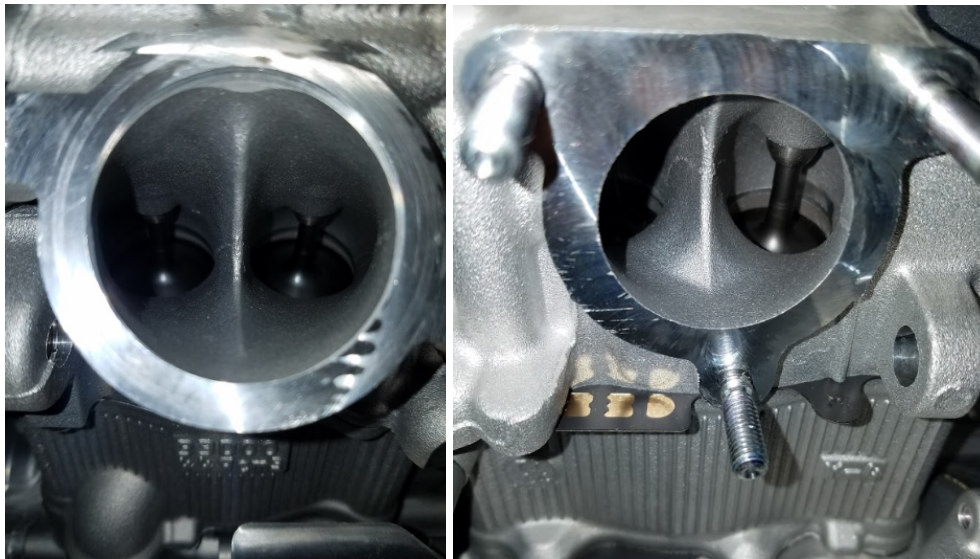
Figure 75:*WR450F Intake and Exhaust Runners*

Runners were the most difficult duct to input in WAVE, as there were many approximations that had to be made, as well as keeping track of how we wished to have the runners interpreted when involved with other elements such as valves and Y-junctions. One of the first interpretations decided upon was the runner length, which is approximated at 57 mm for intake and 43 mm for exhaust, starting at the deepest point of the spline and going to the center of the valve stem as seen in Figure 75. The main opening for intake and exhaust runners were measured as the flat machined face for the entrance of the ports, to the deepest part of the spline. The true curved shape of the runners are outside of the capabilities of our current Ricardo WAVE license, as Ricardo has 3D versions of most of their software, allowing intricately shaped virtual models of components to be made for more realistic airflow calculations.

Since our version of WAVE only accepts circular diameters, the complex elliptical shapes for the ports had to be approximated by height and width, with their areas then converted into a circular shape to give us the radius. This was done using the following formulas.

The equivalent diameter of a oval duct or tube can be seen in the following equations [4].

$$d_e = 1.55A^{0.625}/P^{0.25}$$

where,
A = cross-sectional area oval duct (m², in²)
P = perimeter oval duct (m, inches)
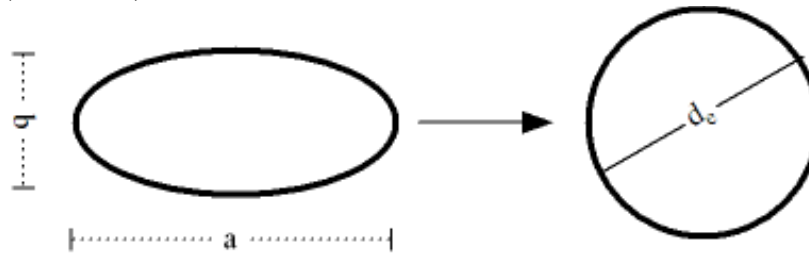
Figure 76: Equivalent diameter of tubing

The cross-sectional area of an oval duct can be expressed as
$$A = \pi\, a\, b\, /\, 4$$

where,
a = major dimension of the flat oval duct (m, in)
b = minor dimension of the flat oval duct (m, in)
The perimeter of an oval duct (ellipse) can be approximated to

$$P \approx 2\,\pi\,(1/2\,((a/2)2 + (b/2)2))1/2$$

Figure 77: *Port Geometry Measurements*

The end result of utilizing these formulas gave us an approximated shape which WAVE will perceive for the ports, being a curved cone shape. Looking in the simulation for the runner ducts however, there will not be a bend angle in the parameter. This is due to curves being accounted for in valve flow coefficients, as said in R-Desk Manual Chapter 3.1.1.
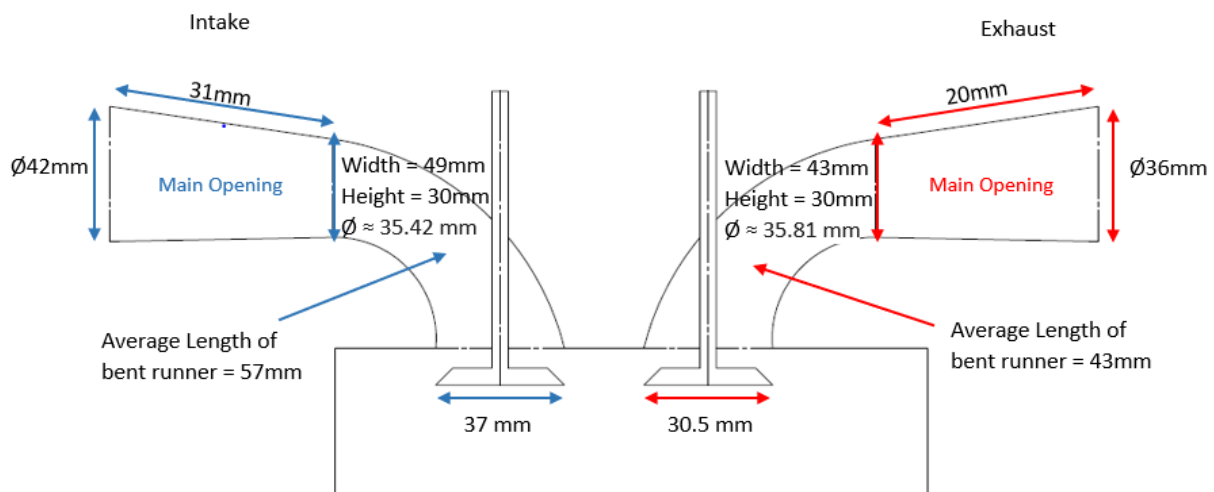
For exhaust and intake ducts, an optimal length and diameter are desired to take advantage of pressure waves the occur from Helmholtz Resonance. This resonance occurs due to the oscillation between combustion and exhaust strokes in a typical internal combustion engine. Air consumption and emissions ejection through intake and exhaust tubing respectively does not occur at a constant rate, as their valves close and open rapidly. During these events, the incoming air and outgoing exhaust gases create a pressurized area near these valves, then sending a sonic pressure wave back towards the atmospheric opening at the end of these ducts. These pressure waves can be accounted for in an internal combustion engine's operation. Known as resonance tuning, these pressure waves bounce back and forth from end to end of engine piping, and can increase horsepower and torque incrementally at a specific RPM. If said pressure waves arrive once an intake valve opens, additional air can enter the chamber, aiding the combustion process. If a pressure wave is leaving an exhaust valve once it opens, exhaust gases can be evacuated from the chamber much faster. If piping is to stay a constant length and diameter, as with the exhaust, the RPM for this desired tuning must be accounted for, as the speed of these pressure waves remains constant as a sonic wave as well. This has been done using the following calculations derived from A. Graham Bell's *Performance Tuning in Theory and Practice, Four Strokes* [5].

The value for ED is derived from our cam timing measurements implemented within Ricardo WAVE. The exhaust anchor in WAVE is 254° on one side of the lobe.

$P = (850(ED) / RPM) - 2.5$ P = Pipe Length (in.)
$P = (850(254) / 6000) - 2.5$ ED = Angle range in which exhaust valve is open.
$P = 33.5 \ in.$

$ID = (\sqrt{(cc / (P + 3)25)}) * 2.1$ ID = Inner Exhaust Pipe Diameter
$ID = (\sqrt{(449.3 / (33.5 + 2.5)25)}) * 2.1$ cc = Cylinder Volume (cm^3)
$ID = 1.5 \ in.$

The exhaust calculation for primary pipe length was initially subtracted by 3, which was eventually deduced to be an assumption made in Graham Bell's *Performance Tuning in Theory and Practice, Four-Strokes* [5] that the distance between the exhaust valve and beginning of the headers was around 3 inches. While we don't have a perfect value, this length has been approximated at 63 mm, or 2.5 inches, and was incorporated in the equation. The end result is an exhaust pipe a half-inch longer, and the same diameter as it would be if 3 was subtracted. The length and diameter for these components have been implemented into the simulation, yet with the measurements of Yamaha exhaust header piping purchased early in the year included in the model.

Figure 78: *Yamaha Exhaust Header Piping.*

The reason orifice elements exist within the WAVE model is due to the Yamaha exhaust header piping being two components of varying diameter. In addition, resonance tuning for the intake will be more complex, as we plan to develop variable intake runners for the engine.

Throttle

The throttle is an element used to model a butterfly plate within an orifice, which is implemented in the system to represent the butterfly valve within the intake system. Considering its function, there are not many functional characteristics to input, being basic measurements such as the diameter of the valve, the diameter of the shaft which the valve pivots upon, and the angle of the plate when resting which was estimated at 12 degrees. During a simulation run, the throttle will open when throttle is applied, which constantly at any and all RPMs as of now. Therefore, the throttle in WAVE is there as acknowledgement of material within a portion of the intake duct for the sake of making the air pressure waves and flow more representative of what will occur for the intake in reality.

Y-Junctions

Junction elements are a more complex version of ducts, as their variable shape requires more parameters to be accounted for. Within our engine model, Y-Junctions are a representation of the main opening for intake and exhaust ports. While this would imply these Y-Junctions could be perceived as simple tubes, the WAVE model perceives them as a large cylinder with a width equal to that of the intake diameter, with two small exists being equivalent to the approximated diameters of the beginning of port runners.

Figure 79: *Port Volume Measurement*

Thankfully, developers of the software have acknowledged the complex shapes of most ports, and allow an input for volume to be taken into account. This will be the primary value used to determine mass transfer of air flow in the software, not the diameters of the Y-Junction. The measurements were done utilizing a burette which dispensed fluid into the required orifices until full, giving us a total intake and exhaust valve chamber volume of 100 mL, and 56 mL respectively. Before this was done, our Y-Junctions were set at default values to simply acknowledge the presence of a split into two runners for intake and exhaust ports. Once these volumes were implemented, as well as more accurate valve diameters, a significant increase of about 5 horsepower was noticed, bringing the max value for the simulation up to 50 hp.

Injector

The fuel injector element in WAVE allows for various ways to interpret how much fuel enters the engine and at what rate. For now, our injector is based on the Fuel/Air Total injector, as its basic parameters only factors in the ratio of fuel to air. This has been left as a default, which utilizes the stoichiometric ratio between air and gasoline as an input. More specific details will be implemented once more is known about the fuel injector selected for the car.

Valves

One of the most important inputs for the engine simulation was the camshaft profiles or the geometry of the camshaft lobes. A significant amount of the data needed for the simulation can be found in the Yamaha service manual, but only a small amount of the needed data was listed in the manual. The two main measurements needed were the camshaft lobe lift and the camshaft duration. The camshaft lobe lift is the distance the cam moves the tappet and opens the valve. The duration is the measurement of the time one valve begins to open until it finishes closing. The initial measurements were done by installing a degree wheel onto the engine crankshaft and recording the maximum angle the crankshaft turns from the start of the cam lobe to the cam lobes maximum lift. The lift of the camshaft was measured using a dial indicator positioned on the camshaft lobe, see Figure 80.
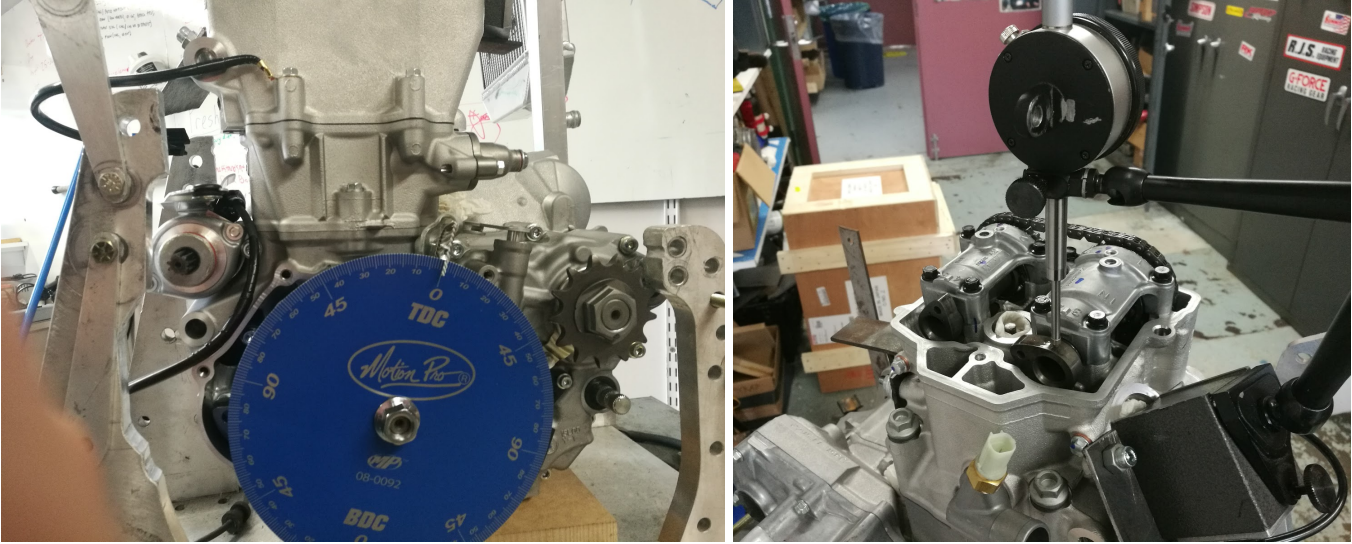
Figure 80: *Camshaft Lift and Duration Measurement with Degree Wheel and Dial Indicator.*

An issue was discovered with this data that was causing the simulation to produce negative power, not ideal. The cause was due to how the program was reading the cam profile data.With a multitude of changes compared to the original Ricardo motorcycle engine example model we began from, we were able to isolate the cause of the issue by implementing the original intake/exhaust measurements and cam timing from the example motorcycle engine until positive power could be produced. The cause of the issue was found to be that only 20 data points were recorded for the new WR450 exhaust cam profile and 18 for the intake, this was not enough. Feeling unconfident in the accuracy of the camshaft profiles we obtained from measuring the camshafts while in the engine the team decided it would be best to take the time to measure the cams using the CNC milling machine. The camshafts were removed from the engine and mounted to the rotary indexer in the VM2 milling machine. This allowed the cam to be rotated an exact amount and then record the lift of the lobe using a dial indicator, see Figure 81. This data was plotted into an excel table to convert the units of the the measured lift (inch to millimeters) and also convert the camshaft degree values into crankshaft degrees (since the crankshaft rotates twice per cam rotation). This conversion was needed to input the data into the Ricardo Wave simulation. This method allowed for many more data points to be collected and was input input into an excel sheet to create a lift vs crankshaft degree plot for the intake and exhaust cam, see Figure 82.

Figure 81: *Camshaft Lift and Duration Measurement with CNC Mill and Dial Indicator.*
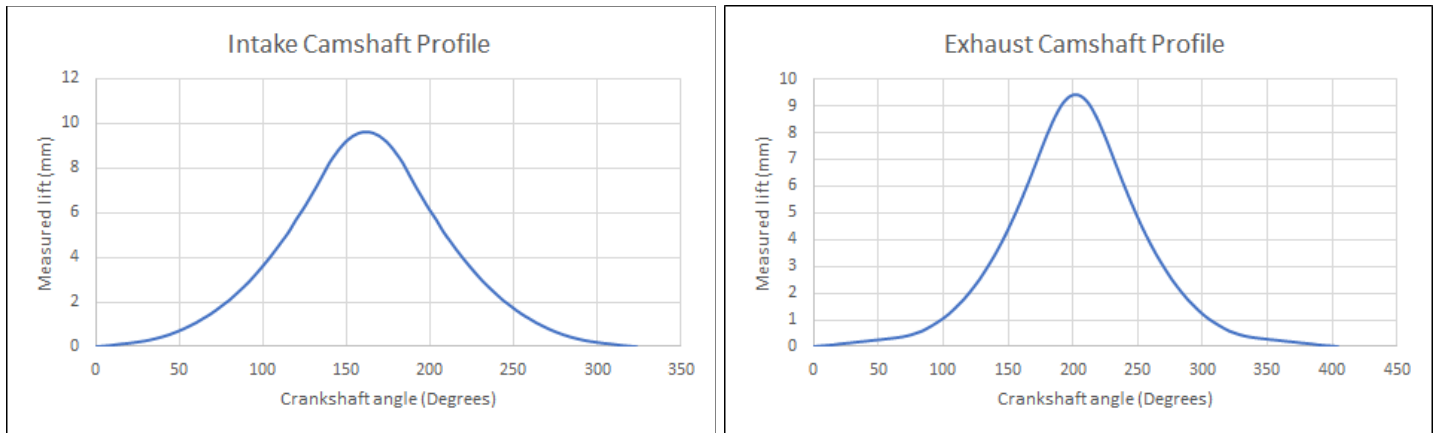
Figure 82: *Camshaft Lift vs Crankshaft Angle for Intake and Exhaust Camshafts.*

Engine Cylinder

The cylinder element is modelled after physical measurements taken for the WR450F during dismantling. The cylinder is an element in WAVE that doesn't require every element to be filled with data, yet the more that is contributed, the more accurate engine performance is expected to be. The bore and stroke of the WR450F were implemented from measurements gained from the manual. Other parameters such as wrist pin offset had to be physically measured, such as the wrist pin offset of 0.1 mm on the new 14:1 compression ratio Wiseco piston. Unknown variables left as defaults in the engine cylinder element include temperatures of the cylinder liner, cylinder head, piston top, and valves. Other parameters, such as the head geometry and pentroof height, require 3D modelling, which we do not have access to. Besides the aluminum block and titanium valves, much is not known about engine materials. The coating for cylinder liners is required by WAVE, yet the manual and online sources do not reference the existence of a cylinder liner for the WR450F whatsoever. This and more will have to be investigated further, yet have been left with generic assumptions in the model, such as the cylinder liner being the same material as the rest of the block.

Engine Block

The engine block element does not play a serious role in simulation, as the WR450F is a single cylinder engine. Most parameters for the block can be found within the cylinders, with the engine block primarily accounting for the number of pistons with those parameters.

Orifice

Ducts of varying diameters must still remain interconnected, such as with the exhaust system. Physically, this is explained with tight fittings, such as with the FMF muffler, yet with WAVE this is represented by an orifice element. An orifice element is a dimensionless element placed between two ducts, or pipes. Ducts of varying diameters are bonded together through this element, and will act as a virtual representation of differently sized ducts sealed together. Previously, ducts have contained their physically measured diameter on the left end ,and the physically measured diameter of the next duct at the right. Unless both ducts were the same, this would cause WAVE to perceive slightly cone shaped tubing, which isn't an accurate representation of real exhaust piping. Orifices solve this issue.

Work with Ricardo WAVE has proven promising, and most parameters required for an accurate simulation of WAVE have been collected. With the construction of a rolling chassis incoming, more data will be able to be implemented into the engine model, further acting as a proper representation of its realistic counterpart. From there, the focus of Ricardo WAVE will be an experimental one, adjusting and changing the components of the powertrain. Various adjustments such as exhaust and intake lengths will be simulated and reviewed, with the most optimal configuration being chosen and manufactured for the 2019 car.

Engine ECU Tuning and Electric Throttle Control

The WPI FSAE teams have utilized a Haltech standalone engine control unit (ECU) for several years with great success. For the 2019 competition vehicle a Haltech Elite 1500 was used because of its ability to control the drive by wire (DBW) system along with giving full control of fuel and ignition timing. Installing a standalone ECU onto single cylinder engines is not common and little information regarding tuning of a single cylinder engine is available, unlike multiple cylinder automobile engines. This section will help to explain the process taken to develop an efficient and reliable tune for the 2019 competition vehicle. The wiring harness and sensors used were taken from the previous years vehicle and modified to work on the new vehicle. The 2018 ECE MQP report [*2018 Formula SAE Race Car Electrical System*] contains the referenced material used to manufacture, install, and wire the components and sensors in the fuel injection system. The information in this section will mostly regard tuning the Haltech ECU, but all the principles should also apply to other ECUs.

Initial ECU Setup

The engine control unit is essentially a device that receives several inputs from various sensors and then sends outputs to several actuators to control the engine. All the sensor data is read and then interpreted using a lookup table or "map" and the information collected from the table is used to adjust the engine actuators. The main outputs of the ECU are the fuel delivery into the engine and the ignition timing to control when the spark initiates. Since DBW throttle control is used, the ECU also is in control of opening the throttle, therefore controlling the amount of air entering the engine. The tables stored in the ECU, such as the fuel or ignition maps, are constructed with two or three dimensional tables. Each axis will be a selected engine parameter such as engine RPM or engine load, and the current location on each axis is found from the data being measured by the various engine sensors. For example, Figure 83 displays a basic ignition map from a Haltech base tune. In this map, the X axis contains the engine load, which can be thought of as the amount of air entering the engine. The Y axis is the rotational speed of the engine in RPM. In the case of the 2019 competition car, the ECU measures the engine RPM and calculates the engine load using the intake manifold pressure from the manifold pressure sensor (MAP Sensor). Looking at the ignition map in Figure 83 shows how the ECU controls the firing of the spark plug. As the engine is running, the ECU will read the engine RPM and MAP sensor value then locate and command the spark plug to fire at the given degree value. The most difficult part in engine tuning is finding the correct values to produce the maximum torque and power output. Before creating any of the lookup tables, the ECU will need to be given information regarding the engine. Basic engine parameters such as displacement, number of cylinders, fuel type, and load type will need to input. Next would be to choose the injection and ignition mode.

Base Ignition Angle °										
Ignition - Load psi / inHg										
RPM	-29.5	-23.6	-20.7	-17.7	-14.8	-11.8	-8.9	-5.9	-3.0	0.0
10000	34.0	41.0	40.4	37.8	35.0	32.2	28.9	27.4	26.9	26.4
9000	34.0	41.0	40.4	37.8	35.0	32.2	28.9	27.4	26.9	26.4
8000	34.0	41.0	40.4	37.8	35.0	32.2	28.9	27.4	26.9	26.4
7500	34.0	41.0	40.4	37.8	35.0	32.2	28.9	27.4	26.9	26.4
7000	34.0	41.0	40.4	37.8	34.9	32.0	28.7	27.2	26.7	26.2
6500	34.0	41.0	40.4	37.8	34.8	31.8	28.5	27.0	26.5	26.0
6000	34.0	41.0	40.4	37.8	35.0	32.2	28.6	26.9	26.4	25.9
5500	34.0	41.0	40.4	37.8	35.0	32.2	28.4	26.4	25.9	25.4
5000	34.0	41.0	40.4	37.8	35.0	32.2	28.1	25.9	25.4	24.9
4500	33.2	40.2	39.6	37.0	34.2	31.4	27.5	25.4	24.9	24.4
4000	32.4	40.4	39.3	36.2	32.9	29.6	25.8	23.9	23.4	22.9
3500	31.8	40.8	39.2	35.6	31.7	27.8	24.5	23.0	22.5	22.0
3000	31.0	40.0	38.5	35.1	30.5	26.0	22.3	21.2	20.7	20.2
2500	27.2	34.2	35.3	32.5	29.0	24.6	20.9	19.8	19.5	19.0
2000	23.2	31.2	33.1	32.0	28.0	23.0	21.1	19.0	18.5	18.0
1500	17.4	22.0	26.0	26.0	22.8	19.6	17.5	15.2	14.7	13.2
1000	10.0	10.0	15.5	18.0	17.0	13.0	11.0	8.0	7.5	7.0
500	10.0	10.0	10.0	10.0	10.0	10.0	8.0	6.0	5.0	4.0
0	10.0	10.0	9.5	9.0	7.0	5.0	3.0	1.0	1.0	1.0

Figure 83. Modified Haltech Base Tune Ignition Timing Map

There are several injection modes, but the most common would be sequential and semi-sequential types. In sequential injection, the injection is timed to fire only on the intake stroke (once per engine cycle or every 720° of crankshaft rotation). Sequential injection requires full engine synchronisation which means that the ECU knows the position in the cycle at all times. The cycle position is measured using a trigger wheel on the crankshaft and camshaft. A common trigger wheel normally has an even number of teeth, but one of the teeth will be missing. The ECU will know that a full revolution has occurred by reading when the sensor misses a signal, which occurs when the missing tooth passes by the sensor. As the crankshaft position sensor counts the teeth on the crank trigger wheel it will be able to locate every 360° of crank rotation and also when the piston is at top dead center (TDC) . However, because the four stroke cycle is completed every 720° the piston is at TDC two times per cycle, once for intake/exhaust stroke and once for compression/power stroke. Sequential injection only fires the injector on the intake stroke and the ECU needs to know which of the two TDCs is the intake stroke. To accomplish this, a "home signal" is required. A home signal is normally given to the ECU by a camshaft position sensor. The trigger wheel on the camshafts will be able to signal the ECU on the intake stroke to let it know that the full cycle is complete and to inject more fuel. Semi-sequential injection mode is used in engines with no homing signal, such as our FSAE car. Since the ECU has no way to know when the piston is at the intake stroke TDC it will inject half the total amount of fuel on each of the TDC events. On the compression/power TDC the intake valve will be closed and the fuel will sit in the intake port until the next TDC where it will combine with the second half of the fuel being injected. Semi-sequential injection mode is considered to be less efficient than a full sequential injection mode because the fuel that sits in the intake port has the possibility to condensate on the port walls producing a less atomized fuel charge.

The most common ignition modes are direct fire and wasted spark. These two modes are very similar to sequential and semi-sequential ignition modes. Direct fire is comparable to sequential injection and wasted spark is comparable to semi-sequential. As with the injection modes because the current 2018 WR450F engine has only a crank position sensor there is no way for the ECU to know when the engine is approaching the

compression stroke to fire the coil. This means the ECU will fire the coil twice per engine cycle, just like the injection.

For future reference the 2018 Yamaha WR450F engine uses a variable reluctor crank sensor with a 12-1 trigger wheel. The 12-1 refers to a 12 tooth wheel with 1 tooth missing. The missing tooth is located 190° from TDC. Trigger wheel is located on the engine flywheel behind stator cover, seen in Figure 84.
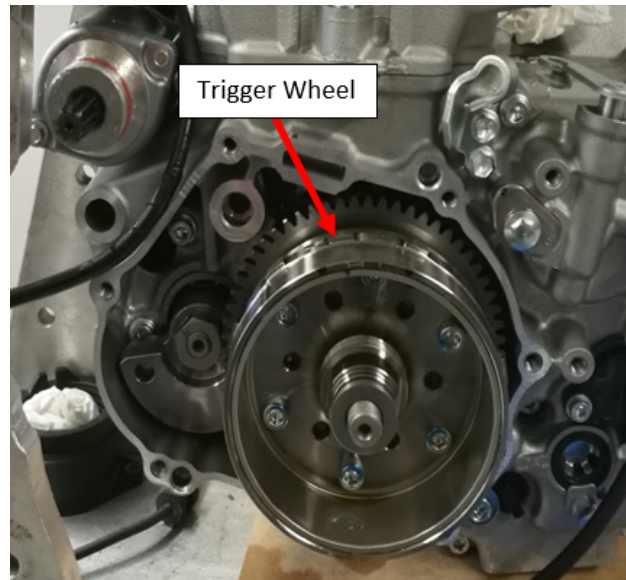

Figure 84: *Crankshaft Trigger Wheel Located on Flywheel*

Tuning Method

Before beginning fuel tuning, the tuning method needs to be chosen. Tuning method refers to the method the ECU uses to calculate the amount of fuel injected and defines the configuration of the fuel lookup tables. Three common methods are: mass air flow, injector pulse width (Injector time), and volumetric efficiency (V.E.). Mass air flow uses a mass air flow sensor to measure the air entering the engine and calculated the amount of fuel required based on the measure airflow. Injection time method calculates the fuel amount by opening the injector for a certain amount of time. The longer the injector is open, the more fuel will be injected and the richer the air fuel mixture will be. Lastly, the volumetric efficiency tuning method, or speed density tuning, is based on how much air can get into the engine cylinder. In other words, how full the engine's cylinder is. Volumetric efficiency can be defined as the ratio of air volume entering the cylinder and the volume of the engine's cylinder. [24] The air entering the engine needs to flows through and around the intake, throttle body, and valve components, which all act as a restriction to the air flow. V.E. (η_v) is calculated as the measured volume of air entering the cylinder (V_a) divided by the cylinders displaced or swept volume (V_d).

$$\eta_v = \frac{V_a}{V_d}$$

Volumetric efficiency relates to the volume of air fuel mixture entering the engine's cylinder and the volume of the cylinder itself, therefore V.E. is a function of the engine displacement, engine load, air

76

temperature, and the fuel injector characteristics [25]. The chosen tuning method for the 2019 competition car was volumetric efficiency. Since V.E is a function of the engines load, a MAP sensor was used to calculate the engine load by measuring intake manifold pressure.

Fuel Map Tuning

When using the V.E. tuning method, it is extremely important to make sure the correct engine specifications, injector flow rate table, and injector deadtime table are input into the ECU. Without the correct engine and fuel injector specifications the ECU will not be able to calculate the correct amount of fuel to input. Injector specifications, such as flow rate or dead times, are measured by testing the actual injector. Injector manufactures normally perform these tests and include the measured data with the purchased injector. Note that even two of the same model injector can have different flow and deadtime values so it is important to use the actual measured values. A wideband oxygen sensor is required to tune the fuel system. The wideband is wired into the ECU to input the actual air fuel ratio of the engine.

Fueling adjustment will be split into two seperate lookup tables. The first table is the target air fuel ratio (AFR) table and the second is the V.E. table, called the base fuel table. The AFR table is what the engine's target air fuel ratio is to be achieved. This table is constructed using the appropriate AFR for any certain RPM and engine load. At idle and light load conditions, engines require close to stoichiometric mixtures (14.7:1 AFR with gasoline). During high load conditions, a much richer AFR is required. A relatively rich AFR of 12.5:1 was initially chosen as a safe starting point for the current WR450F engine, which is utilizing a 14:1 high compression piston. After tuning the vehicle it was found that a 12.5:1 AFR was a slightly too rich and took away power across the RPM range. A final AFR of 12.7:1 was chosen due to it increasing power while still providing enough fueling to keep the combustion temperature down, keeping the engine safe. Figure 85 shows the target AFR table from the Haltech ECU tune.

Target Lambda Table Output | AFR

Fuel - Load psi / inHg

RPM	-29.5	-26.6	-23.6	-20.7	-17.7	-14.8	-11.8	-8.9	-5.9	-3.0	0.0	1.0
11100	14.5	14.3	14.0	13.8	13.5	13.2	12.9	12.6	12.7	12.7	12.7	12.7
10500	14.5	14.3	14.0	13.8	13.6	13.3	12.9	12.6	12.7	12.7	12.7	12.7
10000	14.5	14.3	14.0	13.8	13.6	13.3	13.0	12.7	12.7	12.7	12.7	12.7
9500	14.5	14.3	14.1	13.9	13.6	13.3	13.0	12.7	12.7	12.7	12.7	12.7
9000	14.5	14.3	14.1	13.9	13.7	13.4	13.0	12.7	12.7	12.7	12.7	12.7
8500	14.5	14.3	14.1	13.9	13.7	13.4	13.1	12.8	12.7	12.7	12.7	12.7
8000	14.5	14.4	14.2	14.0	13.8	13.5	13.1	12.8	12.7	12.7	12.7	12.7
7000	14.6	14.4	14.3	14.2	14.1	13.5	13.2	12.9	12.7	12.7	12.7	12.7
6000	14.6	14.5	14.4	14.4	14.3	13.6	13.3	12.9	12.7	12.7	12.7	12.7
5000	14.7	14.6	14.6	14.5	14.5	13.7	13.3	13.0	12.7	12.7	12.7	12.7
4500	14.7	14.7	14.6	14.6	14.6	13.7	13.4	13.0	12.7	12.7	12.7	12.7
4000	14.7	14.7	14.7	14.7	14.7	13.8	13.4	13.0	12.7	12.7	12.7	12.7
3500	14.7	14.7	14.7	14.7	14.7	13.8	13.4	13.1	12.7	12.7	12.7	12.7
3000	14.7	14.7	14.7	14.7	14.7	13.9	13.5	13.1	12.7	12.7	12.7	12.7
2500	14.7	14.7	14.7	14.7	14.7	13.9	13.5	13.1	12.7	12.7	12.7	12.7
2000	14.7	14.7	14.7	14.7	14.7	13.9	13.5	13.2	12.7	12.7	12.7	12.7
1500	14.7	14.7	14.7	14.7	14.7	14.0	13.6	13.2	12.7	12.7	12.7	12.7
1000	14.7	14.7	14.7	14.7	14.7	14.0	13.6	13.2	12.7	12.7	12.7	12.7
500	14.7	14.7	14.7	14.7	14.7	14.1	13.7	13.3	12.7	12.7	12.7	12.7
0	14.7	14.7	14.7	14.7	14.7	14.1	13.7	13.3	12.7	12.7	12.7	12.7

Figure 85: Haltech Target AFR Table

After the target AFR table is made, each cell of the V.E. table needs to be adjusted. Be sure that all correction maps, such as coolant temp and air temp maps, are turned off so only the V.E. table can affect the engines AFR. Beginning at idle and low load conditions, the value in each V.E. cell needs to be adjusted until the actual air fuel ratio matches the target value in the AFR table. The values inside the V.E. table cells are percentage values of the air entering the engine's cylinder. Around 40-50% V.E. is a typical value under idle conditions. The higher the value in the cell means more air is entering the engine, therefore the ECU will command more fuel to be to be injected. Continue adjusting the values inside the V.E. table at different load and RPM locations until the actual AFR matches the target AFR ratio. To get into the higher load zones the vehicle can be ran on a dynamometer under constant speed mode. Under constant speed mode the vehicle wheel speed will not be able to exceed a selected speed and only the engine load will increase when more throttle is applied. Begin by selecting a wheel speed to bring the engine into a certain RPM row and then adjust the value inside the cell under each load cell as the load is increased. This can be repeated for each RPM row, but it is also possible to skip a couple rows and then calculate the values for thoses rows by interpolating between adjusted row above and below the unadjusted rows. When the engine RPM is the higher rev zones it may be more beneficial to switch to full dyno pulls (running the gar through a full gear while recording engine data) rather than a constant speed mode. Tuning the V.E. table is complete when the actual AFR curve across the entire RPM and load range, measured by the wideband oxygen sensor, matches the target AFR curve. The base fuel or V.E. table can be seen in figure 86.

Figure 86:. Initial Haltech Base Fuel (V.E.) Table

Ignition Map Tuning

After the fuel maps are completely tuned, the ignition advance angle map can be adjusted. Adding too much ignition advance with too lean of air fuel ratio can cause damage to the engine from pre-ignition or knock. Start the map by adjusting the advance at idle conditions. It was found that the WR450F engine had the most stable idle with between 13-16 degrees of timing advance. Ignition timing can also be a good way to help steady the RPM at idle. As previously mentioned, engine torque is increased by advancing ignition timing, which is achieved by increasing the amount of the combustion energy transferred to the piston. For example, if the target idle speed is 2000 RPM, the ignition advance under 2000RPM could be set to a higher value and the advance above 2000 RPM could be set to a lower value. What this would achieve is when the idle RPM drops below the target the higher advance would produce more engine torque and help to increase the engine speed, potentially preventing stalling. If the idle goes above the target, the lower advance would reduce engine torque and bring the RPM down, closer to the target value. An example of this can be seen in the zero demand ignition map shown in figure 87.

Zero Demand Ignition Angle °									
RPM RPM									
	600	**1100**	**1200**	**1300**	**1500**	**1750**	**2000**	**2500**	**3000**
CTS °F 210	30.0	30.0	25.0	23.0	19.0	18.0	13.0	13.0	10.0
180	30.0	30.0	25.0	23.0	19.0	18.0	13.0	13.0	10.0
140	30.0	30.0	25.0	23.0	19.0	18.0	13.0	13.0	10.0

Figure 87: Initial Haltech Zero Demand Ignition Table

After adjusting the ignition advance angle for idle, the advance can be found under engine loading conditions using a similar method to the fuel tuning. However, instead of monitoring the engines actual AFR, the engine torque can be monitored on the dyno. In each load and RPM cell, the ignition advance should be adjusted for maximum torque. It is common that as load increases, the ignition advance angle will decrease, and when the engine speed increase the ignition advance angle will increase. When approaching the higher speed and load cells it is important to increase the ignition advance for max torque, but to be sure that the minimal value is used to decrease the risk of any detonation. A maximum ignition advance angle around 27.5° was found to produce maximum torque on the WR450F engine with the 14:1 wiseco piston. The Haltech ignition advance table can be seen in Figure 88.

Base Ignition Angle °											

Ignition - Load psi / inHg

RPM	-29.5	-23.6	-20.7	-17.7	-14.8	-11.8	-8.9	-5.9	-3.0	0.0	1.5
10000	35.0	35.0	35.0	33.1	31.2	29.4	27.5	27.5	27.5	27.5	27.5
9000	35.0	35.0	35.0	33.1	31.2	29.4	27.5	27.5	27.5	27.5	27.5
8000	35.0	35.0	35.0	33.0	31.1	29.2	27.2	27.2	27.2	27.2	27.2
7500	35.0	35.0	35.0	33.0	31.1	29.2	27.2	27.2	27.2	27.2	27.2
7000	35.0	35.0	35.0	33.0	31.1	29.2	27.2	27.2	27.2	27.1	27.0
6500	35.0	35.0	35.0	33.0	31.1	29.2	27.2	27.2	27.2	27.2	27.2
6000	35.0	35.0	35.0	32.8	30.7	28.6	26.4	26.4	26.4	26.4	26.4
5500	35.0	35.0	35.0	32.8	30.7	28.6	26.4	26.4	26.4	26.4	26.4
5000	31.7	31.7	33.0	31.2	29.4	27.8	26.0	25.6	25.7	25.7	25.7
4500	28.3	28.3	31.0	29.5	28.1	27.1	27.0	25.2	25.3	25.3	25.4
4000	25.0	25.0	29.0	27.9	26.8	26.3	27.0	25.0	25.5	25.0	24.5
3500	21.7	21.7	27.1	26.3	25.6	25.5	27.0	24.6	25.0	24.4	23.8
3000	18.3	18.3	25.1	24.6	24.3	24.8	27.0	24.0	24.5	23.8	23.0
2500	15.0	15.0	23.1	23.0	23.0	24.0	23.6	22.2	21.8	21.4	21.0
2000	15.0	15.0	19.0	19.0	19.0	23.6	23.1	21.6	21.0	20.5	20.0
1500	15.0	15.0	15.0	15.0	15.0	21.2	20.6	19.9	19.3	18.6	18.0
1000	16.0	16.0	16.0	16.0	16.0	19.8	19.0	18.3	17.5	16.8	16.0
500	16.0	16.0	16.0	16.0	16.0	18.4	17.5	16.6	15.8	14.9	14.0
Output Value 0	17.0	17.0	17.0	17.0	17.0	13.0	12.0	11.0	10.0	9.0	8.0

Figure 88: Initial Haltech Ignition Table

Drive by wire system

A drive by wire (DBW) system is a method of throttle actuation where the throttle body is actuated by an electric motor rather than a mechanical system, such as a cable or linkage. Due to the lack of physical connection between the throttle pedal and the throttle body a number of rules are employed by the FSAE organization to ensure the system cannot malfunction, causing the throttle to remain open.

General overview

For the 2019 competition our team will be running a similar system to the 2018 completion car. The main components of the system are a Bosch 40mm throttle body with dual throttle position sensors (TPS), a BMW accelerator pedal with dual accelerator pedal position sensors (APPS) and return springs, two Honeywell 3000 PSI pressure sensors for front and rear brake pressure measurement and a Haltech Elite 1500 ECU with ETC control. The Haltech ECU is used to compare the TPS, APP and brake pressure values. This ECU has two throttle position inputs and two accelerator pedal position inputs. The Haltech Elite ECU has several checks for fault conditions and in the event of a failure in the system the output to the DBW motor is cut. This would return the throttle to the closed position. Our system also includes a Brake Plausibility Device (BSPD) used to compare the brake pressure values acquired through the pressure sensors to the APP values. This device contains a standalone analog circuit that compares the values from the sensors and if any implausibilities are detected a relay will be activated and will completely remove power from the engine management system as well as fuel pump and other engine controls in order to trigger engine shutdown. Immediately after the power is removed the throttle body will return to the closed position and will be held closed by the throttle bodies internal spring. The Brake Plausibility Device may only be reset by power cycling the Primary Master Switch.

Suspension

Overview

The role of a vehicle's suspension system is to keep the tires in contact with the road surface as much as possible. The vehicle's suspension system is what harnesses the power from the power unit and the grip from the tires and ultimately defines the vehicle's performance on the track [6]. For all road vehicles, driver comfort and vehicle responsiveness must be optimized for the vehicles main function. In order to adjust these values, suspension geometry must be designed accordingly, along with correct selection of spring and damper rates. Other factors, such as a vehicle's tires, road surface, sprung and unsprung weight, center of gravity, and ride height, will affect how the overall vehicles performs and must be accounted for when designing a suspension system.

For racing applications, driver comfort is not considered a main priority, and only to the extent of reducing fatigue while racing. Autotrack racing occurs on smooth tracks, and therefore a soft bump absorbing suspension system is not required. Aerodynamics also play a major role in the vehicle's suspension system, and throughout the vehicle's race the downward force produced by wings must never bottom-out the car.

Design Formulation

Characteristics for how the vehicle should respond under suspension related situations must be defined before any design can take place. Often designing suspension systems is a balancing act, where one parameter will directly affect another. Characteristics should be prioritized when planning a suspension system, such as ride frequency for front and rear, to help guide your design to accomplish your end goal of a high performing suspension system. Along with characteristic prioritization, assemblies within the vehicle should be designed in parallel with the suspension to allow for direct compatibility. Figure 89 and 90 show the difference between designing suspension in parallel with the frame and without.
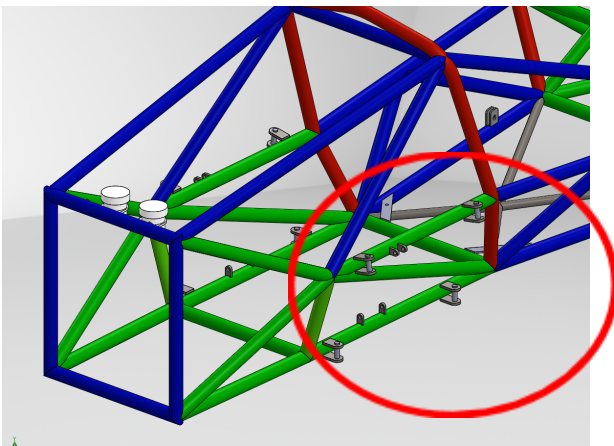

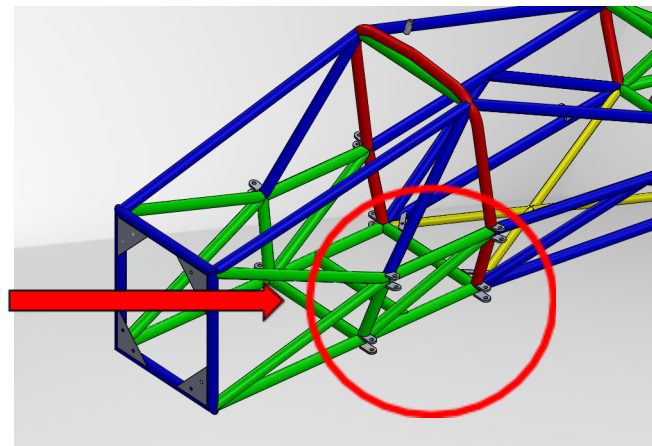Figure 89: *2018 car not designed in parallel.*   Figure 90: *2019 car designed in parallel.*

The past years car was not designed in parallel with their frame, which lead to a non ideal suspension mounting system. This current years frame was an optimization of last years frame to account for suspension, which will reduce tube twisting during engagement of the suspension system.

A key requirement for our suspension system is that the MkII shock absorbers have to be mounted vertically. This is a specification provided by the shock manufacturer, Ohlins. If mounted horizontally, there will be cavitation inside of the shock and will cause the shock to work unpredictably throughout run cycles.

Design Process

One of the initial issues the judges from the previous year had with our suspension design was the mounting points of our shocks and rockers. These mounting points created moments on frame tubes that were not designed to uphold these forces. Our team had two options to optimize the previous years design, one design which would horizontally mount the shocks, allowing for a rocker which would not generate a moment on the unsupported frame tubes (picture of rocker like that), or add more frame tubes to support the current design. Although the former sounds favorable, due to our TTX MKII shocks containing twin tube rods, the shocks must be vertically mounted to avoid cavitation [7]. Due to our frame being similar to the previous years, our team was able to utilize the 3 dimensional sketch created last year and adjust it for the new a-arm and rocker positions. After positions were selected, the car model would be imported into OptimumKinematics software to assist with upright mounting locations and rocker design.

Utilizing the data collected from last years car, tire data, and this years design preferences, a spreadsheet was developed to assist in the spring and damper rate selection utilizing equations from OptimumG, as seen in figures 91 and 92.

$$K_{ss} = 4\pi^2 f_s^2 m_{sm} MR_s^2$$

K_{ss} = Single wheel spring rate (N/m)
m_{sm} = Sprung mass on that corner (kg)
f_s = Single wheel bump frequency (Hz)
MR_s = Motion ratio (Wheel/Single wheel spring travel)

Figure 91: *Spring equation*[8]

$$\text{Initial Slope} = (4\pi \zeta_{ride} \omega_{ride} m_{sm}) \quad N/(m/s)$$

ζ_{ride} = Damping ratio in ride
ω_{ride} = Ride frequency (Hz)
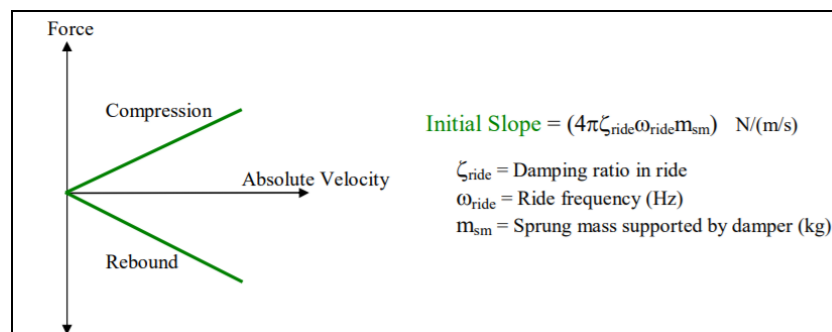m_{sm} = Sprung mass supported by damper (kg)

Figure 92: *Damper slope calculation*[8]

To simplify our modeling process, assumptions for the spring and dampers had to be made. These assumptions are defined in appendix D.

Using the information above, a half car model and Bond graph of the theoretical system was developed to analyze how these selections would affect the car. This model helps analyze the motions of a car through bump scenarios. An example of a half car model can be seen in Figure 93
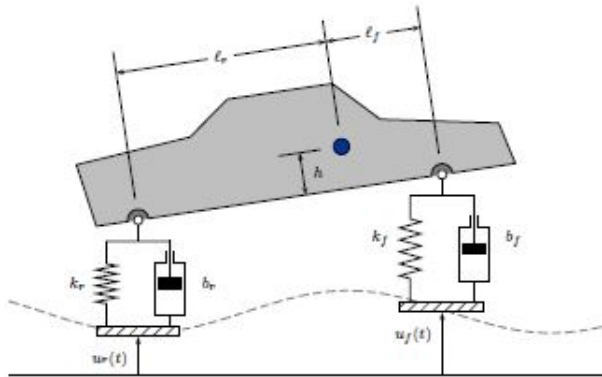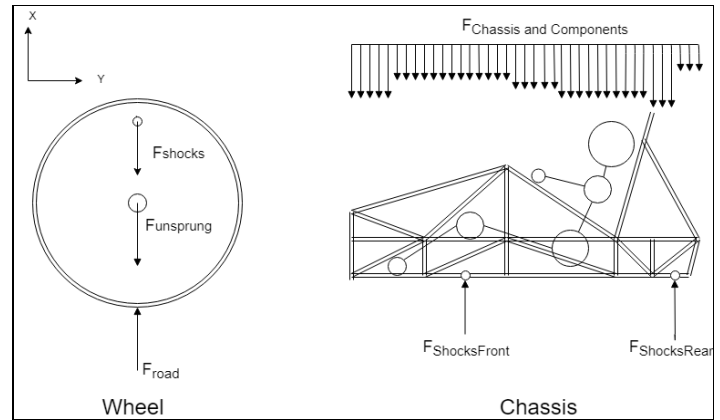

Figure 93: *Example of half car model [9]*

Figure 94: *Free body of single wheel and chassis.*

Figure 94 presents the free body diagrams representing a single wheel and our chassis with all components installed. This free body was necessary before forming our bond graph and state equations.

Once the free body was defined, the initial bond graph of the half car model can be formed, as seen in Figure 95. This graph shows the different components that make up our system.
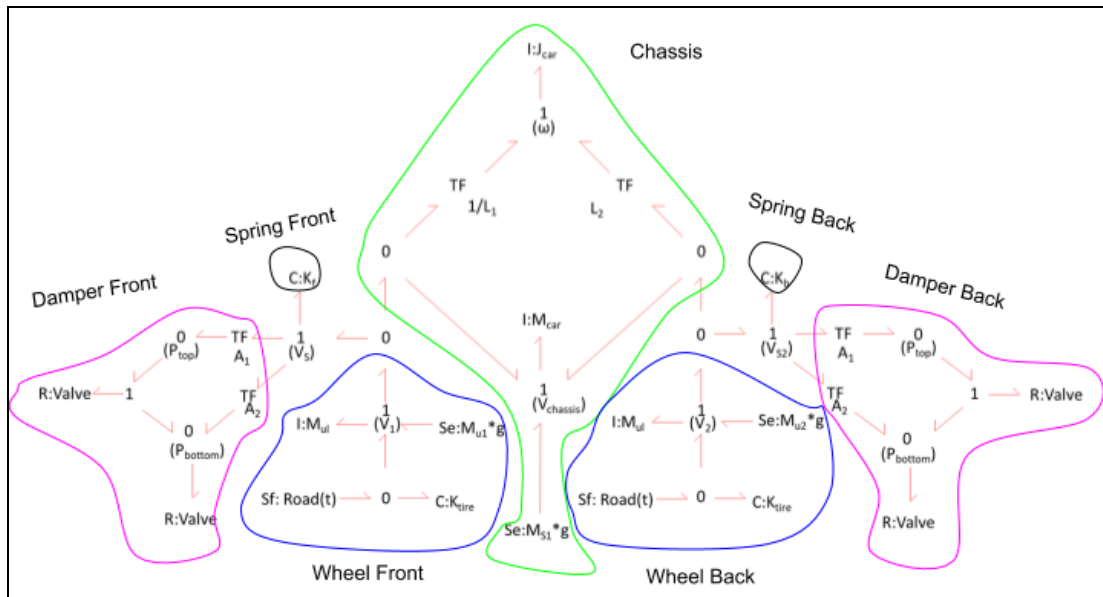
Figure 95: *Initial bond graph.*

Having information on the damper components already, our team was able to simplify the bond graph to the graph scene in Figure 96.
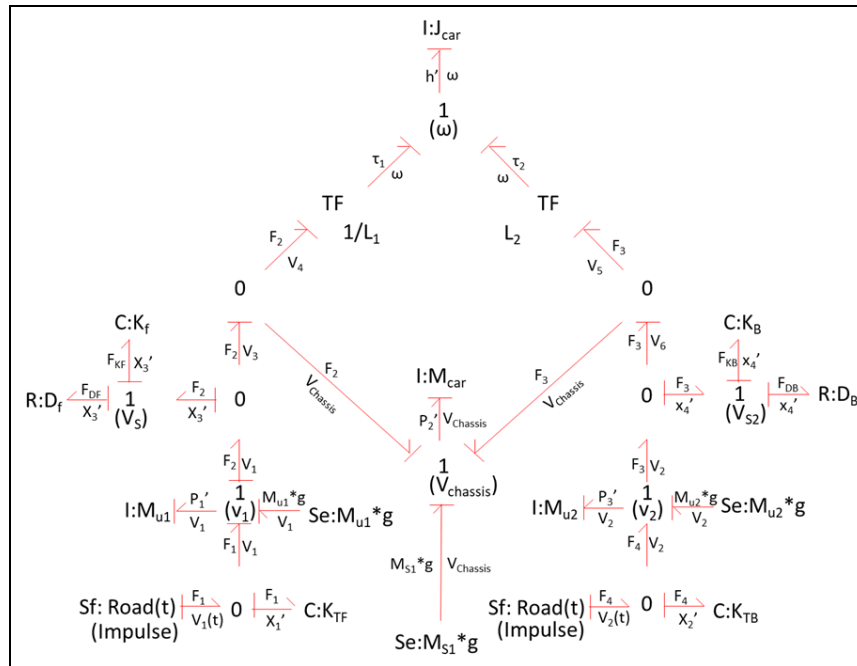
Figure 96: *Simplified bond graph.*

Below, Figure 97, are the equations our team was able to derive from the bond graph presented above. The state equation matrix and determining constants can be found in appendix D.

$$X_1' = V_1(t) - (P_1/M_{unsprung1})$$
$$X_2' = V_2(t) - (P_3/M_{unsprung2})$$
$$X_3' = (P_1/M_{unsprung1}) - (P_2/M_{sprung}) - L_1(h/J)$$
$$X_4' = (P_3/M_{unsprung2}) - (P_2/M_{sprung}) + L_2(h/J)$$
$$P_1' = K_{tf}X_1 + M_{unsprung1}G - (D_FP_1/M_{unsprung1}) + (D_FhL_1/J) + (D_FP_2/M_{sprung}) - K_FX_3$$
$$P_2' = (D_FP_1/M_{unsprung1}) + ((-D_FL_1 + D_BL_2)/J)h + ((-D_F - D_B)/M_{sprung})P_2 + K_FX_3 + M_{sprung}*G + K_BX_4 + (D_BP_3)/M_{unsprung2}$$
$$P_3' = K_{tb}X_2 + M_{unsprung2}G - (D_BP_3/M_{unsprung2}) + (D_BhL_2/J) + (D_BP_2/M_{sprung}) - K_BX_4$$
$$h' = (L_1D_FP_1/M_{unsprung1}) - h((L_1^2D_F + L_2^2D_B)/J) + L_1K_FX_3 - L_2K_BX_4 - (L_2D_BP_3/M_{unsprung2}) +$$
$$(-L_1D_F + L_2D_B)/M_{sprung}$$

Figure 97: *State equations.*

Utilizing Matlab, our team was able to convert our state equations into functions relating to time. To model a bump scenario, our team developed a piecewise function, seen in Figure 98, that would dynamically change the vertical velocity of the wheel when traveling over the bump and then to a constant vertical velocity

of 0 to represent the post bump continuation that would help us analyze the effects of the bump on our car. Our team currently does not have any bump data, so we estimated that the car traveling at ~9 m/s would take about .05 seconds to travel over the a small bump. The plotted response can be seen in Figure 99.

```
function V1= velocityFront(t)
if t<.05
    V1 = (8.9408)*sin(t*((2*pi())/.05));
else
    V1 = 0;
end
```
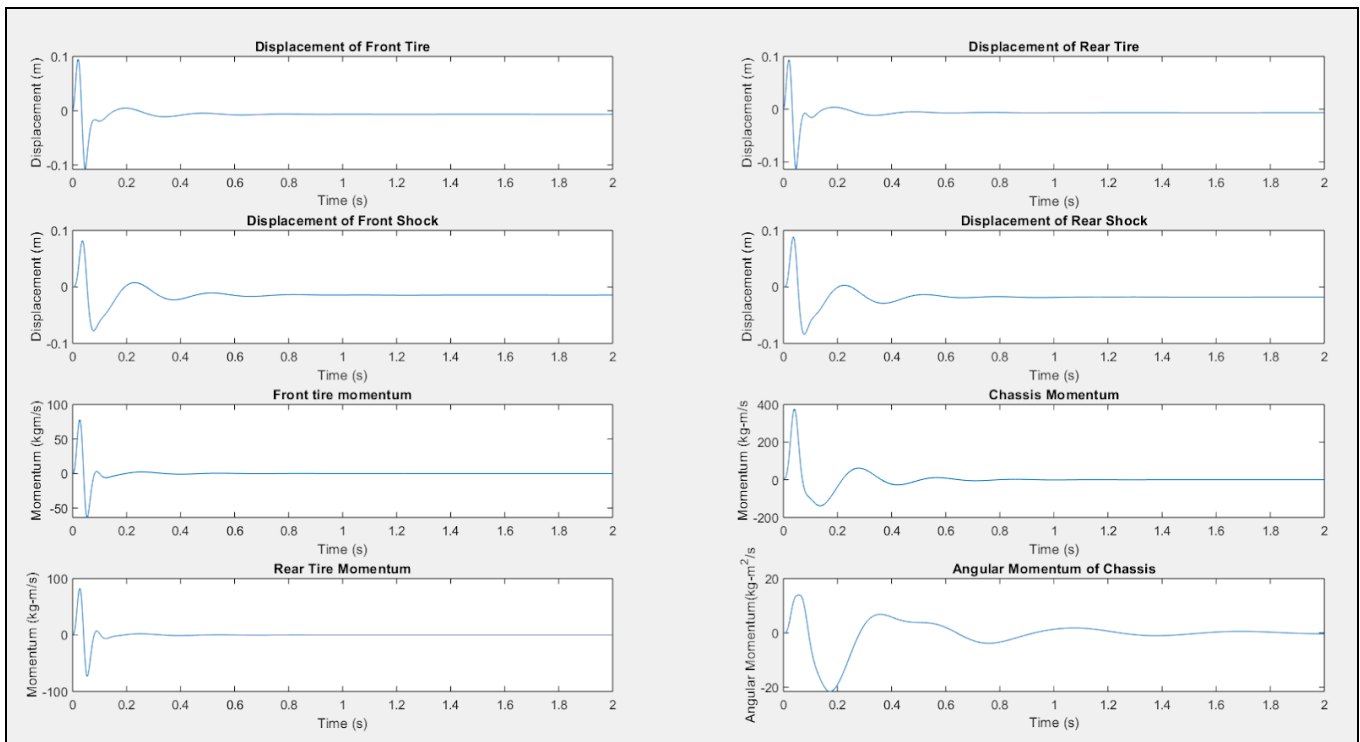
Figure 98: *Piecewise bump formula.*

Figure 99: *Plotted response.*

After creating our bond graph, assigning causality, determining our constants, developing state equations, and implementing them in Matlab, we were able to successfully model the vertical travel of the front and rear shocks following an irregularity on the road surface. This vertical travel was represented by the variables X_3 and X_4. A key decision was to model our flow input from the road surface as a piecewise function, which significantly improved the accuracy of our model. While not yet perfect, our model produced results that were well within an order of magnitude of the expected response of the system, and we expect it will prove useful in tuning our shocks to achieve the desired ride response. The assumptions made in the modeling process proved to be reasonable. While experimentally determined values for some of our constants would have been preferable to our calculated estimates, it appears that they were not necessary to achieve a model accurate

enough for our intended application. The use of dynamic values for stiffness and damping coefficients would likely have further increased our model's accuracy, and is an area for further study and development.

Suspension Geometry

Our frame geometry was based off last years design of a pullrod system, and because of this our team was able to modify the previous years 3D suspension mockup in SolidWorks to match our new suspension parameters, as seen in Figure 100.
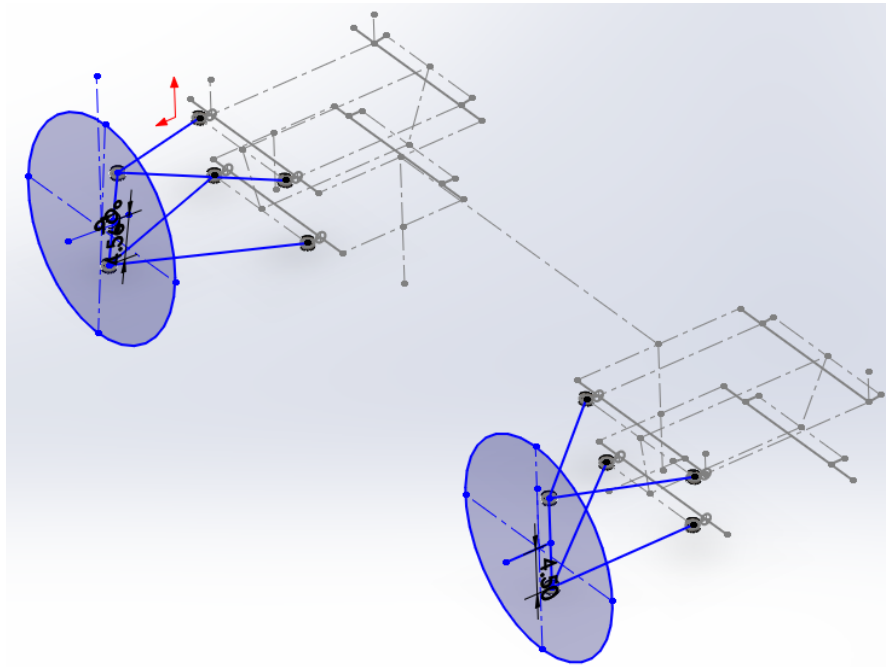

Figure 100: *3D initial sketch.*

Although based on last years design, the suspension system still requires assumptions. Ideal characteristics, such as desired ride frequencies or ideal roll centers, have to be determined based on previous gathered data or rule of thumb if full knowledge of all suspension components is not known.

Our team utilized last years car data to refine our suspension system to further optimize the suspension system, along with analyzing tire data from Milliken Research Associates to help determine ideal spring and damper rates for our assumed ride frequencies.

Although our team designed the suspension in parallel to the frame, due to the frame being similar in design, ride height was kept the same at 5.3" to comply with rule T.2.26.4. In the future, ride height should be lowered. Along with this, mounting locations were relatively similar to the previous years car, which lead to a higher roll center in the front. Front roll center is 2.896", rear roll center is 2.149", which is similar to the previous years. This is not a worry for our team though, as a higher roll center in the front leads to to a more responsive car and better performance for quick turns[10], and previous years data has shown that our performance with this setup was effective. For future recommendations, the conventional way is to have a higher roll center in the rear, this causes less lateral forces in the front, which combats understeer [10].

The previous years car almost failed the tilt test, and has therefore lead to an additional track width adjustment of 2" total, as seen in Figure 101.
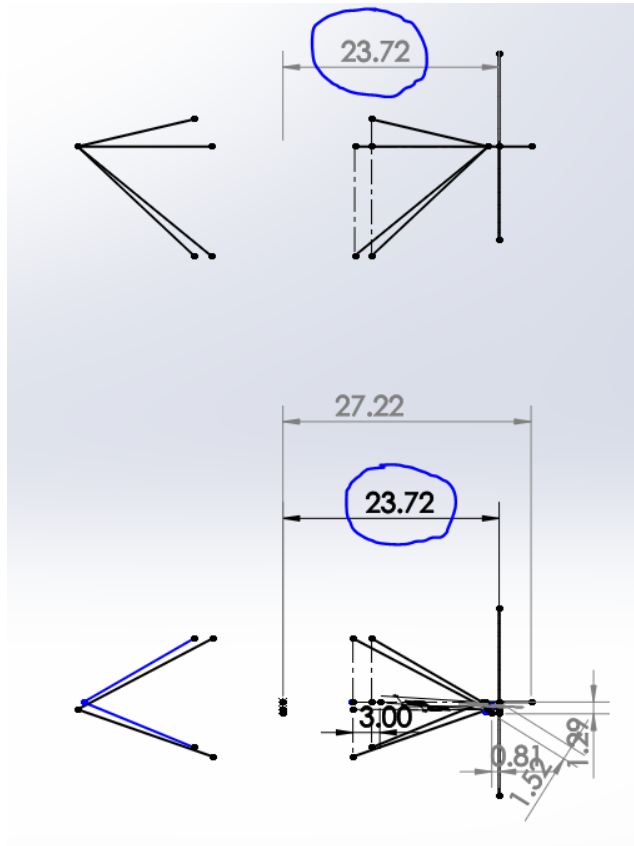

Figure 101: *Track width of new car.*

Along with this, tabs were increased in size from 1" to 1.25" on the top and 1.375" on the bottom due to control arm contact with nodes throughout motion, as seen in Figure 102:
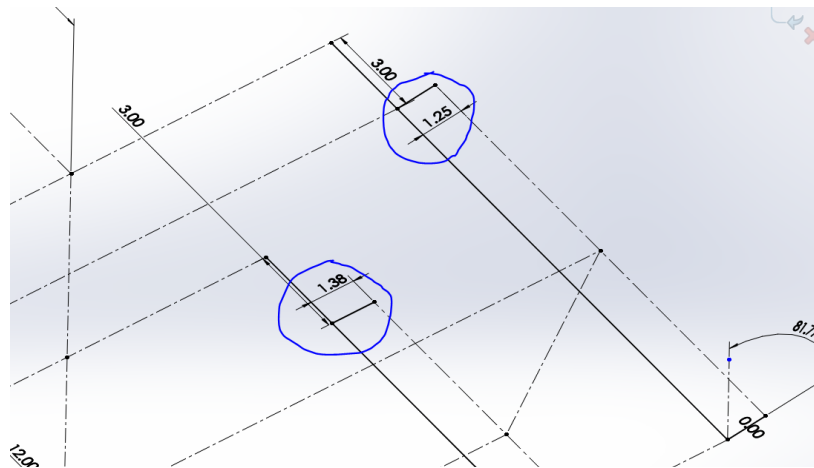

Figure 102: *New tab lengths.*

Since mounting locations and track width were now defined, the model was then translated into OptimumKinematics, which is a suspension software to help suspension design and data collection, as seen in Figure 103.
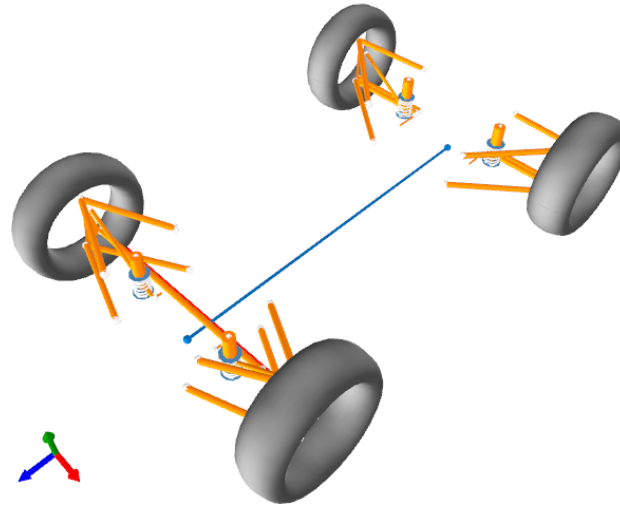

Figure 103: *OptimumKinematics model of new car.*

Before the a-arms could be finalized and data collected, our team had decided to create new uprights, allowing us to change the characteristics and geometry of the suspension slightly.

To finalize the suspension geometry and begin collecting data from OptimumKinematics, mounting locations had to be selected for the uprights. This means that camber, caster, and kingpin had to be defined.

Camber is the measure in degrees of the difference between the wheels vertical alignment perpendicular to the surface [11], as seen in Figure 104.
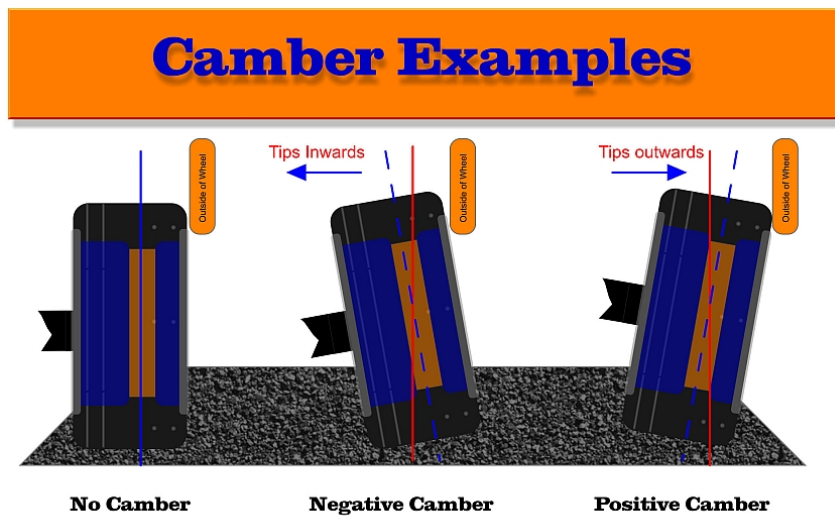

Figure 104: *Camber example* [12].

The previous years suspension system had accidently built camber into both the uprights and the a-arms, leading to too much camber in the wheels. This year, camber was removed completely from the a-arms and would only be built into the uprights. The camber chosen for this year was a variable amount, both 1, 1.5, and 2 degrees of negative camber in the front and .25,.5, and .75 negative in the rear. These were chosen after discussing with Bill Gendron, who owns Small Fortune Racing and provided his past experience with designing similar vehicles for autocross events. These variable camber angles allow for driver exchangeability depending on driver preference. Different camber angles have different benefits. Positive camber provides the vehicle with more stability[14], while negative camber allows for more wheel surface contact throughout turns [14].

Caster is the angle created by the steerings pivot point from the front to back of the vehicle [11], as demonstrated in Figure 105.
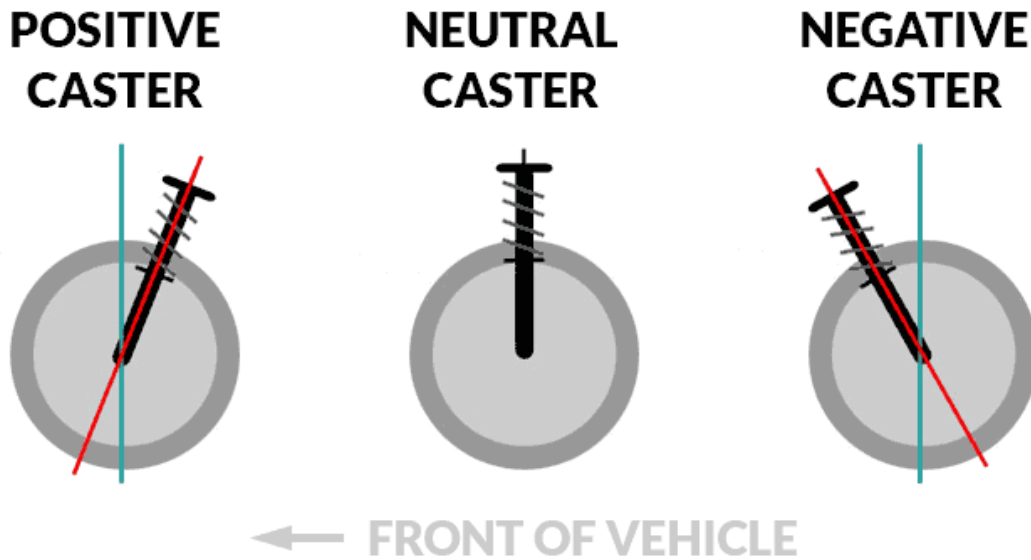

Figure 105: *Caster examples* [13].

Positive caster will increase tire learn during turning but also provide more vehicle stability during high speeds [11]. Positive caster will also increase the steering effort required, and without power steering too much positive caster can make turning extremely difficult [15]. The previous years car had a 4.8 degrees caster angle, which was kept the same as this year because our team had liked the steering performance it provided.

Kingpin is defined as the angle between the steering axis and an axis extending perpendicular from the contact patch[16]. A diagram of this can be seen in Figure 106.
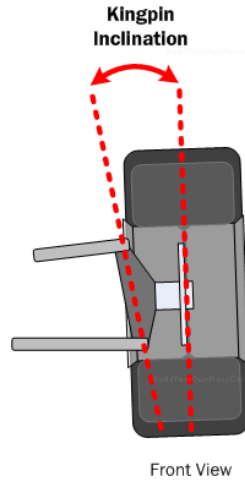
Figure 106: *Kingpin example.* [17]

The previous year had a kingpin angle of 2.3 degrees in the front. This year it was increased to 3.909, with a scrub radius of 0.79", as to allow for a smoother turn, but still retain its responsiveness.

This information was then imported into the OptimumK software. Simulations were then run to represent bump scenarios, seen in Figure 107, and our team was able to further analyze our car throughout ride conditions. Along with this, information such as roll centers and camber change were able to be easily collected from the software, as seen in figures 108 and 109.
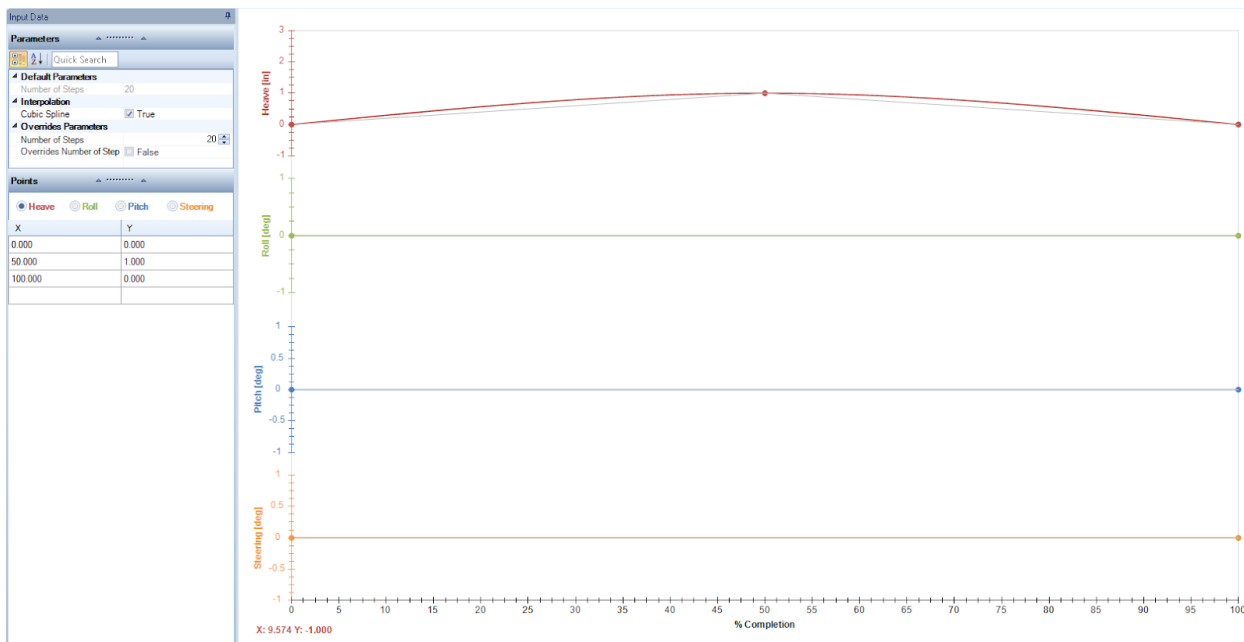

Figure 107: *Information input for OptimumK simulation.*

	Single Left Wheel Motion Ratio CoilOver [Rear Left] (-)	Single Right Wheel Motion Ratio CoilOver [Rear Right] (-)	Single Right Wheel Motion Ratio CoilOver [Front Right] (-)	Single Left Wheel Motion Ratio CoilOver [Front Left] (-)	Scrub Radius [Front Left] (in)	Camber Angle [Front Left] (deg)	Camber Angle [Front Right] (deg)	Kinematic Roll Center Y (Ground) [Front] (in)	Kinematic Roll Center Y (Ground) [Rear] (in)	Camber Angle [Rear Right] (deg)
Maximum Value	1.058	1.058	1.196	1.196	8.05E-1	-3.83E-1	-3.83E-1	4.640	3.565	8.81E-2
Minimum Value	1.017	1.017	1.014	1.014	7.85E-1	-1.500	-1.500	2.896	2.149	-7.5E-1
Average Value	1.039	1.039	1.120	1.120	7.94E-1	-8.35E-1	-8.35E-1	3.929	2.989	-2.48E-1
Start Value	1.018	1.018	1.014	1.014	8.05E-1	-1.500	-1.500	2.896	2.149	-7.5E-1
End Value	1.017	1.017	1.014	1.014	8.05E-1	-1.500	-1.500	2.896	2.149	-7.5E-1
Max Absolute Value	1.058	1.058	1.196	1.196	8.05E-1	1.500	1.500	4.640	3.565	7.5E-1
Variance Value	1.87E-4	1.87E-4	3.63E-3	3.63E-3	4.51E-5	1.37E-1	1.37E-1	3.34E-1	2.2E-1	7.68E-2
Std Deviation Value	1.37E-2	1.37E-2	6.03E-2	6.03E-2	6.71E-3	3.7E-1	3.7E-1	5.78E-1	4.69E-1	2.77E-1
Step [0]	1.018	1.018	1.014	1.014	8.05E-1	-1.500	-1.500	2.896	2.149	-7.5E-1
Step [1]	1.022	1.022	1.040	1.040	8.03E-1	-1.332	-1.332	3.154	2.360	-6.21E-1
Step [2]	1.027	1.027	1.065	1.065	8.01E-1	-1.168	-1.168	3.407	2.566	-4.96E-1
Step [3]	1.032	1.032	1.090	1.090	7.98E-1	-1.011	-1.011	3.651	2.764	-3.77E-1
Step [4]	1.037	1.037	1.113	1.113	7.96E-1	-8.64E-1	-8.64E-1	3.881	2.951	-2.67E-1
Step [5]	1.042	1.042	1.135	1.135	7.93E-1	-7.31E-1	-7.31E-1	4.090	3.120	-1.67E-1
Step [6]	1.047	1.047	1.154	1.154	7.9E-1	-6.14E-1	-6.14E-1	4.273	3.269	-8.14E-2
Step [7]	1.051	1.051	1.172	1.172	7.88E-1	-5.18E-1	-5.18E-1	4.426	3.392	-1.06E-2
Step [8]	1.055	1.055	1.185	1.185	7.86E-1	-4.45E-1	-4.45E-1	4.541	3.485	4.27E-2
Step [9]	1.057	1.057	1.191	1.191	7.85E-1	-3.99E-1	-3.99E-1	4.615	3.544	7.64E-2
Step [10]	1.058	1.058	1.196	1.196	7.85E-1	-3.83E-1	-3.83E-1	4.640	3.565	8.81E-2
Step [11]	1.057	1.057	1.194	1.194	7.85E-1	-3.99E-1	-3.99E-1	4.615	3.544	7.64E-2
Step [12]	1.055	1.055	1.185	1.185	7.86E-1	-4.45E-1	-4.45E-1	4.541	3.485	4.27E-2
Step [13]	1.051	1.051	1.171	1.171	7.88E-1	-5.18E-1	-5.18E-1	4.426	3.392	-1.06E-2
Step [14]	1.047	1.047	1.155	1.155	7.9E-1	-6.14E-1	-6.14E-1	4.273	3.269	-8.14E-2
Step [15]	1.042	1.042	1.135	1.135	7.93E-1	-7.31E-1	-7.31E-1	4.090	3.120	-1.67E-1
Step [16]	1.037	1.037	1.113	1.113	7.96E-1	-8.64E-1	-8.64E-1	3.881	2.951	-2.67E-1
Step [17]	1.031	1.031	1.090	1.090	7.98E-1	-1.011	-1.011	3.651	2.764	-3.77E-1
Step [18]	1.026	1.026	1.064	1.064	8.01E-1	-1.168	-1.168	3.407	2.566	-4.96E-1
Step [19]	1.022	1.022	1.040	1.040	8.03E-1	-1.332	-1.332	3.154	2.360	-6.21E-1
Step [20]	1.017	1.017	1.014	1.014	8.05E-1	-1.500	-1.500	2.896	2.149	-7.5E-1

Figure 108: *Output from OptimumK simulation.*

Figure 109: *More outputs from OptimumK simulation.*

Compared to the previous year, OptimumKinematics streamlined the suspension geometry design process. It allowed for quick data collection and also suspension changes. Originally, our team had attempted to utilize SolidWorks block diagrams to collect this data, seen in Figure 110, but deemed this technique to be extremely time inefficient and chose to utilize OptimumKinematics instead.
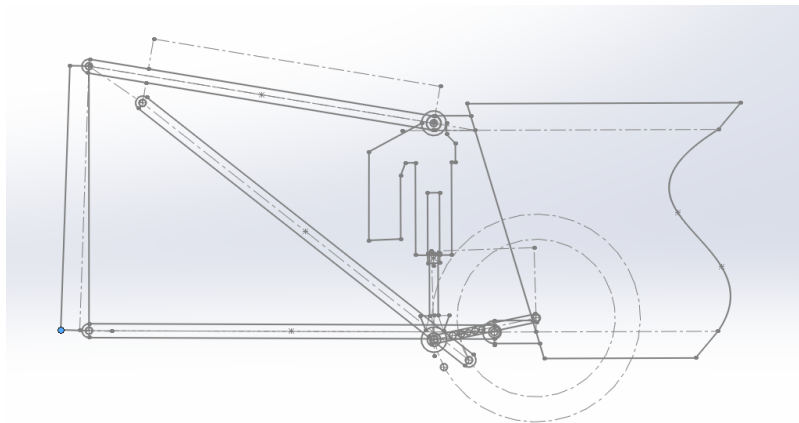

Figure 110: *SolidWorks block diagram of potential new suspension system.*

A-Arm Design

After all the information for suspension geometry was processed in OptimumKinematics, it was then translated back into the SolidWorks 3D sketch. The tubes were then generated and exported as new parts, represented in Figure 111.
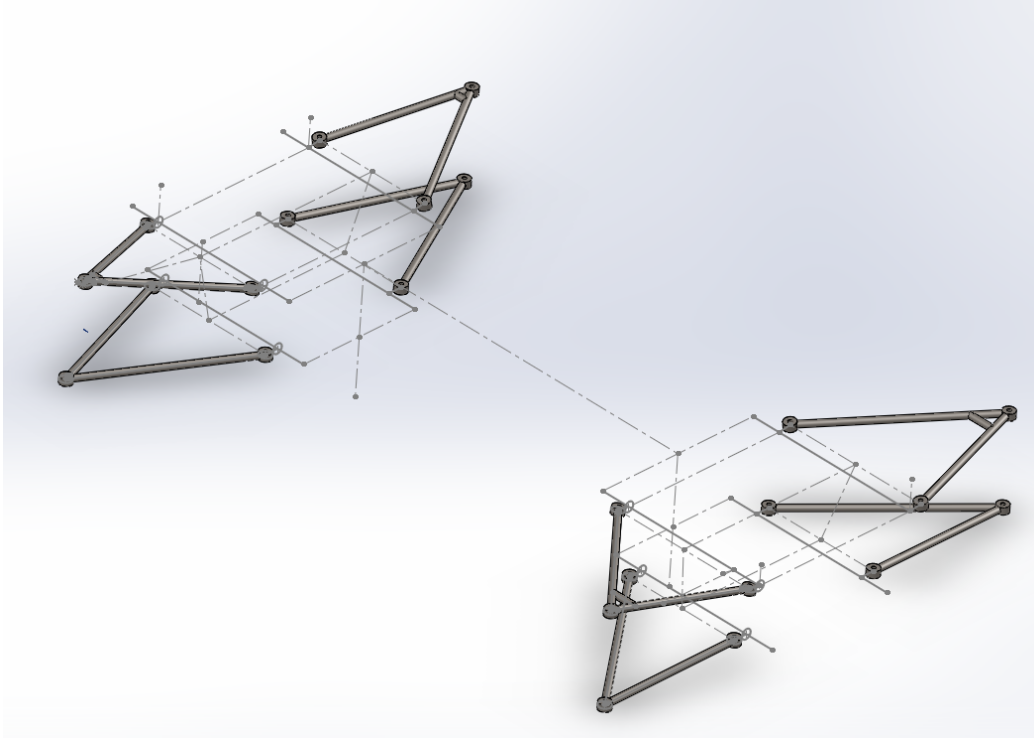

Figure 111: *A-arms generated as new parts and put into assembly.*

The material selected was 4130 steel tubing for its high strength and low weight properties. The tubing outer diameter is .625" and inner diameter is .509". This material also proved itself reliable by being used for the a-arms from the previous years car.

FEA's were run on the the control arms given a 1.5G braking, acceleration, and cornering force. These scenarios were recommended by FSAE literature and the previous years suspension team. Utilizing this information and the equations presented by Carroll Smith in Tune to Win [18], seen in Figure 112, forces were calculated, which can be found in appendix D.

$$\text{Lateral load transfer (lb)} = \frac{\text{Lateral acceleration (g) x weight (lb) x c.g. height (inches)}}{\text{Track width (inches)}}$$

$$\text{Longitudinal load transfer} =$$
$$\text{acceleration (g) x} \quad \frac{\text{Weight (lb) x cg height (inches)}}{\text{Wheelbase (inches)}}$$

Figure 112: *Load transfer weights for a-arms.*

These FEA's parameters were run last year as well, and were proven to be correctly set up by physical testing of last years car. The minimum safety factor was 3 at the rear upper control arm position, as seen in Figure 113.
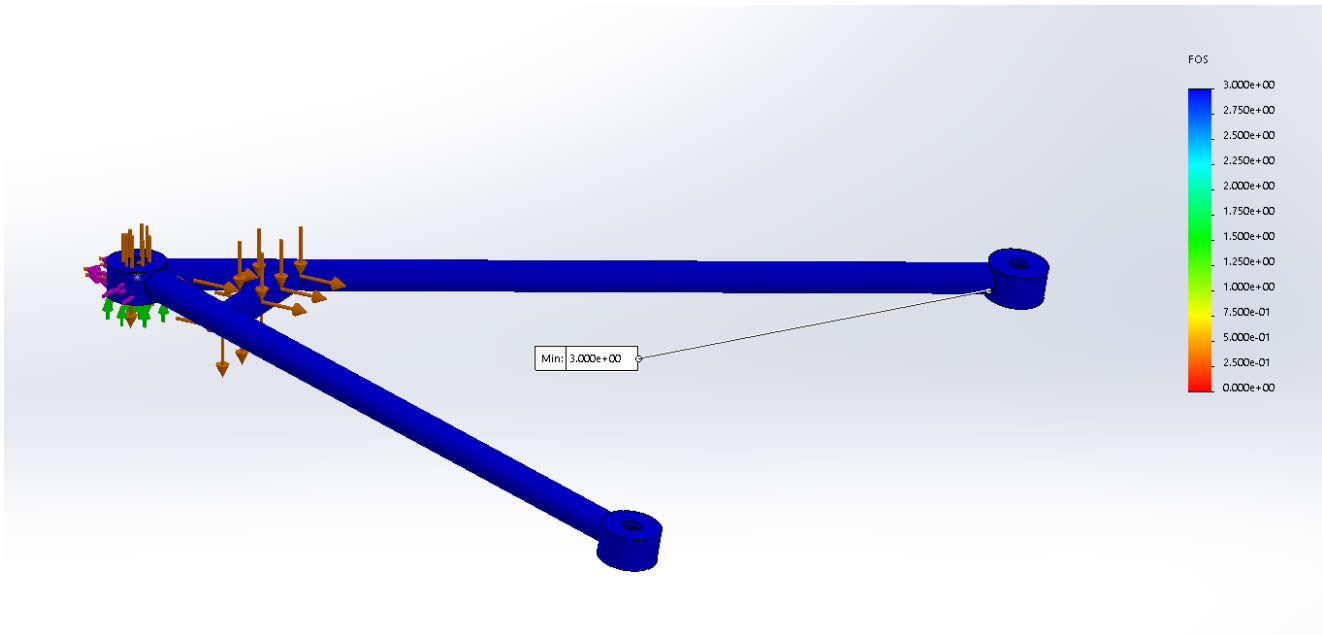

Figure 113: *A-arm Factor of safety FEA.*

Fabrication of the control arms required custom tooling to ensure correct fitting when installed on the car. To do this, 3d printed custom parts were designed. These parts, seen in Figure 114 and 115, held the control arm in the correct position during welding. Without these parts, welding the control arms in the correct orientation is nearly impossible.
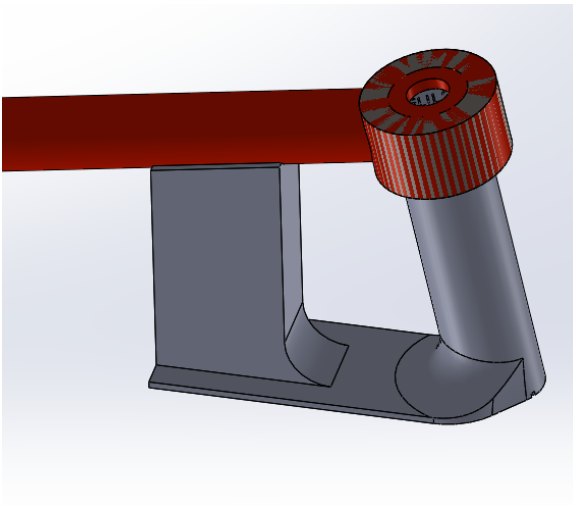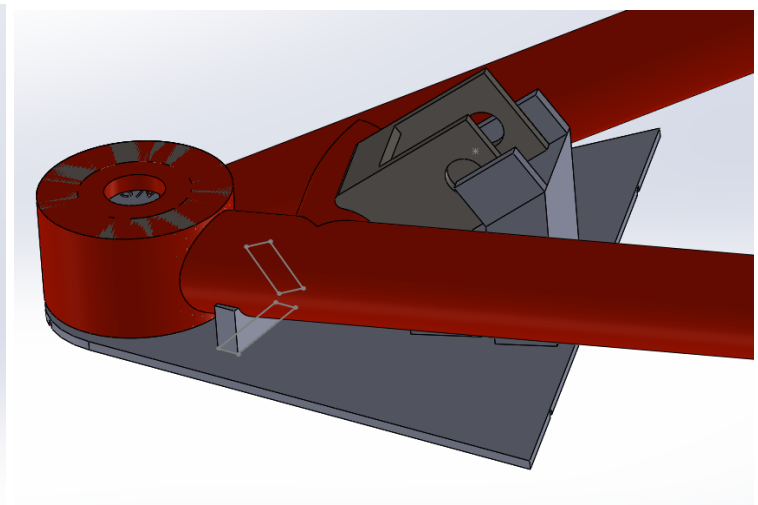

Figure 114: *Frame side control arm jig*

Figure 115: *Wheel side control arm jig*

Upright Modifications

This year our team decided to change the past years uprights. Last years uprights contained camber in both the uprights and the control arms. The camber was non adjustable, and upright mounting positions had play due to being unable to have the upright material flex and compress the control arm in position. Last years front upright can be seen on the left in Figure 116, this years front upright is pictured in Figure 117.
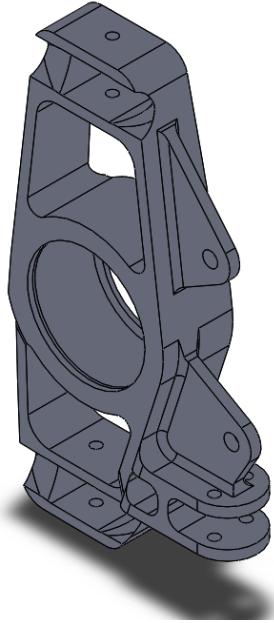
Figure 116: *Previous years front upright.*
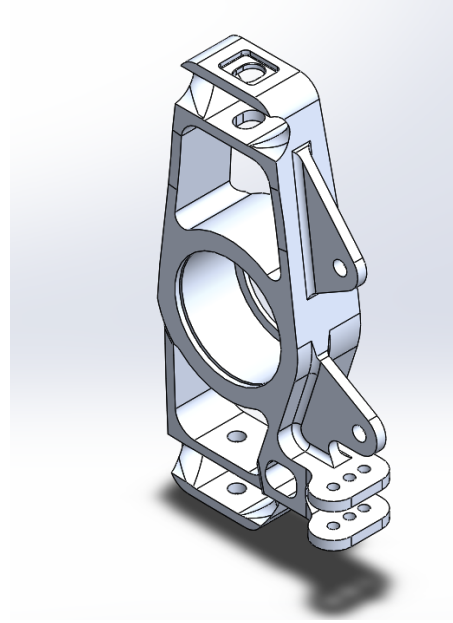
Figure 117: *New upright design.*

Our teams solution to the non adjustable camber was to create "camber blocks" which are inserts, as seen in Figure 118, that have the control arm bolt hole drilled in different positions to provide different camber values. Installing a camber block with the hole in the center of the insert will give a camber angle equal to the chosen static camber value. Different sets of inserts are made with offset holes to allow for changes in camber adjustment. This design allows for a quick suspension geometry adjustments, seen in Figure 119..

Figure 118: *Camber insert.*

Figure 119: *Block inserted in upright.*

Along with this, the upright mounting holes were increased from .25" to .375". This allowed a larger bolt to be inserted, which will allow our team to apply more compression force on the a-arm mounting locations within the upright to avoid any slop that may have come from machining tolerances.
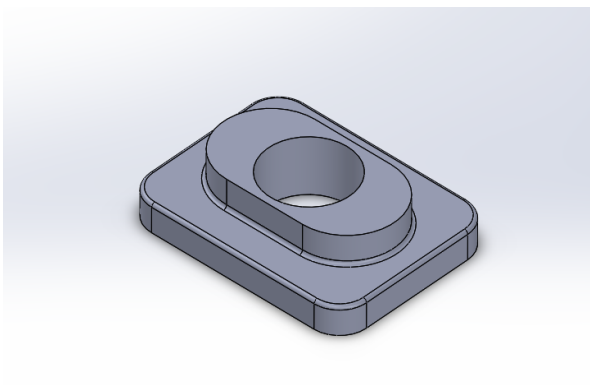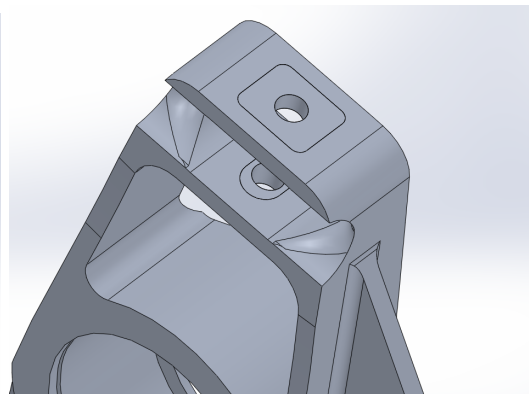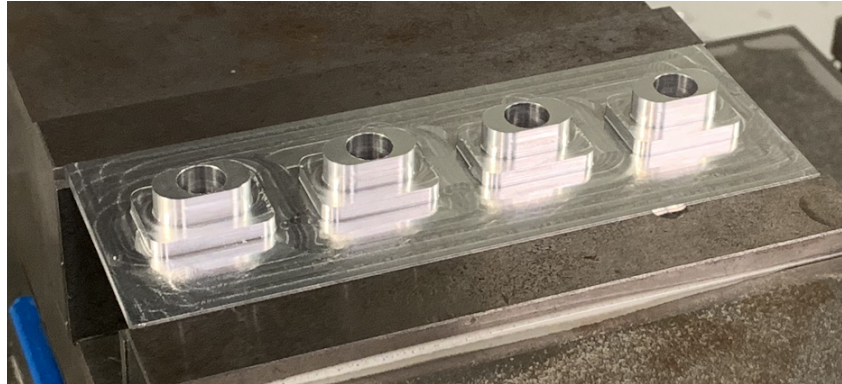

Figure 120: Manufactured camber inserts

FEA analysis was run on the front and rear uprights for braking and bump conditions. The biggest issue our team ran into while attempting these analysis' was determining how to fixture the camber blocks. In order to solve this, our team utilized the no penetration connection applied to the camber blocks and the inside of the upright. This contact set was needed to simulate the small amount of space between the camber block and the upright due to machining tolerances and would accounted for any direct bearing stress that could potentially cause failure from tearout. Force loads were added to each camber block to simulate the the tightened control arm bolt retaining the blocks in the upright. Similar to the a-arms, forces were calculated based on 1.5g scenarios, as recommended from SAE literature and previous years experiences. Analysis and settings can be seen in Figures 120-123. Figure 120 shows the final manufactured camber inserts.
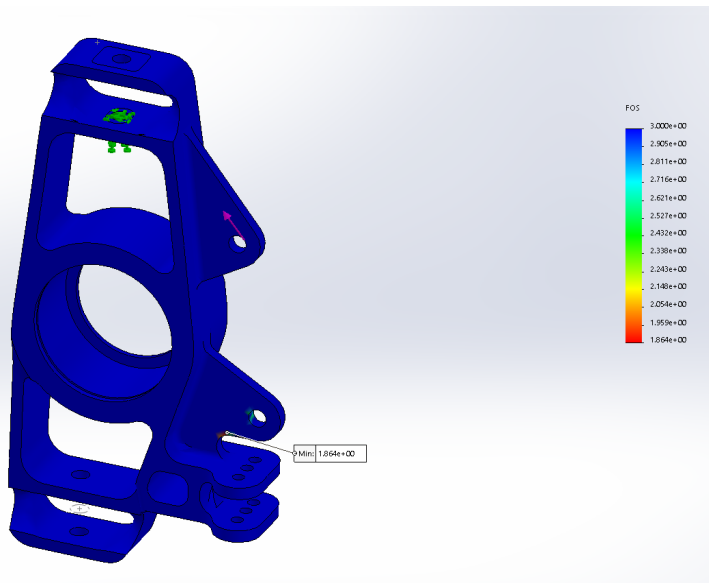
Figure 121: *Front upright braking analysis factor of safety*
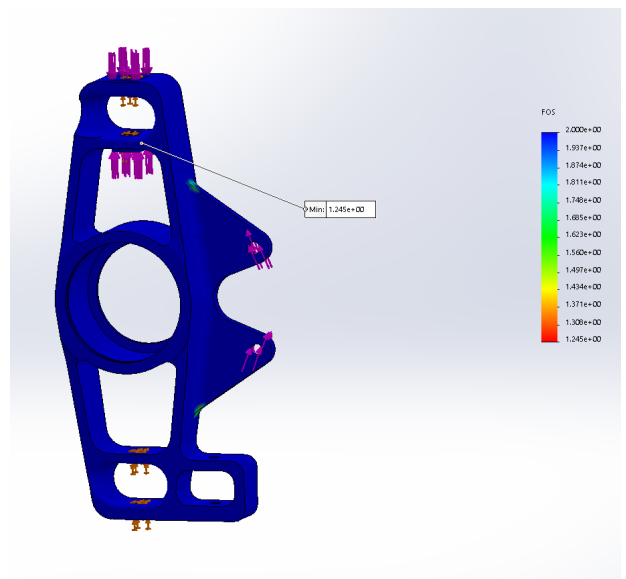
Figure 122: *Rear upright braking analysis.*
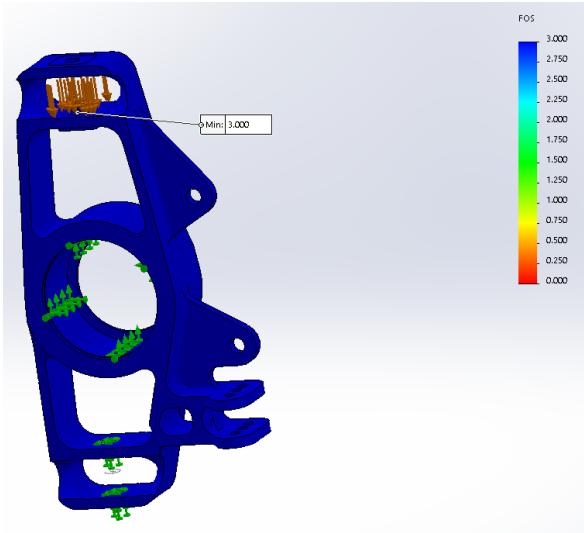
Figure 123: *Front upright bump FEA.*
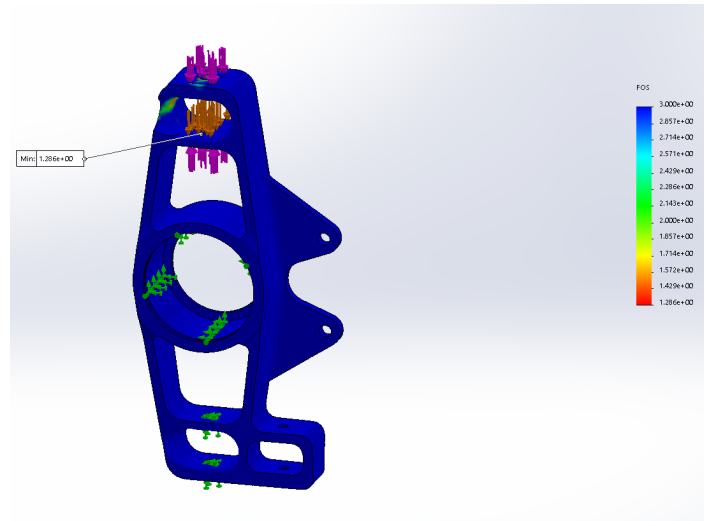
Figure 124: *Rear upright bump FEA.*

Rocker Design

Discussing with Bill Gendron, who had helped our team with deciding on camber values, the recommendation for FSAE car rocker motion ratios is 1:1 front and rear. Motion ratios are defined as wheel travel divided by spring travel. Last years car developed a rocker with a motion ratio of 1.3:1 front, and used the same rocker for the rear, causing the rear to be 1.4:1. The previous years rocker can be seen in Figure 125
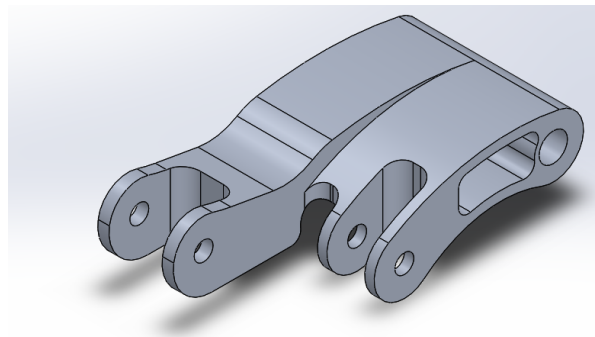
Figure 125: *Previous year's rocker.*

Tab locations were determined before the rocker was designed, and imported into the OptimumKinematics car model. The OptimumKinematics model was then adjusted to provide our current car with motion ratios ~1 for front and rear. After the mounting locations were determined, Rocker geometry was developed in SolidWorks, as seen in figures 126 and 127.

Figure 126: *Front rocker.*

Figure 127: *Rear rocker.*

Rocker material was originally 7075 T6 Aluminium due to its lightweight properties and high strength, but was later changed to 7075 T7 for the purpose of being more affordable. The properties of T6 and T7 are extremely similar, and therefore do not have an impact on our rockers strength or weight. Weight was also reduced on our rockers, at .3 lbs for each front rocker and .26 lbs for each rear, compared to .334 lbs per last years rocker.

An FEA was ran on the rockers with a total lateral load estimate of 1000 lbs. This is a worse case scenario, and had to be estimated due to not having actual information required for lateral load calculations, such as the center of gravity of our new car. This estimate was developed through information passed on from experience with the the 2017-2018 year car, seen in figures 128 and 129.
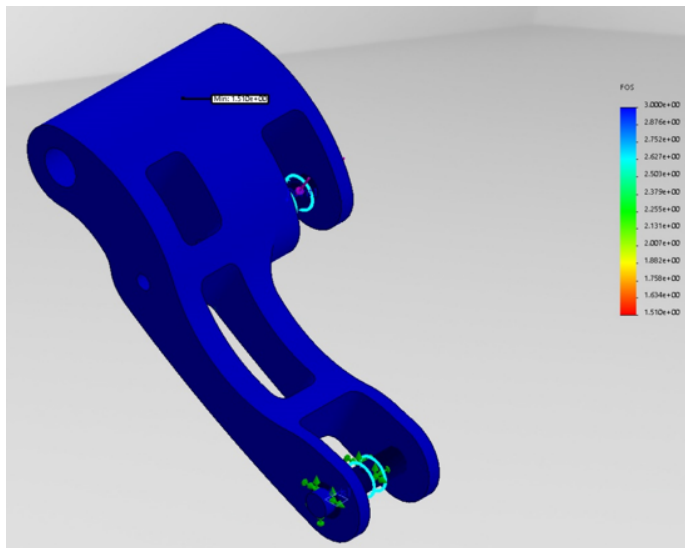
Figure 128: *Front rocker factor of safety.*
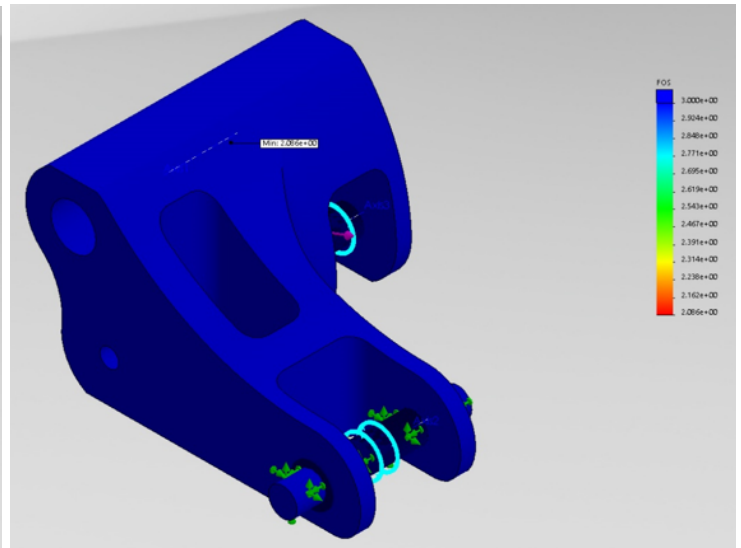
Figure 129: *Rear rocker factor of safety.*

Once geometry was created, the front and rear rockers were 3D printed to verify compatibility with our actual frame. The front rocker mounting position stayed the same as the previous years, and the 3D part in Figure 130 was installed on the previous years car to show functionality. The rear mounting position had

changed from the previous year, and therefore a mock rear frame mounting position had to be 3D printed as well, seen in Figure 131. Figure 132 shows the manufacturing process for the rear rocker and Figure 133 shows the final manufactured front right rocker.

Figure 130: *3D printed front rocker.*

Figure 131: *Rear suspension mockup*
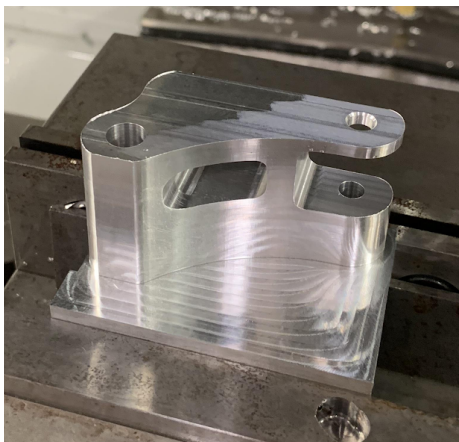
Figure 132: *Rear Rocker Machining*

Figure 133: *Front right rocker*

Recommendations

The first recommendation for next years team is to lower the ride height. This will require re-designing the frame even more than we have for this current year to comply with the rules. With this redesign, also attempt to lower the roll centers by relocating the node mounting points for the control arms and have the rear roll center higher than the front, as discussed in the report above.

The second recommendation is to attempt to create a rocker where the pullrod and shock mounting points are in-line with each other. Currently, when the shock exerts a force on the rocker, it creates a moment on the tabs due to the pullrod not being in-line. Our current mounting set-up prevents the inline geometry, so a new mounting location for the shocks and rockers should be researched to achieve this for the future rocker design.

Steering

System overview and mechanical design

The steering system allows control of the direction of the vehicle, and is one of the most complex and critical links between the driver and the race car. The steering system has been defined as including all assemblies and components from the steering wheel to the steering clevis on the front uprights.

The new steering wheel is a clean sheet design, completed with significant involvement from members of the WPI SAE club. The new wheel was designed to address issues with the previous version identified by team drivers. First, the previous generation wheel is only 10" and is a standard circular layout, limiting the amount of torque the driver can effectively apply. Our new design uses a race wheel layout with thumb cutouts, allowing the driver to apply additional force to the turn. Second, the 2018 design was not built to accommodate our electronic shifting system, which was difficult to reach while steering. Additionally, the wiring for the mounted shift display and shift levers was exposed, problem for a moving component in such an exposed area. The new wheel fully protects the wiring by running it through the shifter housings, which have been redesigned to use magnets to provide a clean, tactile break while shifting. The wheel was constructed from ¼" 7075 Aluminum plate with PLA handles (Figure 134).
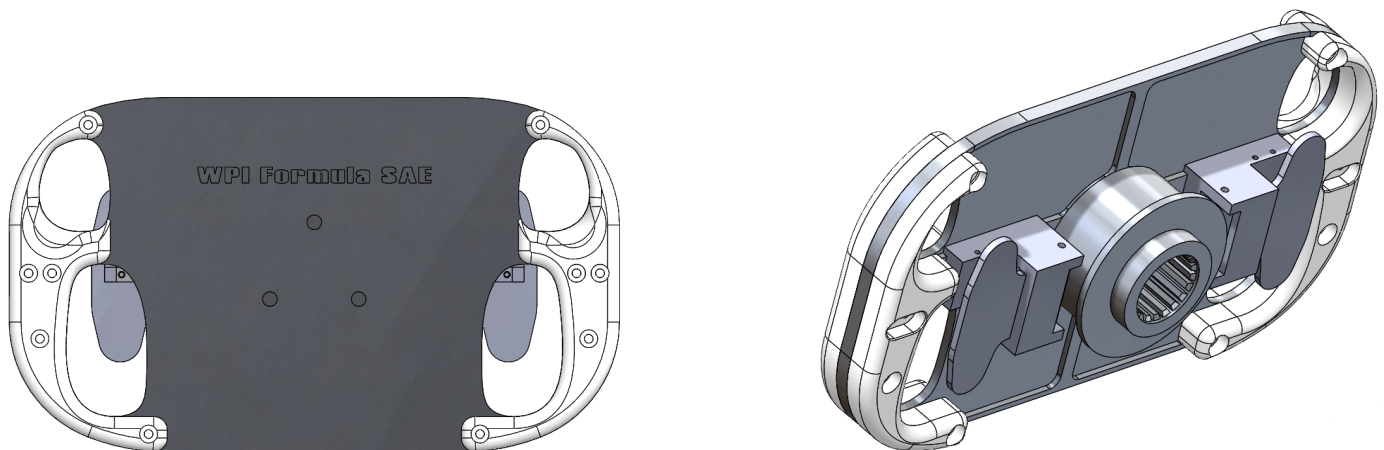
Figure 134: *New steering wheel assembly.*

The steering wheel is attached via a quick detach spline shaft, which allows the driver to rapidly remove the wheel in the event of an emergency. The 2018 vehicle's spline shaft and collar assembly had been reused on multiple vehicles, and was well worn. As such the decision was made to replace it with the QR 1 Quick Detach assembly from SPA Technique (Figure 135). This shaft offered three key essential features which led to it's selection. The shaft is drilled through, allowing the pass through of wires needed for shifting controls. The shaft features a masterkey, meaning the steering wheel can only be placed in a single position. Not only does this

mean that the steering wheel can not be accidently misaligned when being reinstalled, it also allows greater flexibility in the use of directionally dependent connectors for the through shaft wiring. Finally, the shaft is constructed from 4130 steel for better weldability to the upper steering shaft which is made from the same material.

Figure 135: *QR 1 Steering Wheel Quick Release from SPA Technique.*

Figure 136: *Timken LM11949 Bearing*

The upper steering shaft was manufactured made from ¾" 4130 Tubing with a 0.083" wall thickness. The most likely failure mode for the steering shaft was determined to be the bending load applied when a driver attempts to use the steering wheel to lift themselves from the vehicle. For this purpose, the shaft was idealized as a cantilever beam with a 400 lb point load applied straight down at the steering wheel. The 0.083" tubing was found to be sufficient for this loading. The steering shaft will again be mounted to the gearbox with two taper roller bearings mounted in an opposed configuration to solidly position the shaft (Figures 137 & 138).
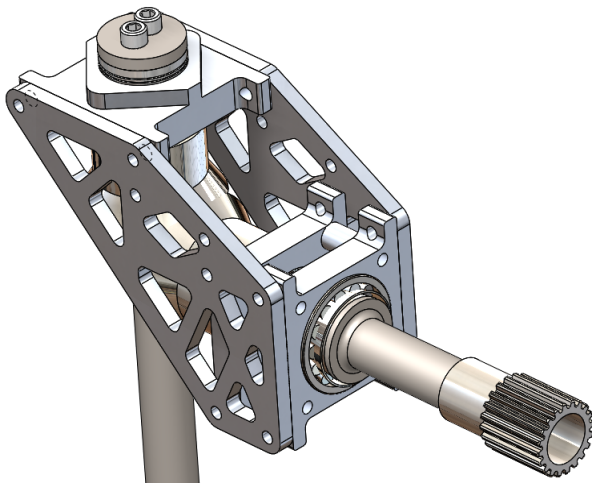
Figure 137: *Steering gearbox.*

Figure 138: *Lower shaft keyway.*

The gearbox was redesigned from the 2019 vehicle with one major change (Figure 137). The gearbox uses two 45° bevel miter gears with a 1:1 gear ratio to transmit the driver's input from the upper to the lower steering shafts. The primary issue identified in this system in the 2018 vehicle was the excessive play caused by the lack of pre tensioning in the taper bearing used to locate the lower steering shaft. To address this issue, two bolts will now be threaded into the steering shaft, transmitting force to the gearbox through a needle thrust

bearing and ensuring that the primary taper roller bearing remains fully engaged. This two bolt arrangement was done to comply with FSAE rules relating to critical fasteners. A single, larger bolt threaded into the shaft was originally considered, but abandoned when it was discovered that it would be impossible to safety wire this assembly. The two bolt arrangement allows the heads to be safety wired together.

The lower steering shaft was constructed from ¾" 4130 Tubing with a 0.083" wall thickness. Here, the primary design constraint was not material yielding but torsional deflection under extreme cornering. All torque applied to the shaft must come from the driver through the steering wheel. Based on external research conducted on student drivers as well as industry standards, a maximum driver applied torque of 130 ft lbs was assumed. A limit of 5° of torsional deflection was set and available tube thicknesses were checked against this until the thinnest possible tube which met this specification was identified. The spline collar, which mates the lower steering shaft to the steering rack was recovered from last years assembly, refinished on a lathe, and welded to the bottom of the lower steering shaft

The Kaz steering rack used by the 2018 vehicle was a significant investment for the team and performed well, ands as such will be used in the 2019 vehicle. This rack has a total travel of 3.25" over 246° of rotation. The steering rack is attached to the car via manufacturer supplied aluminum shaft collars which bolt on to four mounds made from 4130 square tubing which are welded to the frame. The steering rack is attached to the uprights by a pair of 4130 tie rods with nuts welded to either end to allow the attachment of the ball joint ends which ensure the tie rod is only in tension or compression. The tubing has a ⅜" OD and an .049" wall thickness, with a left and right hand nut welded to either end. The use of left and right hand nuts and ball joints allows the adjustment of the steering toe without removal.

Steering Geometry

The geometry of the steering system is essential to influencing how the car handles on the track. The first value which needed to be defined was the maximum turn radius. SAE publishes an overview of the course, along with specifications for corners, from which we were able to determine the carr will need a 14.75' turn radius at the outside wheel. As the maximum travel of our steering rack is defined by the manufacture, the only variable available to adjust turn radius is the position of the pickup points on the upright. The key variable is the distance by which the axis or rotation between the upright and tie rod trails the kingpin axis of the upright; as this distance increases, the turn radius decreases. For our given rack travel and desired turn radius, it was determined that this distance could be no greater than 3.8". This value was determined iteratively using a 2D Sketch of the steering linkage (Figure 139).
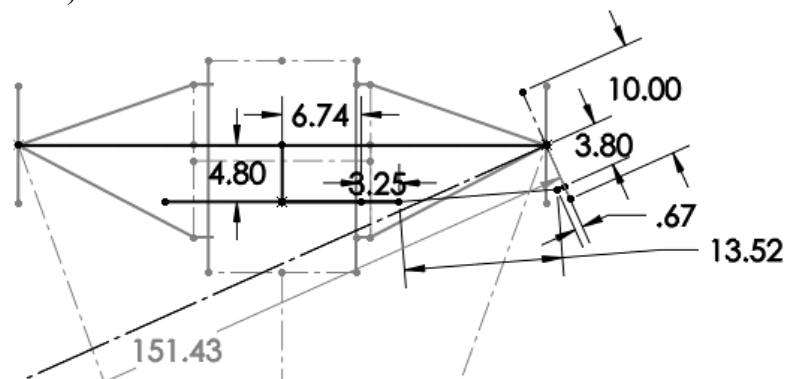

Figure 139: *Sketch used for conformation of the turn radius.*

The next critical value which needed to be determined was the percent Ackerman of the steering system. In a perfectly parallel steering assembly, both wheels remain locked in parallel with each other. This means that each tire is turning about a different point, inducing wheel scrub. Ackerman steering is the implementation of geometry such that both wheels turn about the same center point (Figure 140). This is done by placing the tie rod attachment point such that a line drawn between the kingpin axis and that point intersects the center of the rear axle. While Ackerman geometry works well in low speed low slip corners, at high speeds when wheel scrub increases, this benefit is lost, and parallel steering is preferable. Therefore, it is normally best to design your steering between parallel and full ackerman.
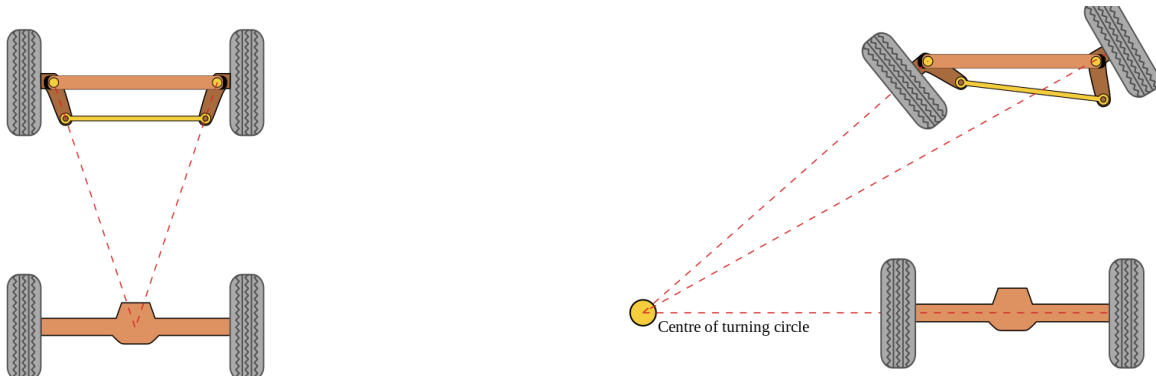

Figure 140: *Sketch of Ackerman Geometry.*

50 % Ackerman was used at competition last year with positive driver feedback, but a review of best practices for vehicles operating at the relatively low speeds found on a FSAE autocross and endurance course indicated that a greater percent ackerman may be preferable, as the technical nature of thee courses means tight turns are often taken at low speed. Therefore it was decided three positions would be available on the upright to adjust ackerman. This posed a challenge, as placing all three holes along the 3.8" offset previously determined in the turn radius design was impossible for the initially desired positions of 30%, 50%, and 70%. Additionally, the design of the upright needed to be modified to remove a support which intersected one of the needed holes. This collison was resolved, and the increments changed to 20%, 50%, and 80%. These positions should allow coarse tuning of the car for varying driving speeds and slip levels. Without tire data and a well developed slip model, the team will rely on tuning the vehicle to driver preference through repeat track sessions.

Implementation and Recommendations

The steering system achieved the primary stated design objectives of eliminating the significant amount of play and backlash found in previous versions. The new wheel was received favorably by our drivers, as were the mounted shifters and associated electronics. The new keyed spline aided significantly in allowing drivers to quickly attach the wheel without need to index, although wear on the spline did reintroduce a small amount of slack. With the taper bearing holding the main shaft properly aligned and gears shimmed, this is the only remaining source of play in the system, resulting in an overall massive improvement in driver feel. The greatest opportunity for future improvement lies in further lightweighting. The hardened steel gears used are sized for a

power transmission application, and could be replaced with far smaller and lighter bevel gears, and the solid steel keyway could likely be lightened significantly with additional turning applications. Overall however, the core system should be maintained unless future vehicle changes make the use of a U-Joint system more viable.

Brakes

Brake System Overview

The braking system is one of the most critical subsystems for both on track performance and driver safety. A well designed braking system is essential for success in the dynamic events and for allowing the driver to safely decelerate the car in the event of unsafe conditions or a mechanical failure elsewhere in the vehicle. Conventional wisdom states that when all other systems have failed, the brakes should be the last system still working. For our use, that means the system must be able to withstand a 450 lbf (2000N) force applied by the driver at the brake pedal. This was the design requirement applied to all components in the assembly.

Three primary design goals drove the redesign of the brake assembly: allow for the adjustment of the pedal position for different driver heights, eliminate play in the bias bar, and reduce unnecessary weight. We aimed to achieve this goal while maintaining the overall driver feel of the system from the 2018 vehicle. To achieve this goal, brake calipers, rotors, master cylinders, and the kinematics of the brake pedal were all held as constants. Our vehicle will again use Wilwood Billet Dynalite Single Calipers with a 2.4 in^2 for the front wheels and Wilwood PS-1 Calipers with a 0.79 in^2 piston area for the rear. The front and rear systems will each be provided pressure through a pair of Wilwood Compact Remote Flange Mount Master Cylinders, with a ¾" front bore diameter and a ⅞ rear bore diameter. These sizes were chosen to attain a brake bias appropriate for the load transfer of the car, with a driver, under 1g of deceleration. The difference in bore size and surface area will provide the coarse balance of the braking system, which will be further tuned at the bias bar.

Brake Caliper and Cylinder Selection

The brake calipers and cylinders were selected by first calculating the weight transfer of the car. The weight transfer relates to the dynamic braking forces needed to slow the car. The inertial forces from the center of mass acting on the suspension cause the weight of the car to transfer forward. The weight bias, or load transfer, in this dynamic case is what the brake bias needs to be set to.

To find the load transfer of the car, this equation is first used:

$$W_R = \frac{W_T * H_{CG} * a_B}{L_{WB}}$$

Table 9: *Variables involved with weight transfer.*

Variable	Value & Unit	Description
W_R	134.21lbf	Effective weight acting on rear wheels in dynamic braking
W_{Tl}	580lbf	Total weight of car with driver
H_{CG}	14in	Height of the center of gravity from the ground
F_B	1	Deceleration achieved by brakes in g's
L_{WB}	61in	Length of the wheelbase, wheel center line to wheel centerline

With the weight acting on the rear wheels calculated, the weight acting on the front wheels can be calculated:

$$W_F = W_T - W_R$$
$$W_F = 445.78 lbf$$

The weight bias percentages can now be calculated. To find the weight bias percentage in the front, the weight over the front wheels is divided by the total weight of the car. For the rear, the rear weight is divided by the total weight.

$$Bias_F = \frac{W_F}{W_T} \quad Bias_R = \frac{W_R}{W_T}$$

The resulting bias is $Bias_F = 76.86\%$ and $Bias_R = 23.14\%$. The brake bias should be this to effectively brake all wheels under 1g of deceleration. The cylinders and calipers purchased by last year's team have a bias of 77% to 23%. They are perfect for this application.

The brake bias describes the ratio of rotor torque between the front and rear wheels. The front and rear rotor torques are both constrained to hold this ratio and must be able to stop the wheel. A newtonian approach can be taken to solve for the required rotor torque on the front and rear wheels. The rotor torque can be found by the amount of force acting on the brake, the lever ratio of the brake pedal, the diameters of the master cylinders, diameter of the calipers, area of the brake pad, coefficient of friction of the pad, and diameter of the rotor. The bias of the brake rotor torques must satisfy the dynamic load transfer. The front and rear brake calipers, cylinders, and rotor diameter produce a bias of 83.7% front and 16.3% rear. The ideal bias would be around 77% front and 23% rear. By adjusting the brake bias bar, the brake bias can be set to this bias. See appendix F for more information.

The pedal subsystem has been modified from the previous year's to be adjustable with respect to the length of the driver's legs. This functionality was desired because the seat is in a fixed position and if the pedals do not allow enough leg room or are unreachable, the driver's ability to handle the car comfortably is limited. The pedal assembly will be manufactured as a subframe that drops in to the frame of the car. There are three tab locations that the subframe can be mounted to, allowing for a short, medium, and tall driver pedal configuration. The pedal frame is constructed of welded 4130 chromoly plates, providing a rigid body for the pedals to be attached to (Figure 141). The subframe bolts to the tabs welded to the frame. The subframe sits to the rear of the tabs so the bolts do not undergo tension when the pedals are used. The mating faces of the subframe and tabs will undergo compression and a shear force will be enacted on the weld. The pedal sub assembly will have a carbon fiber floor to protect the master cylinders from the driver's feet. The floor will not cover the frame tabs holding on the subframe on, making the bolts easily accessible for quick adjustment.

Figure 141: *Pedal subassembly in the frame.*

In the 2018 vehicle, a problem was identified late in development that the bias bar was not functioning as designed, but instead was pivoting about an axis parallel with the master cylinders through pivot point of the bias bar. This was mitigated by the use of washers clamping the bias bar in position, a less than ideal solution which nullified the fine adjustment performed by adjusting the bias bar. We identified the source of this problem as the significant distance between the master cylinders, the center to center distance was 3.75", far greater than any commercially available system. We were able to reduce this distance to 2.5", a distance more in line with traditional brake design which should resolve this issue. Doing so required rotating the master cylinders by 45°

to accommodate the flange mounts. The bias bar assembly form the 2018 vehicle showed significant corrosion, and has been replaced with a Tilton 600 series bias bar. This assembly was chosen for its simplicity and the availability of a remote bias adjustment mechanism, which could be added in the future.

Brake Pedal

The brake pedal has been refined from last year's brake pedal. The design of last year's brake pedal was very heavy and overbuilt, with a safety factor of ~10. This safety factor is unnecessarily large. Part of the reason the pedal was overbuilt was because of how it mounted to the pedal subframe. The pedal straddled an aluminum mount that was 0.75" wide, and the pedal had a constant width of 1.5". Because the pedal straddled the mount, the bias bar spherical bearing sleeve had a large amount of unsupported surface area. By changing the way the pedal mounts to two tabs in double shear, the pedal can be made 0.75" wide. The brake bias bar sleeve is 1.5" wide, so the brake pedal needs to become wider at the bottom to fully support it. The pedal has milled out pockets for brass washers to sit concentric with the pivot point to protect the aluminum pedal from the steel tabs while rotating. The new brake pedal, both assembled and plain, can be seen in figure 142.
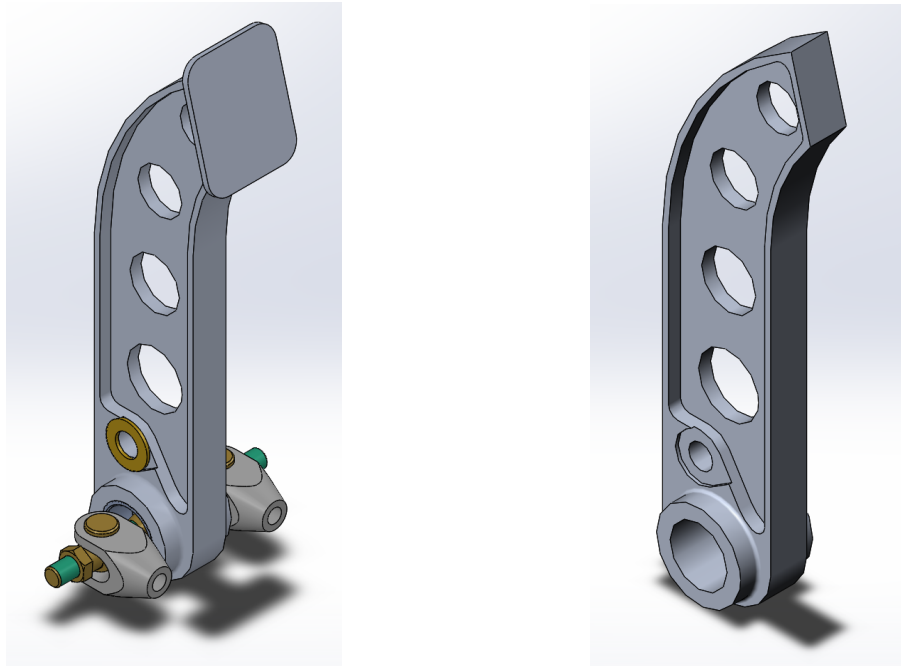
Figure 142: *Assembled brake pedal (left) with stomp plate, washers, and Tilton Bias Bar. Brake pedal (right)*

The dimensions of the brake pedal is based on last year's brake pedal. The main defining size dimensions have remained the same. These dimensions include the size and location of bias bar mount, the size and location of pivot point, and the size and location of the stomp plate mount (Figure 143). The pedal is about one half the weight of the previous year's, 1.5 lbs to 0.78 lbs, and a minimum safety factor of 3.5.

Figure 143: *Size and location of brake bias bar, brake pedal pivot, and stomp plate weld site.*

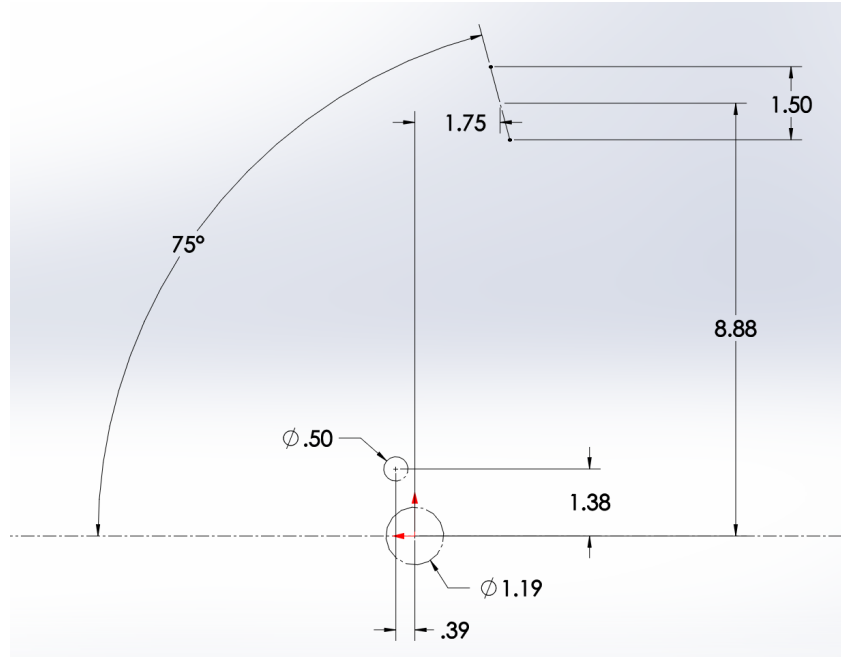Finite element analysis was performed on the brake pedal (Figure 144) to check if the pedal survives under the conditions specified by the rules. T.5.1.10.a specifies that the brake pedal must be designed to withstand a force of 450 lbf (2000N) without failure. The pedal was fixtured so with the pivot hole as a fixed hinge to allow rotation. The bias bar hole was fixed as fixed geometry to simulate the bias bar sleeve pressed in. The force of 450 lbf (2000N) was applied to where the driver presses their foot on the pedal. The 2000N is representative of the driver entering a situation that causes them to press as hard as they can on the brakes to avoid, say, a collision. The results showed a safety factor of 3.353. This safety factor is satisfactory, as it is not as overbuilt as last year's, allowing weight to be saved while maintaining a satisfactory and appropriate part strength.
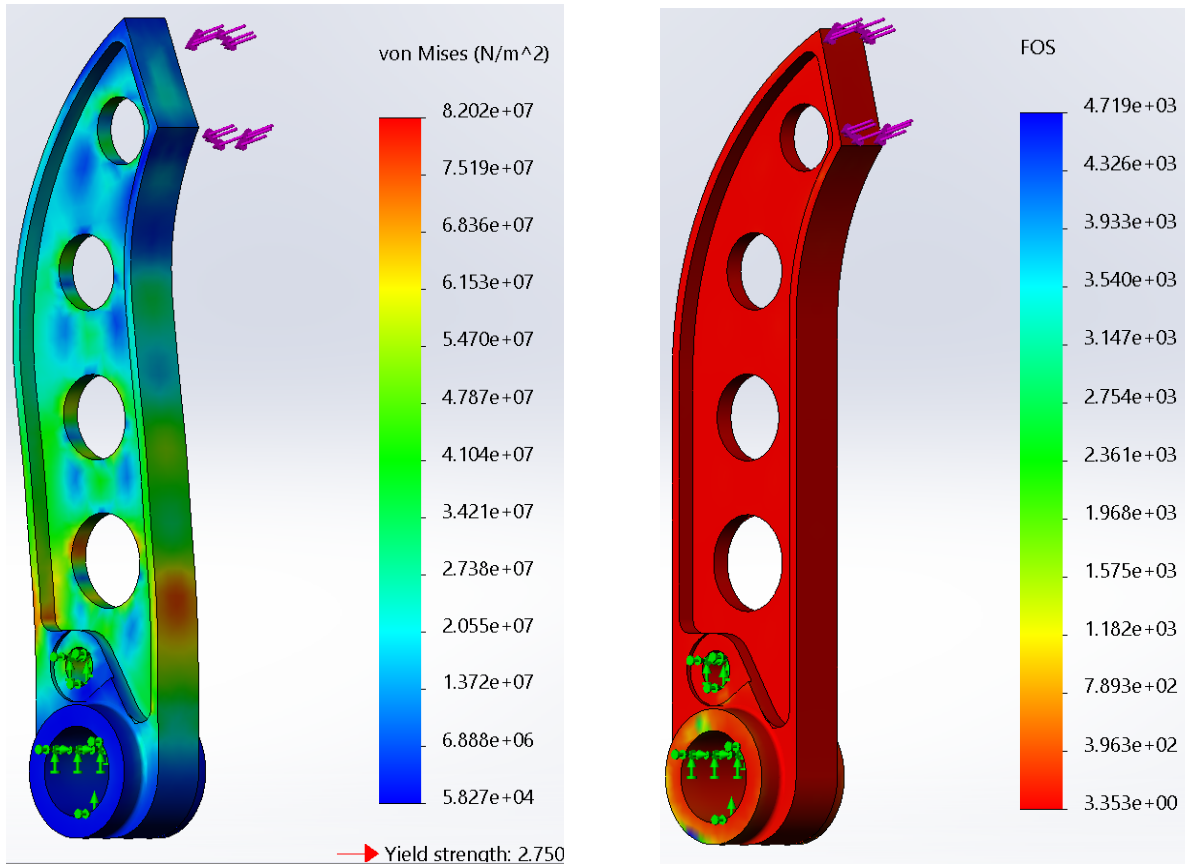
Figure 144: *SolidWorks Simulation results of brake pedal undergoing 2000N of force.*

Through the redesign of the brake assembly, significant weight savings were achieved. The weight of the assembly, bias bar and master cylinder excluded, was reduced from 4.87 lbs to 3.86 lbs.
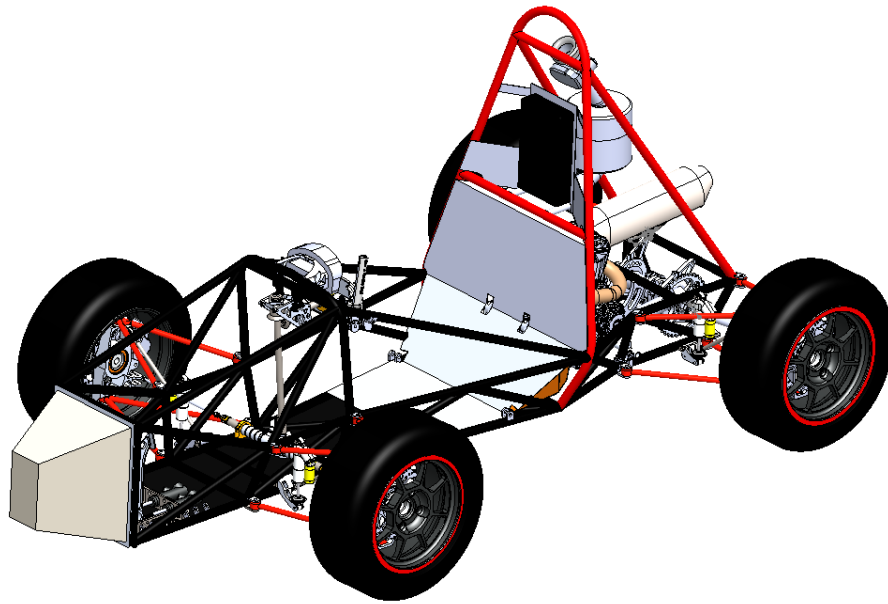
Ergonomics
Firewall, Headrest, and Floor

Figure 145: *Isometric view of the firewall, headrest, and floor mounted in the frame.*

The firewall is constructed from 0.081" 5052 sheets. It stretches from the top of the roll hoop to the bottom of the gas tank This will protect the driver from any malfunctions in the engine bay. It will also serve as a seat backing and a mount for the engine control unit (ECU). The headrest keeps the driver from experiencing whiplash in the event of a crash. It is located at the top of the firewall and holds the driver's head in a comfortable position for driving. If the car were to roll, the headrest will sit 8" above the ground per the rules, ensuring the safety of the driver. The headrest support this year has been reinforced when compared to last year's design. The same two cantilever tubes provide backing, but there is now a flat metal bar that wraps around the back and further supports the backing. This brings the backing out of a cantilever configuration, as seen in Figure 146. This allows the the headrest support to not flex as much when undergoing stresses. To test the strength of the new supports, FEA in SolidWorks was used. The results of this simulation can be seen in Figure 148. The force applied was 890N as specified by rule T.4.7.5 from the 2019 competition rulebook.
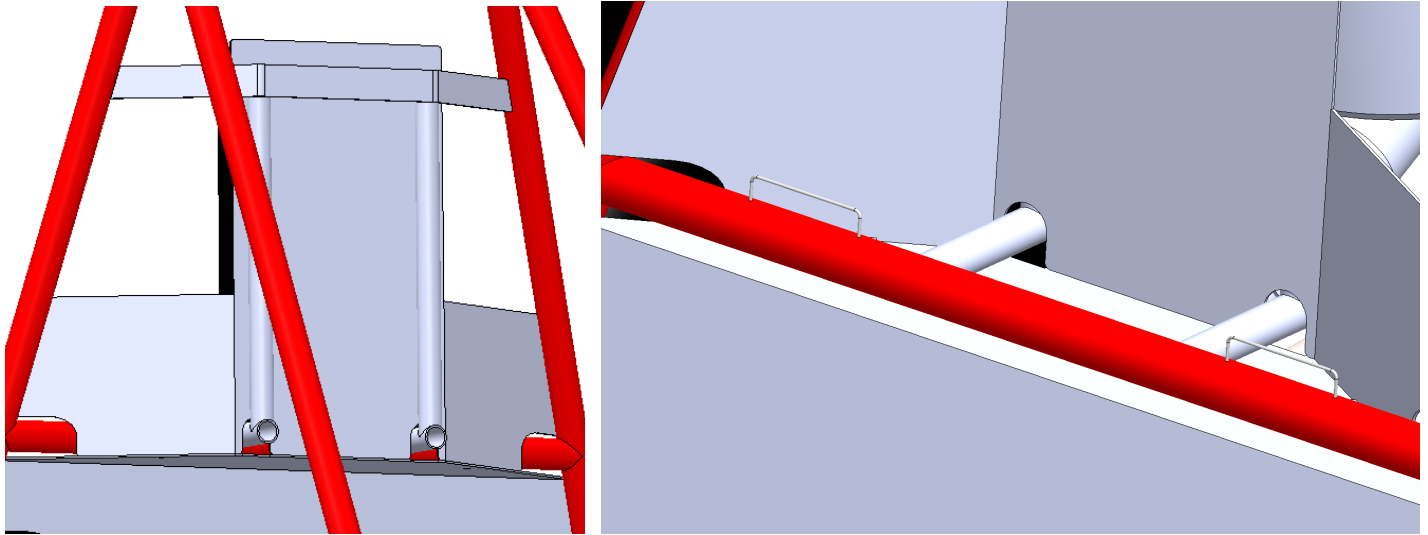
Figure 146: *Firewall, harness guard, headrest supports, and harness shoulder restraint mount.*
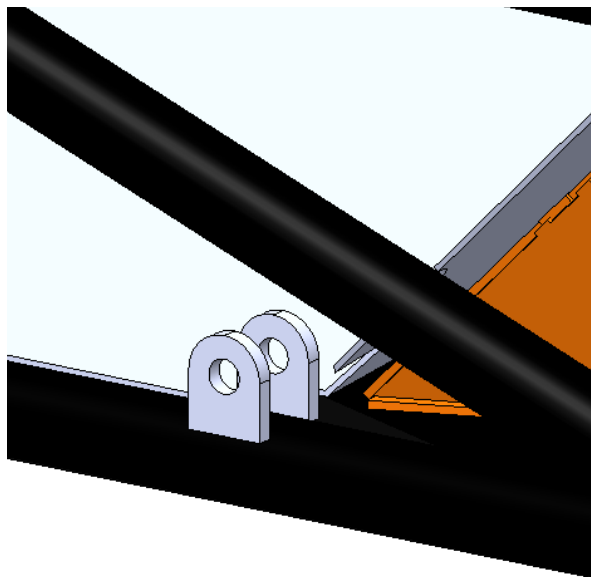
Figure 147: *Seat belt tabs.*
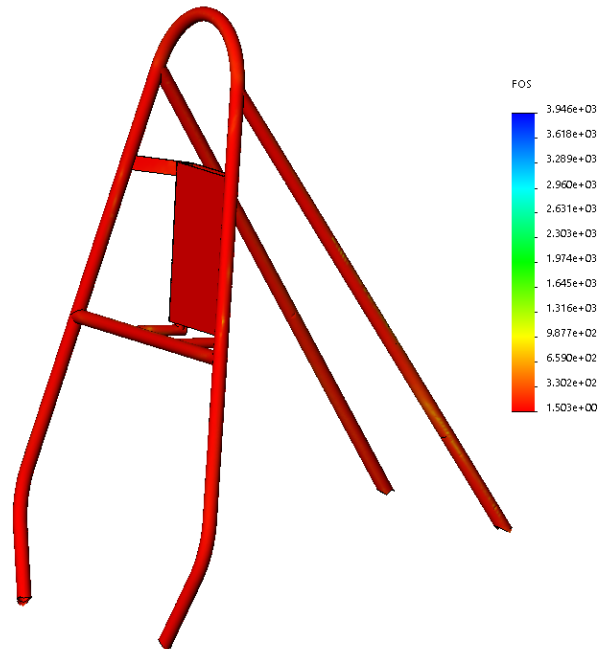
Figure 148: *FEA of headrest under 890N of force.*

The floor will be made entirely from carbon fiber. Last year, the firewall extended below the seat to the front roll hoop and acted as the floor for that section. The floor was then carbon fiber to the front of the car. By having the floor entirely made of carbon fiber it will save weight.

Seat

Seat ergonomics was chosen to be looked into further for the 2019 car. Discussing with Dr.Freed, who has extensive experience with seat design, our team was able to create a layout of what defines good ergonomics, and gathered information on what the optimal design for a race seat is.

The most detrimental design mistake other teams, and even professional race seat manufacturers, make is the angle positioning of a driver's thighs to back. Preferably, the thigh to back angle should be around 110 degrees, yet most seat manufacturers fail to achieve this and use an angle of 90-100 degrees, as seen in Figure 149.
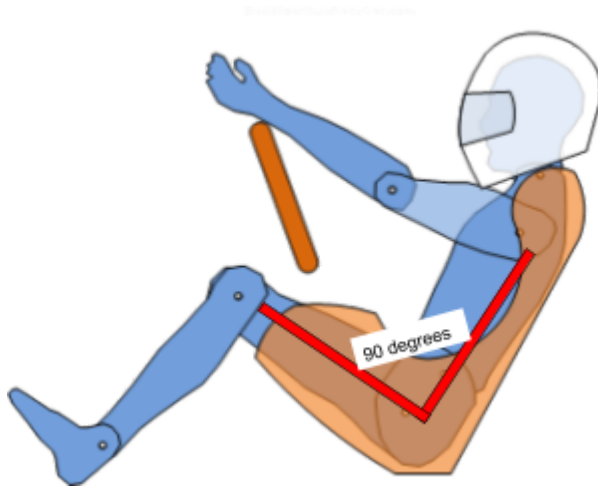
Figure 149: *Bad seating position.*

Figure 150: *JEGS seat.*

After searching for a seat that fit our criteria of this, it was chosen to be a JEGS 70200 Pro High Back Race Seat, Figure 150.

The seat back decline is at 17 degrees, but although this fit our criteria, at 13lbs this seat was too heavy for our car. Instead, utilizing the hollow seat to our advantage, the seat was cut along its mold seems to be used as a mold for our new seat, which utilizes expanding foam for weight reduction. Figure 151 shows the proper pre-foam pour orientation of the seat.

Figure 151: *Correct seating position for current car.*

Utilizing this position, expanding foam was poured within a plastic retaining bag, limited from width expansion by the surrounding frame, to mold to the shape of the seat and car. Post pour and some minor shaping can be seen in Figure 152

Figure 152: *Post foam pour seat shape.*

Figure 153: *Finalized shape of seat.*

The seat required much more shaping, filling, and smoothing before being considered complete. Figure 153 shows the finalized shaping of the seat. Once shaped correctly, the seat was sent out to be upholstered by SoundSensation. This finished seat, shown in Figure 154, maximizes driver comfort and reduces fatigue that would otherwise be caused by improper seating positions during competition racing.


Figure 154: *Final Seat*

Bibliography

1. Fatigue-life curve-4130 Steel. (2016, March 16).

2. Giang, B. (2017, July 1). MUR Blog - Differentials…What's The Difference? (Pt. 2). Retrieved from file:///Y:/2019 Car Files/Engine-Powertrain/Differential/MUR Blog - Differentials…What's The Difference_ (Pt. 2) _ MUR Motorsports.html

3. Norton, R. L., & Higgins, M. P. (2014). *Machine design: An integrated approach*. Boston: Prentice Hall.

4. Koch, P. (2008). Equivalent diameters of rectangular and oval ducts. *Building Services Engineering Research and Technology, 29*(4), 341-347. doi:10.1177/0143624408094631

5. Bell, A. G. (1991). *Performance Tuning in Theory and Practice: Four Strokes*. Sparkford, Yeovil, Somerset, England: Haynes.

6. Suspension. (n.d.). Retrieved October 29, 2017, from https://www.formula1.com/en/championship/inside-f1/understanding-f1-racing/Suspension.html

7. Kasprzak, J. (n.d.). Understanding your Dampers. Retrieved September 16, 2017, from http://www.kaztechnologies.com/wp-content/uploads/2014/03/A-Guide-To-Your-Dampers-Chapter-from-FSAE-Book-by-Jim-Kasprzak.pdf

8. Giaraffa, M. (n.d.). Tech Tip: Springs & Dampers, Part One - OptimumG. Retrieved from http://www.optimumg.com/docs/Springs&Dampers_Tech_Tip_1.pdf

9. Chegg.com. (n.d.). Retrieved from https://www.chegg.com/homework-help/questions-and-answers/half-car-model-shown--find-equations-describe-dynamic-response-vehicle-mode-shapes-frequen-q13009533

10. Roll Center Understood. (n.d.). Retrieved from http://thecartech.com/subjects/auto_eng2/Roll_Center.htm

11. Wheel Alignment Explained - What is camber, caster and toe? (2015, March 27). Retrieved from http://yospeed.com/wheel-alignment-explained-camber-caster-toe/

12. Ganz, S. (n.d.). Simple Tire Camber Examples. Retrieved from http://www.gtsparkplugs.com/wheel-camber-examples.html

13. LaFrance, A. (n.d.). Learn Camber, Caster, and Toe | Suspension Alignments. Retrieved from https://www.comeanddriveit.com/suspension/camber-caster-toe

14. Positive and Negative Camber Effects in Your Car. (2017, December 21). Retrieved from https://oards.com/positive-and-negative-camber-effects/

15. TIRE TECH: ALIGNMENT. (n.d.). Retrieved from
    https://www.tirerack.com/tires/tiretech/techpage.jsp?techid=4

16. Suspension design: Definitions and effects on vehicle behavior. (2015, April 18). Retrieved from
    http://www.car-engineer.com/suspension-design-definitions-and-effects-on-vehicle-behavior/

17. Car Suspension Basics, How-To & Design Tips ~ FREE! (n.d.). Retrieved from
    https://www.buildyourownracecar.com/race-car-suspension-basics-and-design/3/

18. Smith, C. (1999). *Tune to win*. Redwood City, CA: Motorbooks International.

19. E85 (Flex Fuel). (n.d.). Retrieved from https://afdc.energy.gov/fuels/ethanol_e85.html

20. Scheme-it – Schematic Drawing and Block Diagramming. (n.d.). Retrieved from
    https://www.digikey.com/en/resources/design-tools/schemeit

21. EXP Technology. (n.d.). Retrieved from https://rekluse.com/product/exp-technology/

22. Hose Ends at Summit Racing. (n.d.). Retrieved from
    https://www.summitracing.com/search/department/fittings-hoses/part-type/hose-ends/?GroupBy=Produc
    tName&GridPageSize=20&SortBy=Default&SortOrder=Ascending&cm_mmc=ppc-google-_-search-_-
    general-terms-_-keyword

23. Everything you need to know about the 2018 Suzuki RM-Z450. (2018, February 24). Retrieved from
    https://motocrossactionmag.com/first-look-2018-suzuki-rm-z450-2/

24. How to calculate the volumetric efficiency of an internal combustion engine. (n.d.). Retrieved from
    https://x-engineer.org/automotive-engineering/internal-combustion-engines/performance/calculate-volu
    metric-efficiency

25. Haltech ESP (Version 2.39.01). (n.d.). Retrieved from https://www.haltech.com/

26. O. (2000). Choked Flow of Gases. Retrieved from Choked Flow of Gases

Appendix A: Frame FEA

Name	Force	Min FOS	Max FOS
Front Impact Factor of Safety	14750N	1.338e+00 Node: 471	1.000e+16 Node: 20

Frame_9.19.18_FEA-front impact-Factor of Safety-Factor of Safety1
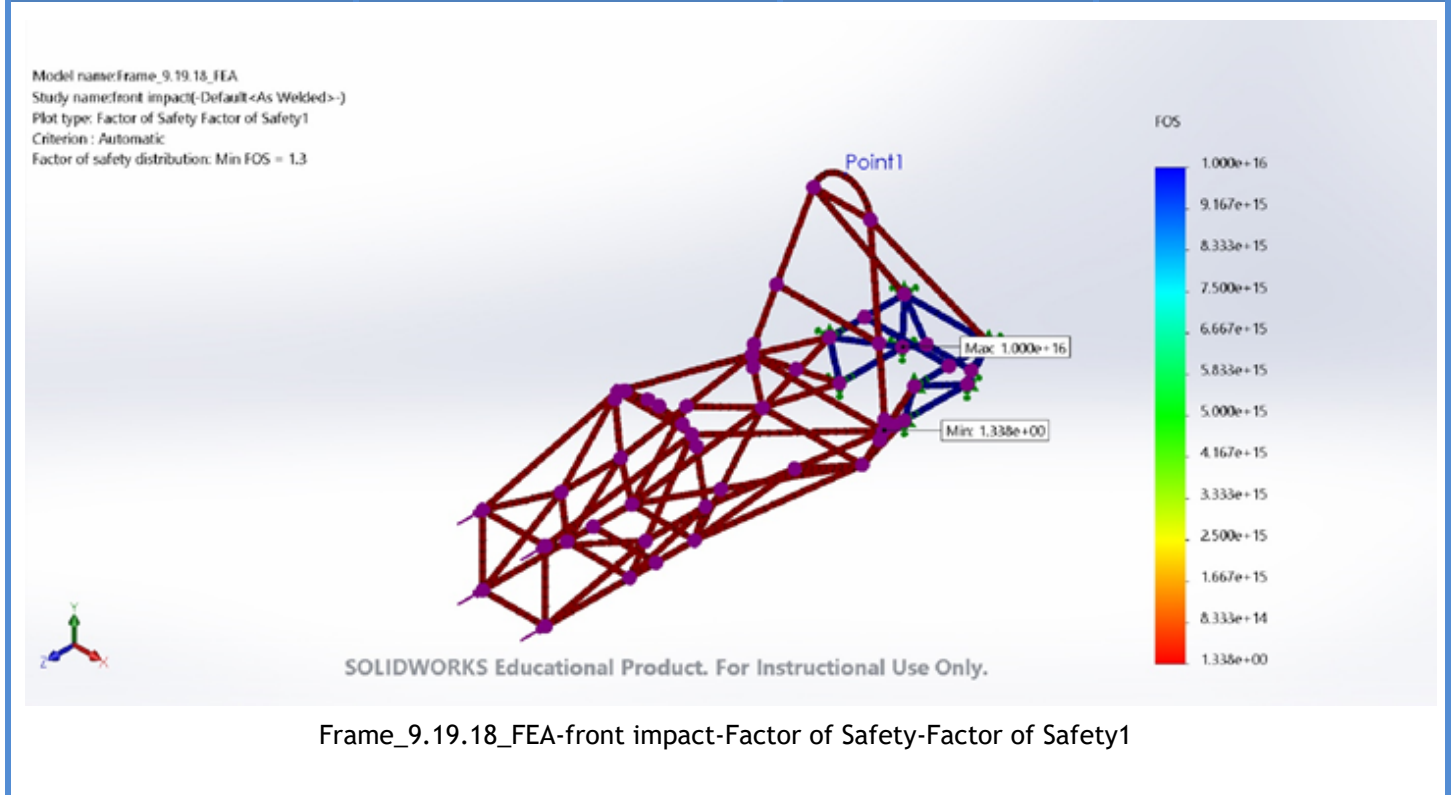
Name	Moment	Min	Max
Torsional Rigidity Torque per degree	1500Nm	-1.797e-03deg Node: 248	1.027e+00 deg Node: 296

Frame_9.19.18_FEA-Torsional Rigidity-Displacement-Displacement2
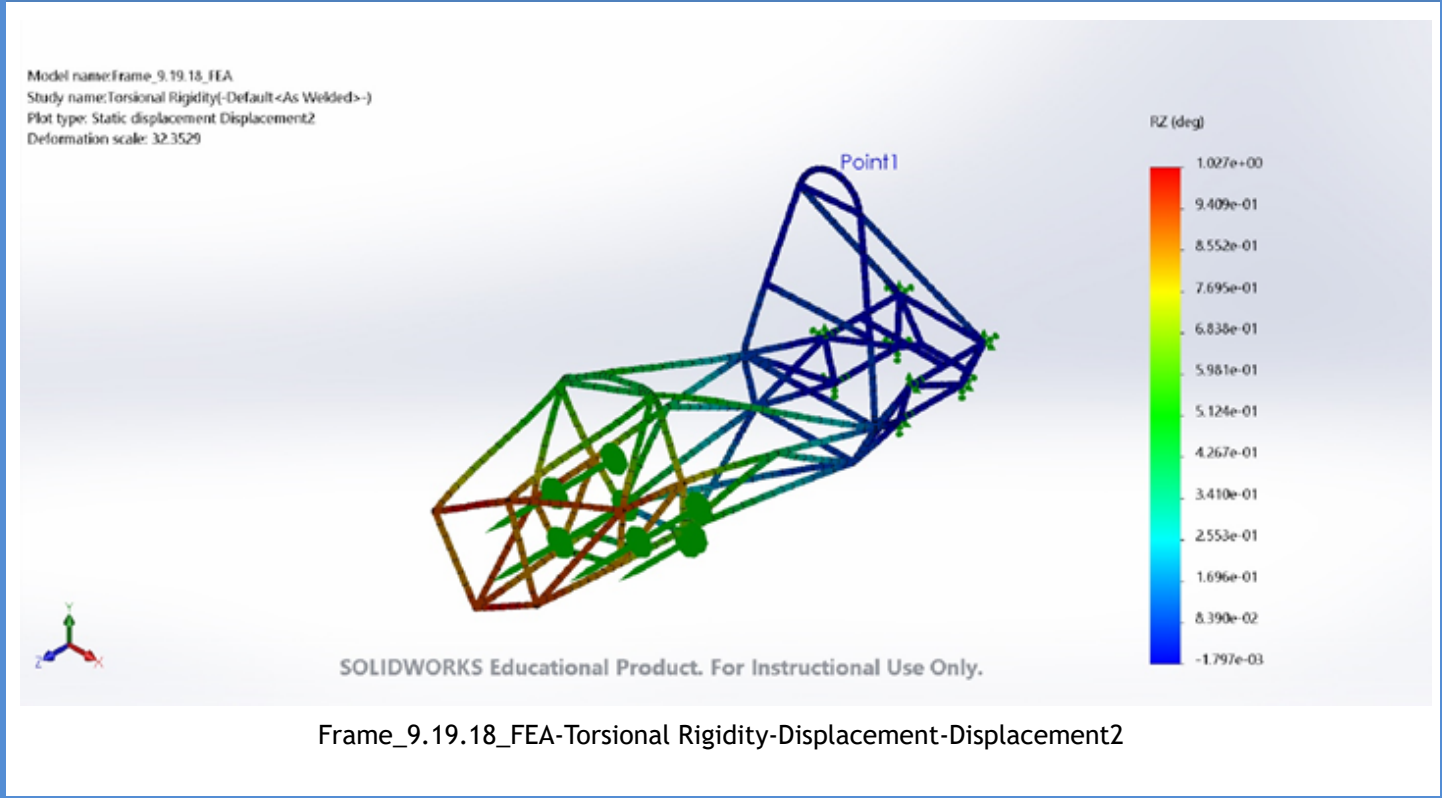
Name	Force	Min	Max
Side Impact Factor of Safety	1750N	1.531e+00 Node: 49	1.000e+16 Node: 20

Frame_9.19.18_FEA-Side Impact-Factor of Safety-Factor of Safety1
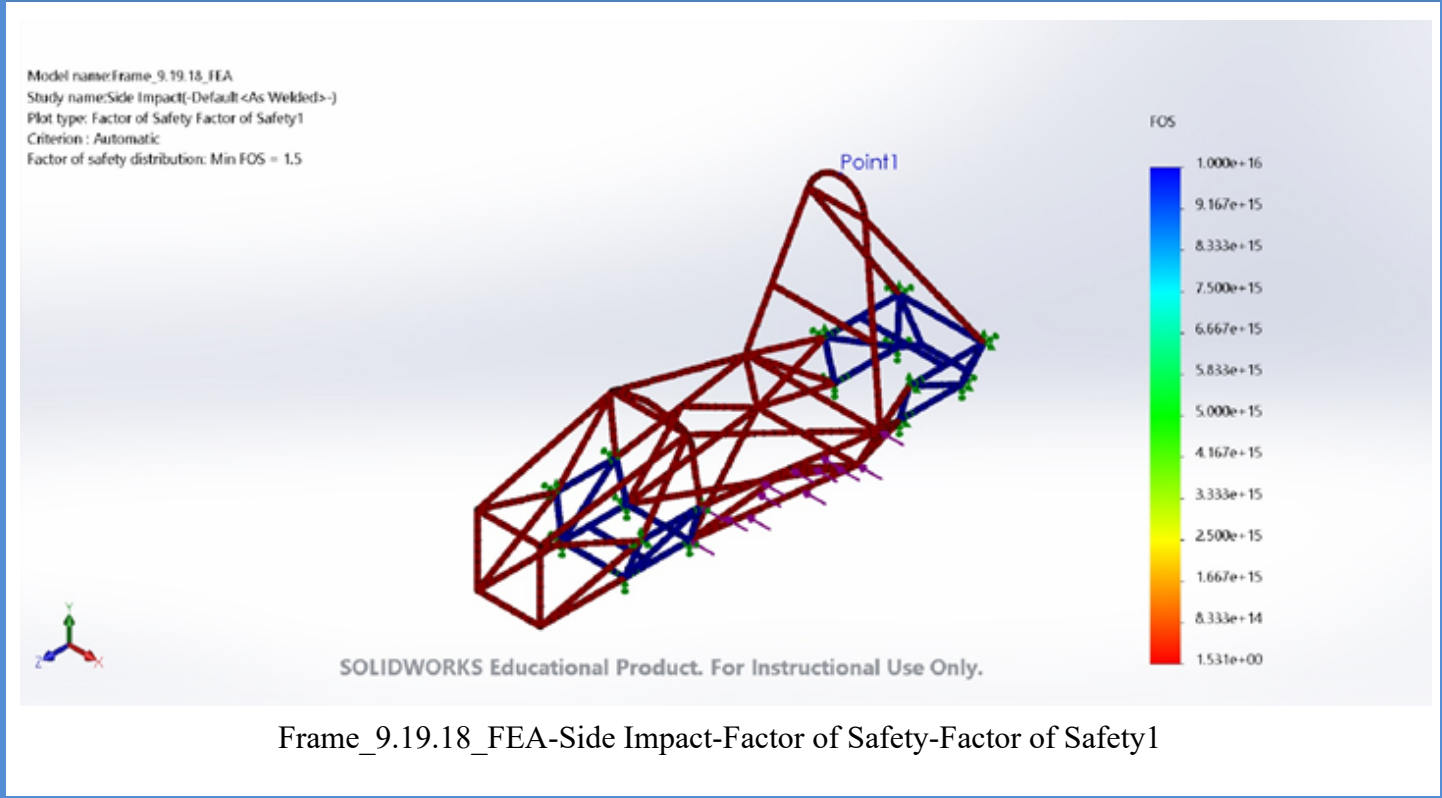
Name	Force	Min	Max
Main Roll Hoop Factor of Safety1	6000N	2.711e+00 Node: 624	1.000e+16 Node: 20

Frame_9.19.18_FEA-Main Roll Hoop-Factor of Safety-Factor of Safety1

Name	Force	Min	Max
Front Roll Hoop Factor of Safety	6000N	2.210e+00 Node: 426	1.000e+16 Node: 20

Frame_9.19.18_FEA-Front Roll Hoop-Factor of Safety-Factor of Safety1

Appendix B: Control Arm Tab Von Mises Stress Calculations and Safety Factors

Geometric Properties

$l := 1.16\text{in}$

$w := 0.875\text{in}$

$h := 0.1875\text{in}$

$A := w \cdot h \qquad c_y := \dfrac{w}{2}$

$I_{yy} := \dfrac{w \cdot h^3}{12} = 2.001 \times 10^{-10}\ \text{m}^4$

$I_{zz} := \dfrac{h \cdot w^3}{12} = 4.357 \times 10^{-9}\ \text{m}^4$

Material Properties: 4130 Chromalloy

$S_{ut} := 97200\text{psi}$

$E := 29700\text{ksi}$

$S_y := 63100\text{psi}$

Environment $\qquad T_{op} := 120$

Forces on Tab

Force from Braking: $\qquad F_B := 375\text{lbf}$

$M_B := F_B \cdot l$

Force from Acceleration: $\qquad F_A := 250\text{lbf}$

$M_A := F_A \cdot l$

Force from Turning: $\qquad F_{Ti} := 375\text{lbf}$

$F_{To} := 375\text{lbf}$

Buckling Analysis: Force from Turning In

Assumed as cantilever beam with force acting on centroid

$F_{crit} := \dfrac{\pi^2 \cdot E \cdot I_{yy}}{4 \cdot l^2} = 2.618 \times 10^4 \cdot \text{lbf}$

$\dfrac{F_{crit}}{F_{Ti}} = 69.804$

Static Bending Failure: Acceleration and Turning In

$$\sigma_{AIx} := \frac{F_{Ti}}{A} = 2.286 \times 10^3 \cdot psi \qquad \tau_{xz} := 0psi$$

$$\sigma_{AIy} := \frac{M_A \cdot c_y}{I_{zz}} = 1.212 \times 10^4 \cdot psi$$

$$\tau_{AImax} := \sqrt{\left(\frac{\sigma_{AIx} - \sigma_{AIy}}{2}\right)^2 + \tau_{xz}^2} = 4.918 \times 10^3 \cdot psi$$

$$\sigma_{AI1} := \frac{\sigma_{AIx} + \sigma_{AIy}}{2} + \tau_{AImax} = 1.212 \times 10^4 \cdot psi$$

$$\sigma_{AI3} := \frac{\sigma_{AIx} + \sigma_{AIy}}{2} - \tau_{AImax} = 2.286 \times 10^3 \cdot psi$$

$$\sigma_{AIvm} := \sqrt{\sigma_{AI1}^2 - \sigma_{AI1} \cdot \sigma_{AI3} + \sigma_{AI3}^2} = 1.115 \times 10^4 \cdot psi$$

Safety Factors: Von Mises and Shear

$$N_{AIvm} := \frac{S_y}{\sigma_{AIvm}} = 5.657 \qquad N_{AIs} := \frac{0.5 \cdot S_y}{\tau_{AImax}} = 6.416$$

Static Bending Failure: Acceleration and Turning Out

$$\sigma_{AOx} := \frac{-F_{To}}{A} = -2.286 \times 10^3 \cdot psi \qquad \tau_{xz} := 0psi$$

$$\sigma_{AOy} := \frac{M_A \cdot c_y}{I_{zz}} = 1.212 \times 10^4 \cdot psi$$

$$\tau_{AOmax} := \sqrt{\left(\frac{\sigma_{AOx} - \sigma_{AOy}}{2}\right)^2 + \tau_{xz}^2} = 7.203 \times 10^3 \cdot psi$$

$$\sigma_{AO1} := \frac{\sigma_{AOx} + \sigma_{AOy}}{2} + \tau_{AOmax} = 1.212 \times 10^4 \cdot psi$$

$$\sigma_{AO3} := \frac{\sigma_{AOx} + \sigma_{AOy}}{2} - \tau_{AOmax} = -2.286 \times 10^3 \cdot psi$$

$$\sigma_{AOvm} := \sqrt{\sigma_{AO1}^2 - \sigma_{AO1} \cdot \sigma_{AO3} + \sigma_{AO3}^2} = 1.341 \times 10^4 \cdot psi$$

Safety Factors: Von Mises and Shear

$$N_{AOvm} := \frac{S_y}{\sigma_{AOvm}} = 4.705 \qquad N_{AOs} := \frac{0.5 \cdot S_y}{\tau_{AOmax}} = 4.38$$

Static Bending Failure: Braking and Turning In

$$\sigma_{BIx} := \frac{F_{Ti}}{A} = 2.286 \times 10^3 \cdot psi \qquad \tau_{xz} := 0psi$$

$$\sigma_{BIy} := \frac{M_B \cdot c_y}{I_{zz}} = 1.818 \times 10^4 \cdot psi$$

$$\tau_{BImax} := \sqrt{\left(\frac{\sigma_{BIx} - \sigma_{BIy}}{2}\right)^2 + \tau_{xz}^2} = 7.948 \times 10^3 \cdot psi$$

$$\sigma_{BI1} := \frac{\sigma_{BIx} + \sigma_{BIy}}{2} + \tau_{BImax} = 1.818 \times 10^4 \cdot psi$$

$$\sigma_{BI3} := \frac{\sigma_{BIx} + \sigma_{BIy}}{2} - \tau_{BImax} = 2.286 \times 10^3 \cdot psi$$

$$\sigma_{BIvm} := \sqrt{\sigma_{BI1}^2 - \sigma_{BI1} \cdot \sigma_{BI3} + \sigma_{BI3}^2} = 1.715 \times 10^4 \cdot psi$$

Safety Factors: Von Mises and Shear

$$N_{BIvm} := \frac{S_y}{\sigma_{BIvm}} = 3.679 \qquad N_{BIs} := \frac{0.5 \cdot S_y}{\tau_{BImax}} = 3.97$$

Static Bending Failure: Braking and Turning Out

$$\sigma_{BOx} := \frac{-F_{To}}{A} = -2.286 \times 10^3 \cdot psi \qquad \tau_{xz} := 0 psi$$

$$\sigma_{BOy} := \frac{M_B \cdot c_y}{I_{zz}} = 1.818 \times 10^4 \cdot psi$$

$$\tau_{BOmax} := \sqrt{\left(\frac{\sigma_{BOx} - \sigma_{BOy}}{2}\right)^2 + \tau_{xz}^2} = 1.023 \times 10^4 \cdot psi$$

$$\sigma_{BO1} := \frac{\sigma_{BOx} + \sigma_{BOy}}{2} + \tau_{BImax} = 1.59 \times 10^4 \cdot psi$$

$$\sigma_{BO3} := \frac{\sigma_{BOx} + \sigma_{BOy}}{2} - \tau_{BOmax} = -2.286 \times 10^3 \cdot psi$$

$$\sigma_{BOvm} := \sqrt{\sigma_{BO1}^2 - \sigma_{BO1} \cdot \sigma_{BO3} + \sigma_{BO3}^2} = 1.715 \times 10^4 \cdot psi$$

Safety Factors: Von Mises and Shear

$$N_{BOvm} := \frac{S_y}{\sigma_{BOvm}} = 3.679 \qquad N_{BOs} := \frac{0.5 \cdot S_y}{\tau_{BOmax}} = 3.083$$

Pin Tear Out May Occur When Turning Out

$$R_1 := \frac{0.375}{2} in$$

$$R_2 := 0.4375 in$$

$$P_T := \frac{F_{To}}{2 \cdot R_1 \cdot h} = 5.333 \times 10^3 \cdot psi$$

$$\tau_T := \frac{P_T}{2} = 2.667 \times 10^3 \cdot psi$$

$$N_T := \frac{0.5 \cdot S_y}{\tau_T} = 11.831$$

Fluctuating Forces: Acceleration and Braking

$$F_{Amin} := F_A$$

$$F_{Amax} := -F_B$$

$$F_{Aavg} := \frac{F_{Amax} - F_{Amin}}{2}$$

$$M_{Amax} := F_{Amax} \cdot l$$

$$M_{Amin} := F_{Amin} \cdot l$$

$$M_{Aavg} := F_{Aavg} \cdot l$$

$$\sigma_{Axavg} := \frac{M_{Aavg} \cdot c_y}{I_{zz}} = -1.515 \times 10^4 \cdot psi \qquad \sigma_{Ayavg} := 0psi \qquad \tau_{Axyavg} := 0psi$$

$$\sigma_{Axmin} := \frac{M_{Amin} \cdot c_y}{I_{zz}} = 1.212 \times 10^4 \cdot psi \qquad \sigma_{Aymin} := 0psi \qquad \tau_{Axymin} := 0psi$$

$$\sigma_{Axmax} := \frac{M_{Amax} \cdot c_y}{I_{zz}} = -1.818 \times 10^4 \cdot psi \qquad \sigma_{Aymax} := 0psi \qquad \tau_{Axymax} := 0psi$$

$$\sigma_{Avmavg} := \sqrt{\sigma_{Axavg}^2 + \sigma_{Ayavg}^2 - \sigma_{Axavg} \cdot \sigma_{Ayavg} + 3\tau_{Axyavg}} = 1.515 \times 10^4 \cdot psi$$

$$\sigma_{Avmmin} := \sqrt{\sigma_{Axmin}^2 + \sigma_{Aymin}^2 - \sigma_{Axmin} \cdot \sigma_{Aymin} + 3\tau_{Axymin}} = 1.212 \times 10^4 \cdot psi$$

Load:

1 if Bending
0.7 if Axial

$$C_{load} := 1$$

Size

$$A_{95} := 0.05 \cdot h \cdot w = 8.203 \times 10^{-3} \cdot in^2$$

$$d_{equiv} := \sqrt{\frac{A_{95}}{0.0766}} = 0.327 \cdot in$$

$$C_{size} := \begin{vmatrix} 1 & \text{if } d_{equiv} \le 8 \\ 1.189 \cdot d_{equiv}^{-0.097} & \text{if } 8 < d_{equiv} \le 250 \end{vmatrix}$$

$$C_{size} = 1$$

Surface

Machined:

$$A_{surf} := 2.7$$

$$b_{surf} := -0.265$$

$$C_{surf} := A_{surf} \cdot S_{ut}^{b_{surf}}$$

$$C_{surf} = 0.803$$

Temperature

$$C_{temp} := \begin{vmatrix} 1 & \text{if } T_{op} \le 450 \\ \left[1 - 0.0058 \cdot \left(T_{op} - 450\right)\right] & \text{if } 450 < T_{op} \le 550 \end{vmatrix}$$

$$C_{temp} = 1$$

Reliability

reliability := 99.99

$$C_{reliab} := \begin{cases} 1.000 & \text{if reliability} = 50 \\ 0.897 & \text{if reliability} = 90 \\ 0.868 & \text{if reliability} = 95 \\ 0.814 & \text{if reliability} = 99 \\ 0.753 & \text{if reliability} = 99.9 \\ 0.702 & \text{if reliability} = 99.99 \\ 0.659 & \text{if reliability} = 99.999 \\ 0.620 & \text{if reliability} = 99.9999 \end{cases}$$

$$S_{e1} := S_{ut} \cdot 0.5 = 4.86 \times 10^4 \cdot psi$$

$$S_e := C_{load} \cdot C_{size} \cdot C_{surf} \cdot C_{temp} \cdot C_{reliab} \cdot S_{e1}$$

$$S_e = 2.739 \times 10^4 \cdot psi$$

$$N_1 := \frac{S_y \cdot \left(1 - \dfrac{\sigma_{Avmmin}}{S_{ut}}\right)}{\sigma_{Avmavg}} = 3.645$$

$$N_2 := \frac{S_e \cdot \left(1 - \dfrac{\sigma_{Avmmin}}{S_{ut}}\right)}{\sigma_{Avmavg}} = 1.582$$

$$N_3 := \frac{S_e \cdot S_{ut}}{\sigma_{Avmavg} \cdot S_{ut} + \sigma_{Avmmin} \cdot S_e} = 1.475$$

$$N_4 := \frac{OZ + ZS}{OZ} = 1.438$$

Fluctuating Forces: Turning In and Out

$$F_{max} := F_{To}$$

$$F_{min} := -F_{Ti}$$

$$F_T := F_{To}$$

$$F_T := \left| -F_{Ti} \right|$$

$$\sigma_{Tx} := \frac{F_T}{A} = 2.286 \times 10^3 \cdot psi$$

$$\tau_{Tmax} := \sqrt{\left(\frac{\sigma_{Tx}}{2}\right)^2} = 1.143 \times 10^3 \cdot psi$$

$$\sigma_{T1} := \frac{\sigma_{Tx}}{2} + \tau_{Tmax}$$

$$\sigma_{Tvm} := \sqrt{\sigma_{T1}^2} = 2.286 \times 10^3 \cdot psi$$

$$S_{e1} = 4.86 \times 10^4 \cdot psi$$

Load:

1 if Bending
0.7 if Axial

$$C_{load} := .7$$

Size

$$A_{95} := 0.05 \cdot h \cdot w = 8.203 \times 10^{-3} \cdot in^2$$

$$d_{equiv} := \sqrt{\frac{A_{95}}{0.0766}} = 0.327 \cdot in$$

$$C_{size} := \begin{vmatrix} 1 & \text{if } d_{equiv} \le 8 \\ 1.189 \cdot d_{equiv}^{-0.097} & \text{if } 8 < d_{equiv} \le 250 \end{vmatrix}$$

$$C_{size} = 1$$

Surface

Machined:

$$A_{surf} := 2.7$$

$$b_{surf} := -0.265$$

$$C_{surf} := A_{surf} \cdot S_{ut}^{b_{surf}}$$

$$C_{surf} = 0.803$$

Temperature

$$C_{temp} := \begin{vmatrix} 1 & \text{if } T_{op} \le 450 \\ \left[1 - 0.0058 \cdot \left(T_{op} - 450\right)\right] & \text{if } 450 < T_{op} \le 550 \end{vmatrix}$$

$$C_{temp} = 1$$

Reliability

$\text{reliability} := 99.99$

$$C_{reliab} := \begin{cases} 1.000 & \text{if } \text{reliability} = 50 \\ 0.897 & \text{if } \text{reliability} = 90 \\ 0.868 & \text{if } \text{reliability} = 95 \\ 0.814 & \text{if } \text{reliability} = 99 \\ 0.753 & \text{if } \text{reliability} = 99.9 \\ 0.702 & \text{if } \text{reliability} = 99.99 \\ 0.659 & \text{if } \text{reliability} = 99.999 \\ 0.620 & \text{if } \text{reliability} = 99.9999 \end{cases}$$

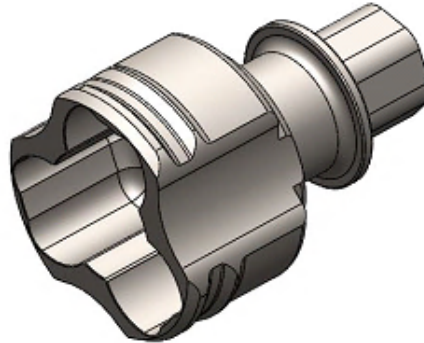$S_e := C_{load} \cdot C_{size} \cdot C_{surf} \cdot C_{temp} \cdot C_{reliab} \cdot S_{e1}$

$S_e = 1.917 \times 10^4 \cdot \text{psi}$

$N := \dfrac{S_e}{\sigma_{Tvm}}$

$N = 8.388$

Appendix C: Axle Housing Von Mises Stress Calculations and Safety Factors

Axle Flange test

Car Specification:

$m := 250\text{kg}$ mass of car

$\mu := 1.5$ Assumed tire coefficient of friction

$d_t := 20.5\text{in}$ Diameter of tire

$d_t = 0.521\,\text{m}$

$R_{1st} := 2.417$ Gear ratio - first gear

$R_p := 2.652$ Gear Ratio - Primary gear ratio

$R_f := 3$ Gear Ratio - Final drive, sprocket combination

$R_t := R_{1st} \cdot R_p \cdot R_f = 19.23$ Final Gear ratio

$T_s := 33\text{lbf} \cdot \text{ft}$ Measured torque from a stock 2018 WR450F dyno chart

1) Calculate Axle torque

Method 1: use maximum force of friction and tire as a lever arm

$F_n := m \cdot g = 2451.662\,\text{N}$

$F_f := F_n \cdot \mu = 3677.494\,\text{N}$

$T_{w1} := \left(\dfrac{d_t}{2}\right) \cdot F_f = 957.435 \cdot \text{J}$

$T_{w1} = 706.168 \cdot \text{lbf} \cdot \text{ft}$ Total wheel torque - for 2 wheels

$T_{axle1} := \dfrac{T_{w1}}{2} = 353.084 \cdot \text{lbf} \cdot \text{ft}$

$+$
Method 2: use stock bike torque value and gear ratio

$T_{w2} := T_s \cdot R_t = 860.373\,\text{J}$ Wheel torque

$T_{axle2} := \dfrac{T_{w2}}{2} = 317.289 \cdot \text{lbf} \cdot \text{ft}$

Using higher calculated value and a factor of safety of 1.5 the final axle torque is,

$$T_{axle} := T_{axle1} \cdot 1.5 = 529.626 \cdot lbf \cdot ft$$

$$T_{axle} = 529.626 \cdot lbf \cdot ft$$

2) Location of critical sections

Assumptions :

- The larger section of the part (from x = 0 to x = a) is not adjustable and will be constrained to the given dimensions. The critical section from x = a to x = b+c is to be found.

- The only load on the part is the axle torque.

- The area d is considered fixed to the hub, therfore the part is assumed fixed at the start of position d.
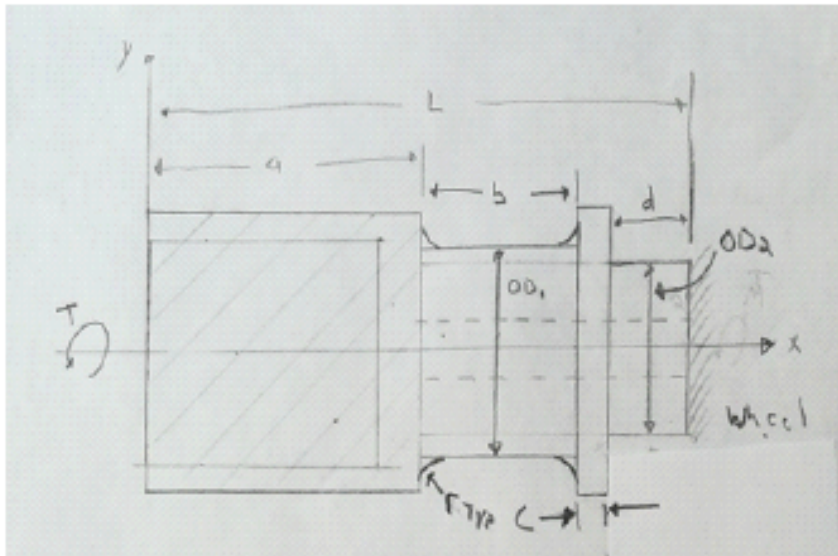
Part Dimensions: Units in inches

L := 4.29in	D_1 := 2.657in	R_1 := .3in
a := 1.57in	D_2 := 1.3in	R_2 := .25in
b := 1.545in	D_f := 2.2in	
c := .15in	D_3 := 1.219in	The red line displays the section being tested
d := .995in	D_{in} := .625in	

FIGURE C-3

Geometric Stress-Concentration Factor K_t for a Shaft with a Shoulder Fillet in Torsion

$$K_t \cong A\left(\frac{r}{d}\right)^b$$

where:

D/d	A	b
2.00	0.863 31	−0.238 65
1.33	0.848 97	−0.231 61
1.20	0.834 25	−0.216 49
1.09	0.903 37	−0.126 92

Stress concentration constants:

Using cubic interpolation to find the constants A and b . From the table and equation in Figure C-3,

$$CA := \begin{pmatrix} 1 & 1.09 & 1.09^2 & 1.09^3 \\ 1 & 1.2 & 1.2^2 & 1.2^3 \\ 1 & 1.33 & 1.33^2 & 1.33^3 \\ 1 & 2.0 & 2.0^2 & 2.0^3 \end{pmatrix}^{-1} \cdot \begin{pmatrix} .90337 \\ 0.83425 \\ 0.84897 \\ 0.86331 \end{pmatrix} \qquad CA = \begin{pmatrix} 11.756 \\ -23.037 \\ 15.839 \\ -3.522 \end{pmatrix}$$

$$A(D') := CA_0 + CA_1 \cdot D' + CA_2 \cdot D'^2 + CA_3 \cdot D'^3$$

$$A(1.2) = 0.834 \qquad \text{test}$$

$$Cb := \begin{pmatrix} 1 & 1.09 & 1.09^2 & 1.09^3 \\ 1 & 1.2 & 1.2^2 & 1.2^3 \\ 1 & 1.33 & 1.33^2 & 1.33^3 \\ 1 & 2.0 & 2.0^2 & 2.0^3 \end{pmatrix}^{-1} \cdot \begin{pmatrix} -0.12692 \\ -0.21649 \\ -0.23161 \\ -0.23865 \end{pmatrix} \qquad Cb = \begin{pmatrix} 9.871 \\ -20.755 \\ 13.951 \\ -3.05 \end{pmatrix}$$

$$b'(D') := Cb_0 + Cb_1 \cdot D' + Cb_2 \cdot D'^2 + Cb_3 \cdot D'^3$$

$$b'(1.2) = -0.216 \qquad \text{test}$$

Critical sections:
A section will be taken at loaction a and b
maximum stress will be located on the outside surface of the part. Points A, B, C and D are equal

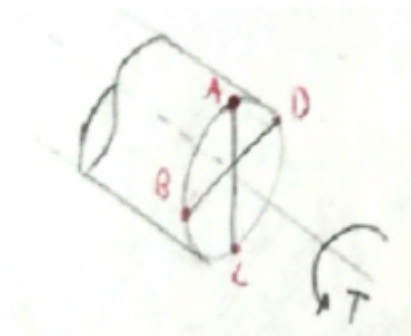Assume Pure Torsion loading - only shear stress

Section a:

$$J_{ax} := \frac{\pi \cdot D_2^4}{32} = 1.167 \times 10^{-7} \, m^4$$

$$c_a := \frac{D_2}{2} \qquad \text{Distance to outer fiber on section a}$$

$$Dda := \frac{D_1}{D_2} = 2.044$$

$$A(Dda) = 0.768$$

$$b'(Dda) = -0.316$$

$$k_t := A(Dda) \cdot \left(\frac{R_1}{D_2}\right)^{b'(Dda)} = 1.219$$

Stress consentration factor at a

$$\tau_{xza} := k_t \cdot \frac{T_{axle} \cdot c_a}{J_{ax}} = 123.854 \cdot MPa$$

Tortional shear stress - with stress consentration

$$\tau_{xza} = 17963.53 \cdot psi$$

Principal Stress at section a, point A

$$\sigma_{xa} := 0 \qquad \sigma_{ya} := 0$$

$$\sigma_{1a} := \frac{\sigma_{xa} + \sigma_{ya}}{2} + \sqrt{\left(\frac{\sigma_{xa} - \sigma_{ya}}{2}\right)^2 + \tau_{xza}^2} = 123.854 \cdot MPa$$

$$\sigma_{3a} := \frac{\sigma_{xa} + \sigma_{ya}}{2} - \sqrt{\left(\frac{\sigma_{xa} - \sigma_{ya}}{2}\right)^2 + \tau_{xza}^2} = -123.854 \cdot MPa$$

$$\sigma_{2a} := 0$$

$$\tau_{maxa} := \frac{|\sigma_{1a} - \sigma_{3a}|}{2} = 123.854 \cdot MPa$$

$$\tau_{maxa} = 17963.53 \cdot psi$$

Section b:

$$J_{bx} := \frac{\pi \cdot \left(D_2^4 - D_{in}^4\right)}{32} = 1.105 \times 10^{-7} m^4$$

$$c_b := \frac{D_2}{2}$$

Distance to outer fiber on section b

$$Ddb := \frac{D_f}{D_2} = 1.692$$

$$A(Ddb) = 1.063$$

$$b'(Ddb) = -0.083$$

$$k_{tb} := A(Ddb) \cdot \left(\frac{R_2}{D_2}\right)^{b'(Ddb)} = 1.218$$

Stress consentration factor at b

$$\tau_{xzb} := k_{tb} \cdot \frac{T_{axle} \cdot c_b}{J_{bx}} = 130.723 \cdot MPa \qquad \text{Tortional shear stress - with stress consentration}$$

$$\tau_{xzb} = 18959.712 \cdot psi$$

Principal Stress at section b, point A

$$\sigma_{xb} := 0 \qquad\qquad \sigma_{yb} := 0$$

$$\sigma_{1b} := \frac{\sigma_{xb} + \sigma_{yb}}{2} + \sqrt{\left(\frac{\sigma_{xb} - \sigma_{yb}}{2}\right)^2 + \tau_{xzb}^2} = 130.723 \cdot MPa$$

$$\sigma_{3b} := \frac{\sigma_{xb} + \sigma_{yb}}{2} - \sqrt{\left(\frac{\sigma_{xb} - \sigma_{yb}}{2}\right)^2 + \tau_{xzb}^2} = -130.723 \cdot MPa$$

$$\sigma_{2b} := 0$$

$$\tau_{maxb} := \frac{|\sigma_{1b} - \sigma_{3b}|}{2} = 130.723 \cdot MPa$$

$$\tau_{maxb} = 18959.712 \cdot psi$$

Von Mises Stress Calculation - Units MPa

$$1 - \quad \sigma'_b := \sqrt{\sigma_{1b}^2 - \sigma_{1b} \cdot \sigma_{3b} + \sigma_{3b}^2} = 226.418 \cdot MPa \qquad \text{Section b has a higher Von Mises stress}$$

$$\sigma'_b = 32839.184 \cdot psi$$

$$2 - \quad \sigma'_a := \sqrt{\sigma_{1a}^2 - \sigma_{1a} \cdot \sigma_{3a} + \sigma_{3a}^2} = 214.522 \cdot MPa$$

$$\sigma'_a = 31113.746 \cdot psi$$

Safety Factor: Point A

SF using distortion energy theory and max shear stress theory

Material Properties: Properties found from SolidWorks material library

4130 Normalized at 870C

$S_{ut4130} := 106022.59\text{psi}$

$S_{y4130} := 66717.36\text{psi}$

4340 Normalized

$S_{ut4340} := 160991.89\text{psi}$

$S_{y4340} := 102976.8\text{psi}$

Given :

Material   4130 Steel

Distorsion Energy Theory:

$$N_{detb} := \frac{S_{y4130}}{\sigma'_b} = 2.032$$

Maximum Shear Stress Theory:

$$S_{ys4130} := \frac{1}{2} \cdot S_{y4130}$$

$$N_{mssb} := \frac{S_{ys4130}}{\tau_{maxb}} = 1.759$$

Material   4340 Steel

Distorsion Energy Theory:

$$N_{detb} := \frac{S_{y4340}}{\sigma'_b} = 3.136 \qquad \boxed{\textbf{Part Safe}}$$

Maximum Shear Stress Theory:

$$S_{ys4340} := \frac{1}{2} \cdot S_{y4340}$$

$$N_{mssb} := \frac{S_{ys4340}}{\tau_{maxb}} = 2.716 \qquad \boxed{\textbf{Part safe}}$$

Axle Housing SolidWorks Von Mises Stress

Name	Type	Min	Max
Stress1	VON: von Mises Stress	4.188e-01 psi Node: 72	3.268e+04 psi Node: 825

F18_DT_RearhubAxleHousing_LongSplineFlange_simple-Static 1-Stress-Stress1
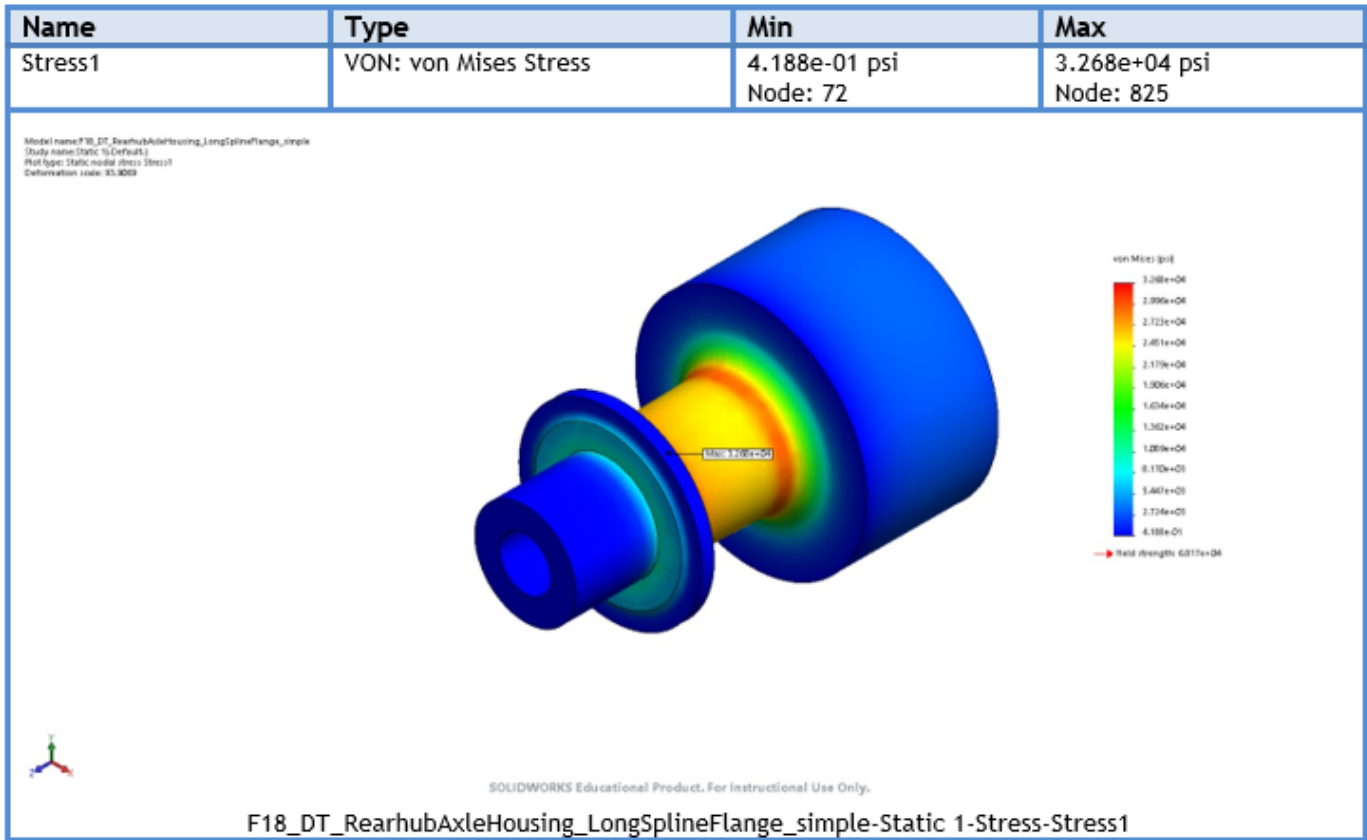
Appendix D: Suspension Bond Graph Formation and State Equations

<u>**Nomenclature**</u>

Variable	Value	Unit(s)
X, x	Displacement	m
M	Mass	kg
D	Dampening	N/(m/s)
G , g	Gravity	m/s^2
L	Length	m
V, X'	Velocity	m/s
F, P'	Force	N
P	Momentum	Kg-m/s
ω	Angular Velocity	rad/s
h',τ	Torque	N*m
K	Stiffness	N/m
h	Angular Momentum	$kg\text{-}m^2/sec$
V(t)	Input Flow	m/s

<u>**Assumptions**</u>

Suspension Modeling Assumptions:

These are assumptions made specifically when modeling the system utilizing the bond graph technique.

- Mass is assumed to be same as last years car
  - 2018/2019 car has not been weighed yet
- Rebound and compression slopes for damper are same
  - Damper slopes can be averaged to achieve a non-dynamic R value
- Tire spring force is constant
  - Tire camber changes constantly throughout operation. On a straight path, our tires will remain mostly at 1.5
    - positive camber allowing us to assume a single tire spring force
- Chassis is rigid body
  - Suspension points are mounted on nodes of the chassis that reduces chassis flex to negligible amount
- No damping effects by tire
  - Tires will be kept at a constant 12 psi for racing conditions
- No damping from spherical bearings
  - Damping effect is insignificant compared to overall system

Suspension Design Assumptions:

These are assumptions made during the initial design of the suspension system.

- Front ride frequency is 3Hz
  - Assumed from past experience and OptimumG references
- Rear ride frequency is 2.8Hz
  - Assumed from past experience and OptimumG references
- Front damping ratio is .65
  - Assumed from past experience and OptimumG references
- Rear damping ratio is .6
  - Assumed from past experience and OptimumG references

State Equation Matrix

Determining Constants

Determining I:

Sprung mass, unsprung mass, and mass moment of inertia were calculated based on a SolidWorks Model of previous years car. An additional estimated factor for average driver weight was added to each value. Values obtained and used in our model are found below.

$M_{Unsprung1} \rightarrow$ Last year's car : 30 lbs $\rightarrow$ 13.6078 kg
$M_{Unsprung2} \rightarrow$ Last year's car : 30 lbs $\rightarrow$ 13.6078 kg
$M_{Sprung} \rightarrow$ Last year's car : 565 lbs $\rightarrow$ 256.28 kg
$J \rightarrow$ SolidWorks File : 850 KgM^2

Determining K:

$MR = 1$
$F_s = 3$ Hz in front, 2.8 in back
$M_{sm} = 246.85$lbf/386.4 front, 258.15lbf/386.4 back (have to convert from lbf to lbm)
K_{ss} becomes lbf/in [2]

Solutions:
Front: 227 lb/in $\rightarrow$ 250 lb/in $\rightarrow$ 43.78 kN/m
Rear: 207 lb/in $\rightarrow$ 200 lb/in $\rightarrow$ 35.025 kN/m

Determining R:

M_{sm} = 55.985kg front, 58.55kg back
ζ_{ride} = .65 in front, .6 in back
ω_{ride}= 3Hz in front, 2.8Hz in back

Solutions:
Front: 1371.88 N/(m/s)
Back: 1236.07 N/(m/s)

Determining lateral and longitudinal load transfer values:

Lateral/longitudinal Acceleration = 1.5 g's
Weight = 505lbs (weight estimate)
Cg height = 14" (last year was ~11, made higher just incase cg rises due to different drivers)
Track width = 61" (Model)
Wheelbase = 47.44"(Model)

Appendix E: Steering Shaft Calculations

Constants	Value	Units	Shown As	
Shear Modulus	11,600,000	psi	G	
Yeild Strength	63100	psi	Yeild	
OD	3/4	in	D	
Max Moment	1560	in*lbs	T	
Shaft Length	12	in	L	
Radius	3/8	in	r	
Inputs	**Value**	**Units**		
Wall Thickness	0.083	in	t	
Calculated Values			**Shown As**	**Equation**
ID	0.58400	in	d	OD-2*t
Polar Moment of Inertia	0.01964	in^4	J	Pi*(D^4-d^4)/32
Output				
Shear Stress	29780.84	psi	τ	T*r/J
Torsional Deflection	4.707080	Degrees	α	LT/JG*(360/2Pi)
Factor of Safety	2.11881178	N/A		Yeild/τ
Recources				

http://asm.matweb.com/search/SpecificMaterial.asp?bassnum=m4130r
http://www.fsaeonline.com/content/Cockpit%20Control%20Forces%20SI%20SAE.pdf

Constants	Value	Units	Shown As	
Elastic Modulus	29,700,000	psi	E	
Yeild Strength	63,100	psi	Yeild	
OD	0.750	in	D	
Max Load	400.000	lbs	F	
Shaft Length	4.000	in	L	
Radius	0.375	in	r/c	
Inputs	**Value**	**Units**		
Wall Thickness	0.083	in	t	
Calculated Values	**Values**	**Units**	**Shown As**	**Equation**
Inner Radius	0.292	in	i	d/2
ID	0.584	in	d	D-2*t
Area Moment of Inertia	0.010	in^4	I	π (OD^4-ID^4) / 64
Max Bending Moment	1,600.000	in*lbs	M	F*L
Max of the 1st Moment	0.019		Q	2/3*(r^3-i^3)
Output	**Values**	**Units**	**Shown As**	**Equation**
Maximum Shear Stress	4,553.011	psi	τ	FQ/
Maximum Bending Stress	61,088.908	psi	σ	M*c/I
Maximim Deflection	0.029	in	δ	FL^3/(3EI)
Factor of Safety	1.033	N/A		Yeild/τ
Recources				

http://asm.matweb.com/search/SpecificMaterial.asp?bassnum=m4130r
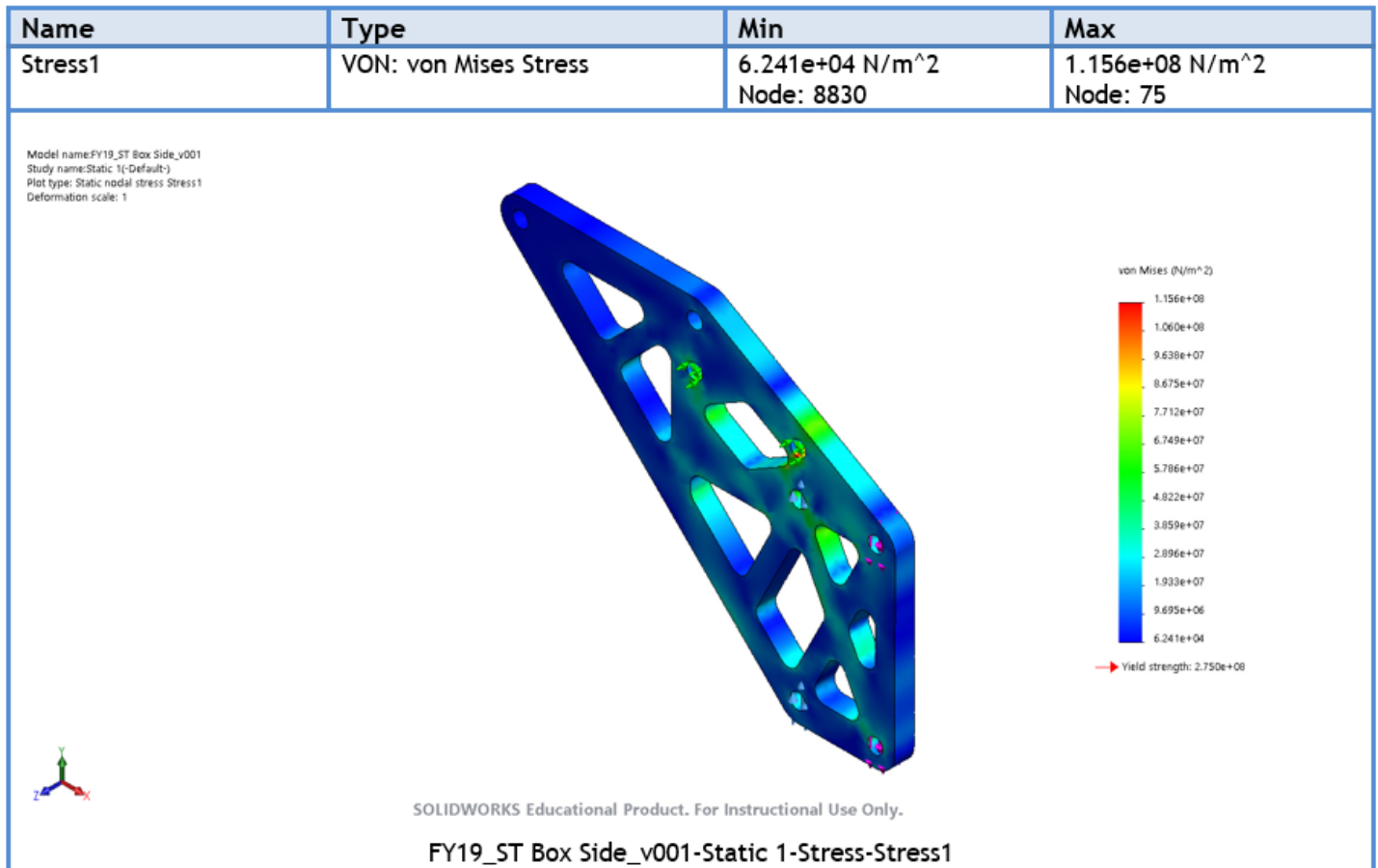http://www.fsaeonline.com/content/Cockpit%20Control%20Forces%20SI%20SAE.pdf

Appendix F: Steering FEA Results

Assumptions

-All loads transferred through bolts.

-Rear bearing box applying a 800lbf force to the sideplates, distributed evenly across 4 holes.

-Front bearing box applying a 1200lbf force to the sideplates, distributed evenly across 4 holes.

-Fixed Reaction at frame mounting holes

Name	Type	Min	Max
Stress1	VON: von Mises Stress	6.241e+04 N/m^2 Node: 8830	1.156e+08 N/m^2 Node: 75

FY19_ST Box Side_v001-Static 1-Stress-Stress1

Stress plot for steering gearbox side plate for load case of driver climbing from vehicle using steering shaft.

Assumptions:

-Each ¼"-20 bolt generates theoretical maximum 1300 lbf, which is applied by the thrust bearing to the box.

-An equal reaction force is applied by the taper bearing race.

-Fixed Reaction at frame mounting holes

Name	Type	Min	Max
Stress1	VON: von Mises Stress	2.330e+05 N/m^2 Node: 988	2.772e+08 N/m^2 Node: 2513
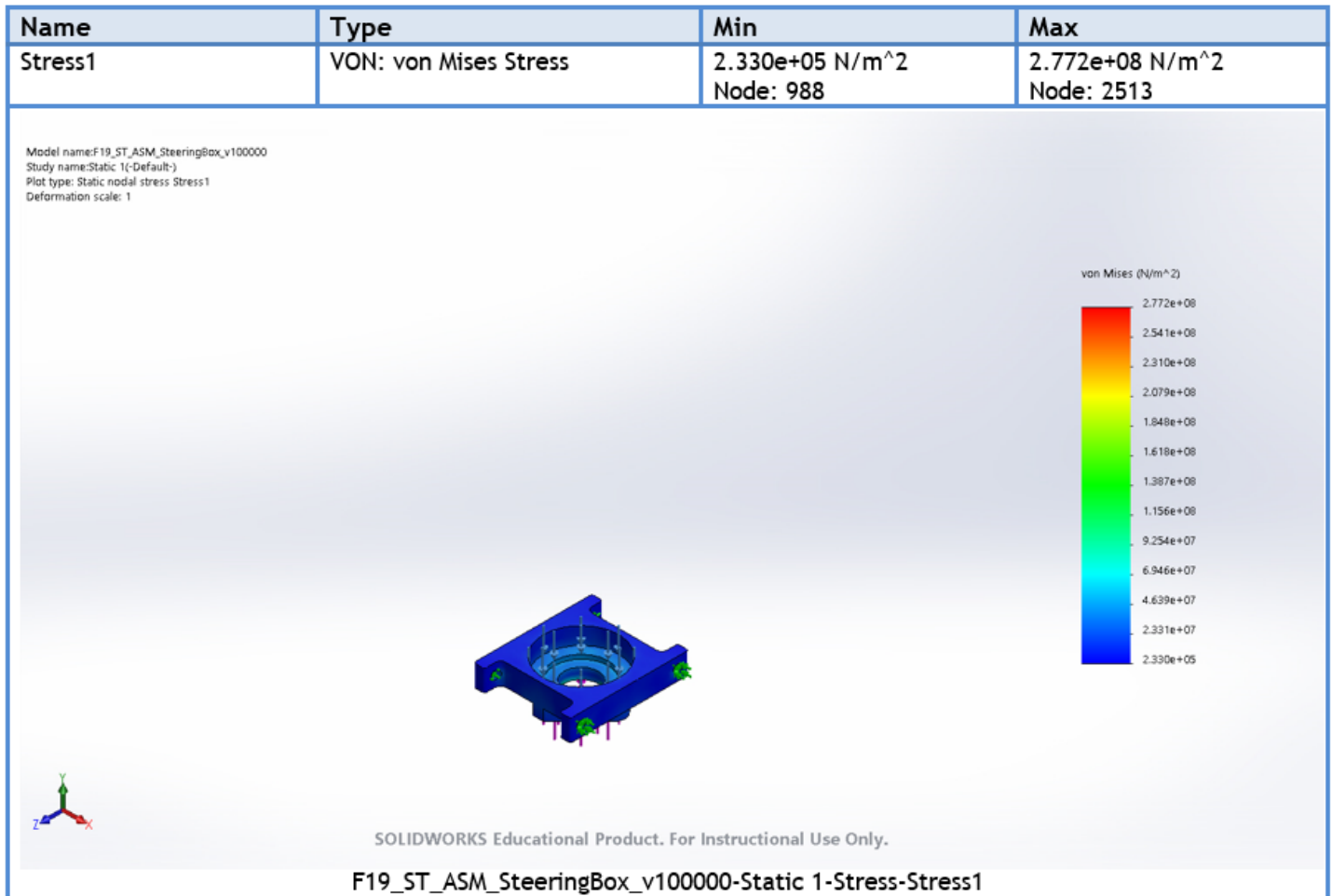
Stress plot for steering gearbox top bearing mount under maximum theoretical clamping load.

Appendix G: Weight Transfer and Brake Bias

Load transfer under 1 g of deceleration

$W_T := 580 \text{lbf}$ $\qquad\qquad$ $L_{WB} := 60.5 \text{in}$

$H_{CG} := 14 \text{in}$

$a_B := 1$

$W_R := \dfrac{W_T \cdot H_{CG} \cdot a_B}{L_{WB}} = 134.215 \text{lbf}$

$W_F := W_T - W_R = 445.785 \text{lbf}$

$Bias_F := \dfrac{W_F}{W_T} = 76.86\%$ $\qquad\qquad$ $Bias_R := \dfrac{W_R}{W_T} = 23.14\%$

$Bias_F + Bias_R = 100\%$

Finding Brake Bias

$R_{Rotor} := 110mm$ $m_{car} := 565lbm$ $F_{Pedal} := 600N$ **Brake Bias Bar**

$$B_F := .5$$

$A_{PadF} := 1in^2$ $A_{PadR} := 1in^2$ $P_U := 7.5in$ $P_L := 1.375in$

$$B_R := 1 - B_F$$

$D_{MCF} := .625in$ $D_{MCR} := .8125in$ $\mu := 0.45$

$A_{CF} := 2.4in^2$ $A_{CR} := .79in^2$ $F_{Cylinders} := \dfrac{F_{Pedal} \cdot P_U}{P_L} = 3.273 \times 10^3 \, N$

$A_{MCF} := \dfrac{1}{4} \cdot \pi \cdot D_{MCF}^2$

$A_{MCR} := \dfrac{1}{4} \cdot \pi \cdot D_{MCR}^2$ $F_{CylF} := F_{Cylinders} \cdot B_F$ $F_{CylR} := F_{Cylinders} \cdot B_R$

$P_{CF} := \dfrac{F_{CylF}}{A_{MCF}} = 1.199 \times 10^3 \cdot psi$ $P_{CR} := \dfrac{F_{CylR}}{A_{MCR}} = 709.507 \cdot psi$

$F_{CalF} := A_{CF} \cdot P_{CF} = 1.28 \times 10^4 \, N$ $F_{CalR} := A_{CR} \cdot P_{CR} = 2.493 \times 10^3 \, N$

$P_{PF} := \dfrac{F_{CalF}}{A_{PadF}} = 1.984 \times 10^7 \, Pa$ $P_{PR} := \dfrac{F_{CalR}}{A_{PadR}} = 3.865 \times 10^6 \, Pa$

$F_{RotorF} := F_{CalF} \cdot \mu = 5.76 \times 10^3 \, N$ $F_{RotorR} := F_{CalR} \cdot \mu = 1.122 \times 10^3 \, N$

Overall Rotor Torques

$\tau_{Front} := F_{RotorF} \cdot 2 \cdot R_{Rotor} = 1.267 \times 10^3 \cdot N \cdot m$ $\tau_{Rear} := F_{RotorR} \cdot 2 \cdot R_{Rotor} = 246.834 \cdot N \cdot m$

$Bias := \dfrac{\tau_{Front}}{\tau_{Front} + \tau_{Rear}} = 0.837$

$1 - Bias = 0.163$

Mathematically adjust bias bar to match load transfer of car

$R_{Rotor} := 110mm$ $m_{car} := 565lbm$ $F_{Pedal} := 600N$

$B_F := .4$

$A_{PadF} := 1in^2$ $A_{PadR} := 1in^2$ $P_U := 7.5in$ $P_L := 1.375in$

$B_R := 1 - B_F$

$D_{MCF} := .625in$ $D_{MCR} := .8125in$ $\mu := 0.45$

$A_{CF} := 2.4in^2$ $A_{CR} := .79in^2$ $F_{Cylinders} := \dfrac{F_{Pedal} \cdot P_U}{P_L} = 3.273 \times 10^3 N$

$A_{MCF} := \dfrac{1}{4} \cdot \pi \cdot D_{MCF}^2$

$A_{MCR} := \dfrac{1}{4} \cdot \pi \cdot D_{MCR}^2$ $F_{CylF} := F_{Cylinders} \cdot B_F$ $F_{CylR} := F_{Cylinders} \cdot B_R$

$P_{CF} := \dfrac{F_{CylF}}{A_{MCF}} = 959.254 \cdot psi$ $P_{CR} := \dfrac{F_{CylR}}{A_{MCR}} = 851.409 \cdot psi$

$F_{CalF} := A_{CF} \cdot P_{CF} = 1.024 \times 10^4 N$ $F_{CalR} := A_{CR} \cdot P_{CR} = 2.992 \times 10^3 N$

$P_{PF} := \dfrac{F_{CalF}}{A_{PadF}} = 1.587 \times 10^7 Pa$ $P_{PR} := \dfrac{F_{CalR}}{A_{PadR}} = 4.638 \times 10^6 Pa$

$F_{RotorF} := F_{CalF} \cdot \mu = 4.608 \times 10^3 N$ $F_{RotorR} := F_{CalR} \cdot \mu = 1.346 \times 10^3 N$

Overall Rotor Torques

$\tau_{Front} := F_{RotorF} \cdot 2 \cdot R_{Rotor} = 1.014 \times 10^3 \cdot N \cdot m$ $\tau_{Rear} := F_{RotorR} \cdot 2 \cdot R_{Rotor} = 296.201 \cdot N \cdot m$

$Bias := \dfrac{\tau_{Front}}{\tau_{Front} + \tau_{Rear}} = 0.774$

$1 - Bias = 0.226$

Finding deceleration of car

$$F_{TireF} := \frac{\tau_{Front}}{20.5in} = 1.947 \times 10^3 \, N \quad F_{TireR} := \frac{\tau_{Rear}}{20.5in} = 568.852 \, N$$

$$a_C := \frac{F_{TireF} + F_{TireR}}{m_{car}} = 1.001 \cdot g$$

Appendix H: FEA of Brake Pedal

Name	Force	Min	Maxb
Brake Pedal Factor of Safety	2000N	3.353e+00 Node: 937	4.719e+03 Node: 1439

Model name:F19_CO_BrakePedal_V4
Study name:Full Brake Force(-Default<As Machined>-)
Plot type: Factor of Safety Factor of Safety1
Criterion : Automatic
Factor of safety distribution: Min FOS = 3.4

FOS
4.719e+03
4.326e+03
3.933e+03
3.540e+03
3.147e+03
2.754e+03
2.361e+03
1.968e+03
1.575e+03
1.182e+03
7.893e+02
3.963e+02
3.353e+00

SOLIDWORKS Educational Product. For Instructional Use Only.

F19_CO_BrakePedal_V4-Full Brake Force-Factor of Safety-Factor of Safety1